

ISSN 1573-160X

Vol. 31, Iss. 3

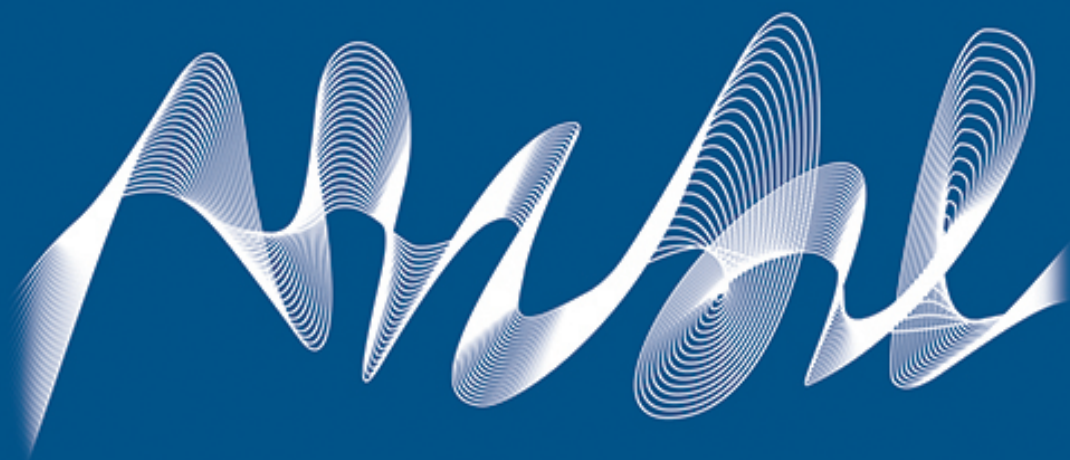
May – June

2024



Physical Oceanography

<http://physical-oceanography.ru/>



ISSN 1573-160X

Vol. 31, no. 3. 2024

May – June

Founded in January 1987

Publication frequency:

6 issues per year

Physical Oceanography

Scientific and theoretical journal

FOUNDER AND PUBLISHER:

Federal State Budget Scientific Institution

Federal Research Centre

“Marine Hydrophysical Institute of RAS”

Peer reviewed scientific journal.

The Journal publishes original research results, review articles (at the editorial board's request) and brief reports on the following sections of hydrophysics:

- thermohydrodynamics of the ocean and atmosphere;
- analysis of observational results and methods of calculation of ocean hydrophysical fields;
- experimental and expeditionary studies;
- satellite hydrophysics;
- mathematical modelling of marine systems;
- automation of scientific research of the seas and oceans.

Objectives

- familiarisation of the world and Russian scientific community with the results of theoretical, experimental and expeditionary studies of the World Ocean;
- exchange of scientific information, experience, research and observation data with specialists from different regions of the country and abroad;
- increase of publication activity of national authors, rating of scientific organisations of Russia and level of national publications in the world scientific community according to their citation data;
- theoretical and practical assistance to scientists in preparing articles for printing that meet modern requirements of publication and scientific ethics;
- strengthening the popularity and authority of the publication, increasing the number of regular subscribers

The Journal is indexed in:

Google Scholar
Web of Science (ESCI)
Scopus
EBSCO Publishing

journal@mhi-ras.ru

<http://physical-oceanography.ru/>

Founder, Publisher and Editorial Office address:

2, Kapitanskaya St., Sevastopol, 299011

Russia

Phone, fax: + 7 (8692) 54-02-23

EDITORIAL BOARD

- Sergey K. Konovalov** – Editor-in-Chief, Director of FSBSI FRC MHI, corresponding member of RAS, Dr.Sci. (Geogr.), ORCID ID: 0000-0002-5200-8448, secretary@mhi-ras.ru (Sevastopol, Russia)
- Vladimir N. Belokopytov** – Deputy Editor-in-Chief, Head of Department of FSBSI FRC MHI, Dr.Sci. (Geogr.), ORCID ID: 0000-0003-4699-9588, (Sevastopol, Russia)
- Aleksandr I. Kubryakov** – Deputy Editor-in-Chief, Chief Scientist Researcher of FSBSI FRC MHI, Dr.Sci. (Phys.-Math.), ORCID ID: 0000-0003-1899-9230, ResearcherID: F-8959-2014, (Sevastopol, Russia)
- Igor K. Ivashchenko** – Executive Editor, Senior Scientist of FSBSI FRC MHI, Ph.D. (Econ.), (Sevastopol, Russia)
- Yuri V. Artamonov** – Head Scientist Researcher of FSBSI FRC MHI, Dr.Sci. (Geogr.), ResearcherID: AAC-6651-2020 (Sevastopol, Russia)
- Sergey V. Berdnikov** – Director of FRC SSC of RAS, Dr.Sci. (Geogr.), ORCID ID: 0000-0002-3095-5532 (Rostov-on-Don, Russia)
- Valery G. Bondur** – Scientific Supervisor of ISR "AEROCOSMOS", academician of RAS, Dr.Sci. (Techn.), ORCID ID: 0000-0002-2049-6176 (Moscow, Russia)
- Demuri I. Demetralashvili** – Head of the sector of mathematical modeling of geophysical processes of sea and atmosphere, the Nodia Institute of Geophysics of the Javakishvili Tbilisi State University, Dr.Sci. (Phys.-Math.), ORCID ID: 0000-0002-4789-4852 (Tbilisi, Georgia)
- Sergey A. Dobrolyubov** – Dean of Faculty of Geography of MSU, academician of RAS, Dr.Sci. (Geogr.), prof., ResearcherID: A-9688-2012 (Moscow, Russia)
- Grigory I. Dolgikh** – Director of POI FEB of RAS, Dr.Sci. (Phys.-Math.), academician of RAS, prof., ORCID ID: 0000-0002-2806-3834 (Vladivostok, Russia)
- Vladimir A. Dulov** – Head of Laboratory of FSBSI FRC MHI, Dr.Sci. (Phys.-Math.), prof., ORCID ID: 0000-0002-0038-7255, (Sevastopol, Russia)
- Vladimir V. Efimov** – Head of Department of FSBSI FRC MHI, Dr.Sci. (Phys.-Math.), prof., ResearcherID: P-2063-2017, (Sevastopol, Russia)
- Vladimir V. Fomin** – Head of Department of FSBSI FRC MHI, Dr.Sci. (Phys.-Math.), ORCID ID: 0000-0002-9070-4460, (Sevastopol, Russia)
- Isaac Gertman** – Head of the Physical Oceanography Department of Israel Oceanographic & Limnological Research, Head of IOLR data center ISRAMAR, Ph.D. (Geogr.), ORCID ID: 0000-0002-6953-6722 (Haifa, Israel)
- Dmitry G. Gryazin** – Head of Department, Chief Metrologist of SRC of the "Concern CSRI Elektropribor" JSC, Dr.Sci. (Techn.), prof. of Mechatronics of ITMO University, Scopus AuthorID: 25638150600, (Saint Petersburg, Russia)
- Rashit A. Ibraev** – Chief Scientist Researcher of INM of RAS, corresponding member of RAS, Dr.Sci. (Phys.-Math.), ORCID ID: 0000-0002-9099-4541 (Moscow, Russia)
- Vasily V. Knysh** – Head Scientist Researcher of FSBSI FRC MHI, Dr.Sci. (Phys.-Math.), prof., ResearcherID: B-3603-2018 (Sevastopol, Russia)
- Gennady K. Korotaev** – Scientific Supervisor of FSBSI FRC MHI, corresponding member of RAS, Dr.Sci. (Phys.-Math.), prof., ResearcherID: K-3408-2017 (Sevastopol, Russia)
- Vladimir N. Kudryavtsev** – Executive Director of Satellite Oceanography Laboratory of RSHU, Dr.Sci. (Phys.-Math.), prof., ResearcherID: G-1502-2014 (Saint Petersburg)
- Michael E. G. Lee** – Head of Department of FSBSI FRC MHI, Dr.Sci. (Phys.-Math.), prof., ORCID ID: 0000-0002-2292-1877 (Sevastopol, Russia)
- Gennady G. Matishov** – Deputy President of RAS, Deputy academician-Secretary of the Department of Earth Sciences of Supervisor of RAS – Head of the Oceanology, Atmospheric Physics and Geography Section, Scientific Supervisor of SSC of RAS, Supervisor of MMBI KSC of RAS, academician of RAS, Dr.Sci. (Geogr.), prof., ORCID ID: 0000-0003-4430-5220 (Rostov-on-Don, Russia)
- Nikolay A. Rimski-Korsakov** – Deputy Director (Marine Engineering) of FSBSI P.P. Shirshov IO of RAS, Dr.Sci. (Techn.), ResearcherID: K-8378-2017 (Moscow, Russia)
- Angelo Rubino** – Professor of Ca' Foscari University, Ph.D. (Phys. Oceanogr.), ORCID ID: 0000-0003-3857-4811 (Venice, Italy)
- Anatoly S. Samodurov** – Head of Department of FSBSI FRC MHI, Dr.Sci. (Phys.-Math.), ResearcherID: V-8642-2017 (Sevastopol, Russia)
- Georgy I. Shapiro** – Head of Plymouth Ocean Forecasting Centre of the University of Plymouth, Dr.Sci. (Phys.-Math.), prof. in Phys. Oceanogr., (Plymouth, Great Britain)
- Naum B. Shapiro** – Head Scientist Researcher of FSBSI FRC MHI, Dr.Sci. (Phys.-Math.), ResearcherID: A-8585-2017 (Sevastopol, Russia)
- Mikhail V. Shokurov** – Head Scientist Researcher of FSBSI FRC MHI, Dr.Sci. (Phys.-Math.), ORCID ID: 0000-0003-1595-8281 (Sevastopol, Russia)
- Elena F. Vasechkina** – Deputy Director of FSBSI FRC MHI, Chief Research Associate of FSBSI FRC MHI, Dr.Sci. (Geogr.), ORCID ID: 0000-0001-7007-9496 (Sevastopol, Russia)
- Elizaveta V. Zabolotskikh** – Head Scientist Researcher of RSHU, Dr.Sci. (Phys.-Math.), Scopus Author ID: 6506482460 (Saint Petersburg, Russian)
- Vladimir B. Zalesny** – Head Scientific Researcher of INM of RAS, Dr.Sci. (Phys.-Math.), prof., ORCID ID: 0000-0003-3829-3374 (Moscow, Russia)
- Andrey G. Zatsepin** – Chief of Laboratory of FSBSI P.P. Shirshov IO of RAS, Chief Research Associate of FSBSI P.P. Shirshov IO of RAS, Dr.Sci. (Phys.-Math.), ORCID ID: 0000-0002-5527-5234 (Moscow, Russia)
- George Zodiatis** – Senior Researcher of Laboratory of Coastal and Marine Research of the Institute of Applied and Computational Mathematics, for Research and Technology Foundation – Hellas, Ph.D. (Oceanol.), ResearcherID: J-3032-2013 (Heraklion, Crete, Greece)

CONTENTS

Vol. 40, no. 3. 2024

May – June, 2024

THERMOHYDRODYNAMICS OF THE OCEAN AND THE ATMOSPHERE

- Demyshev S. G.** Finite-difference approximation of the potential vorticity equation for a stratified incompressible fluid and an example of its application for modeling the Black Sea circulation. Part II. Discrete equation of potential vorticity in a quasi-static approximation and an example of its application for simulation the Black Sea circulation in 2011..... 319

ANALYSIS OF OBSERVATIONS AND METHODS OF CALCULATING HYDROPHYSICAL FIELDS IN THE OCEAN

- Andrulionis N. Yu., Podymov O. I.** Errors in calculating density using the CTD probe data in suboxic layer of the Black Sea 336
- Rostov I. D., Dmitrieva E. V.** Trends in the interannual variability of salinity field in the upper 1000-meter layer of the northeastern Pacific Ocean under conditions of modern global warming 350
- Smirnov A. V., Ivanov V. V., Sokolov A. A.** Comparison analysis of heat and mass transport through Fram Strait calculated using the mooring and ocean reanalysis data 364
- Shevchenko G. V., Lozhkin D. M.** Spatial and temporal variability of a latent heat flux in the northwest Pacific Ocean based on the ERA5 reanalysis data 387

EXPERIMENTAL AND FIELD RESEARCH

- Myslina M. A., Varenik A. V., Tarasevich D. V.** Dynamics of nutrients concentration in the Chernaya River waters (Crimean Peninsula) in 2015–2020 398
- Kovalev D. P., Manilyuk Yu. V., Kovalev P. D.** Sea level oscillations in the adjacent bays – Trade Port and Kholmsk-Severny (Sakhalin Island)..... 409

MATHEMATICAL MODELING OF MARINE SYSTEMS

- Fomin V. V., Ivancha E. V., Polozok A. A.** Resuspension of bottom sediments in a shallow lagoon by currents and waves based on the numerical modeling data (using the example of Sivash Bay, the Sea of Azov) 427



All the materials of the journal are available under Creative
Commons Attribution-NonCommercial 4.0 International (CC BY-NC 4.0)

Finite-Difference Approximation of the Potential Vorticity Equation for a Stratified Incompressible Fluid and an Example of its Application for Modeling the Black Sea Circulation*

Part II. Discrete Equation of Potential Vorticity in a Quasi-Static Approximation and an Example of its Application for Simulation the Black Sea Circulation in 2011

S. G. Demyshev

Marine Hydrophysical Institute of RAS, Sevastopol, Russian Federation

✉ demyshev@gmail.com

Abstract

Purpose. The study is purposed at deriving a finite-difference equation of potential vorticity for a three-dimensional baroclinic fluid with regard for diffusion and viscosity in a quasi-static approximation. Its terms are calculated and analyzed in numerical modeling of the Black Sea circulation for two periods – winter and summer 2011.

Methods and Results. A finite-difference equation for the potential vorticity of a stratified incompressible fluid is obtained for a system of discrete equations of sea dynamics in the hydrostatic approximation allowing for viscosity, diffusion, river inflow, water exchange through the straits and atmospheric forcing. It is shown that the main contribution to the potential vorticity is made by its vertical component. The horizontal components are predominant in the areas of river inflow and water exchange through the straits. The vertical component of potential vorticity, except for the river inflow zones, is conditioned by the value and structure of an absolute eddy. The main contribution in the sea upper layer of the coastal region, its northwestern part and along the Anatolian coast is made by the advection of potential vorticity. At the lower horizons, its highest values are observed in the coastal strip, at that its character is more pronounced near the southern coast of the sea.

Conclusions. Analysis of the potential vorticity equation has shown that the value of the advective terms is conditioned by the divergence of the product of nonlinear terms in the motion equations and density gradient. The main conclusion consists in the following: locally, the sum of vertical and horizontal advection of potential vorticity is two orders of magnitude less than each of them separately.

Keywords: numerical modeling, kinetic energy, discrete equations, Black Sea, cyclonic circulation, anticyclonic eddies, eddy, potential vorticity, Ertel invariant

Acknowledgments: The study was carried out with financial support of the Russian Science Foundation grant 23-27-00141.

For citation: Demyshev, S.G., 2024. Finite-Difference Approximation of the Potential Vorticity Equation for a Stratified Incompressible Fluid and an Example of its Application for Modeling the Black Sea Circulation. Part II. Discrete Equation of Potential Vorticity in a Quasi-Static Approximation and an Example of its Application for Simulation the Black Sea Circulation in 2011. *Physical Oceanography*, 31(3), pp. 319-335.

© 2024, S. G. Demyshev

© 2024, Physical Oceanography

* See Part I: Demyshev, S.G., 2024. Finite-Difference Approximation of the Potential Vorticity Equation for a Stratified Incompressible Fluid and an Example of its Application for Modeling the Black Sea Circulation. Part I. Finite-Difference Equation of Potential Vorticity of Ideal Fluid. *Physical Oceanography*, 31(2), pp. 149-160.



Introduction

To study circulation in the atmosphere and ocean, analysis of potential vorticity (PV) is of fundamental importance, since PV characterizes the role of nonlinear processes in fluid dynamics. In the field of potential mass force in the absence of viscosity and density diffusion (ideal fluid), PV is an invariant [1] and therefore its structure determines the trajectory of fluid particles preserving potential vorticity. The difficulty is that in reality the abovementioned conditions are not met or only met in an approximate form, since friction, diffusion and diabaticity change the PV of seawater particles. When analyzing the equation of potential vorticity of a stratified fluid, it is possible to estimate the influence of nonlinear and diffusion factors on its evolution.

The importance of Ertel's theorem for research in the field of physical oceanography is discussed in [2]. It emphasizes that for large-scale water movements, the appropriate form of vorticity is potential vorticity, which includes such physically different elements as velocity vortex and seawater density. Ertel's theorem, which most other vorticity theorems are derived from, determines dynamic evolution of potential vorticity. In turn, the absence of potential vorticity means an inertial-gravitational mode of motion that depends on the ocean stratification. Since Ertel's theorem does not depend on the specific type of Lagrangian invariant, modified formulas for potential vorticity can be applied. As an example, the work [3] introducing "optimal" potential vorticity can be pointed out. As a result, the approach used permits to quantify the degree of disequilibrium in atmospheric climate processes.

Studies of the dynamics of currents in the atmosphere and ocean based on the potential vorticity analysis are few. Apparently, this is due to two factors. Firstly, potential vorticity according to Ertel is a kinematic quantity [4], from which it is impossible to determine intensity of the vortex structure of currents and even the rotation sign. Secondly, it is often sufficient to consider the potential vorticity in the quasi-geostrophic approximation according to Rossby [5] that is a dynamic characteristic [4] and contains the necessary information about the dynamics of currents.

For the analysis of atmospheric forecasts, the work [6] plays an important role. It analyses the possibilities of using isentropic maps of potential vorticity to represent some dynamic processes in the atmosphere. Examples from operational weather analysis and from idealized theoretical models are given to illustrate this approach and its relationship to classical synoptic concepts. The structure, reasons for the formation and stability of cyclones and blocking anticyclones, physical mechanisms of Rossby wave propagation, baroclinic and barotropic instability in space and time are discussed.

In [4], the concept of "potential vorticity" is analyzed and the basic relationships for calculations are considered, the approaches of Rossby and Ertel are studied. As an example, estimates are given from observational data of potential vorticity for the quasi-permanent anticyclonic Lofoten eddy in the Norwegian Sea. The authors showed that Ertel potential vorticity is a kinematic characteristic and Rossby potential vorticity in the quasi-geostrophic approximation is dynamic.

Analysis of the Ertel potential vorticity equation permits to estimate the contribution of nonlinear and diffusion effects to the balance of forces that

determine PV evolution. This study is a continuation of the research [7]. It is aimed at obtaining a discrete equation for the potential vorticity of a stratified fluid in a quasi-static approximation as a consequence of the initial finite-difference system of equations of the Black Sea dynamics model using the example of the Black Sea circulation with realistic atmospheric conditions for 2011 and to analyze the resulting potential vorticity equation.

Equation of potential vorticity of a stratified incompressible fluid in the quasi-static approximation

In the Boussinesq approximation and quasi-statics in the Cartesian coordinate system, the fluid motion in the domain Ω with boundary $\partial\Omega$ in the Gromeka-Lamb form is described by the following system of equations:

$$\frac{\partial \vec{U}_H}{\partial t} + \vec{\xi} x \vec{U}_H = -\frac{1}{\rho_0} \nabla(P + E) + \vec{F}, \quad (1)$$

$$\frac{\partial P}{\partial z} = g\rho, \quad (2)$$

$$\nabla \vec{U} = 0, \quad (3)$$

$$\frac{\partial T}{\partial t} + \text{div}(T\vec{U}) = (\kappa^T T_z)_z - \kappa^H \nabla^4 T, \quad (4)$$

$$\frac{dS}{dt} + \text{div}(S\vec{U}) = (\kappa^S S_z)_z - \kappa^H \nabla^4 S, \quad (5)$$

$$\rho = \Phi(T, S). \quad (6)$$

The following designations are introduced: $\vec{U} = (\vec{U}_H, w) = (u, v, w)$ are the components of the current velocity vector along the axes (x, y, z) directed to the east, north and vertically downwards, respectively; $\vec{F} = (F^u, F^v)$, $\vec{g} = (0, 0, g)$ is free fall acceleration; $(T, S, P$ and $\rho)$ are temperature, salinity, pressure and sea water density; $\rho_0 = 1 \text{ g/cm}^3$ (here and henceforth it is pressure and density normalized to ρ_0); $\vec{f} = (0, 0, f^z)$ is the Coriolis parameter, where $f^z = 2\omega \sin \varphi$; ω is angular velocity of the Earth's rotation; φ is latitude.

In equation (1), taking into account the quasi-static approximation, the absolute velocity vortex and kinetic energy of motion are introduced:

$$\vec{\xi} = (\xi^x, \xi^y, \xi^z), \text{ где } \xi^x = -\frac{\partial v}{\partial z}, \xi^y = \frac{\partial u}{\partial z}, \xi^z = \frac{\partial v}{\partial x} - \frac{\partial u}{\partial y} + f^z = \xi^r + f^z,$$

$$F^u = (\mu^{\text{ver}} u_z)_z - \mu^{\text{hor}} \nabla^4 u, \quad F^v = (\mu^{\text{ver}} v_z)_z - \mu^{\text{hor}} \nabla^4 v, \quad \vec{F} = (F^u, F^v),$$

$$E = \rho_0 \frac{u^2 + v^2}{2},$$

where μ^{ver} , μ^{hor} are coefficients of vertical and horizontal exchange of momentum.

On the surface at $z = 0$

$$v_v u_z = -\tau^x, v_v v_z = -\tau^y, w = -\zeta_t, \kappa^T T_z = Q^T, \kappa^S S_z = \frac{Ev - Pr}{\rho_1} S_0; \quad (7)$$

at the bottom at $z = H(x, y)$

$$u = v = w = 0, T_z = S_z = 0. \quad (8)$$

The following designations are used: (τ^x, τ^y) is tangential wind stress; Q^T is heat flow; Ev is sea water evaporation; Pr is precipitation; S_0 is model salinity on the sea surface; ρ_1 is sea water density on the sea surface.

Functions $\mu^{ver}, \kappa^T, \kappa^S$ were calculated in accordance with the Mellor–Yamada parameterization [6].

On solid side walls for meridional boundary sections:

$$u = \nabla^2 u = v_x = \nabla^2 v_x = 0, T_x = (\nabla^2 T)_x = S_x = (\nabla^2 S)_x = 0, \quad (9)$$

for zonal boundary sections:

$$v = \nabla^2 v = u_y = \nabla^2 u_y = 0, T_y = (\nabla^2 T)_y = S_y = (\nabla^2 S)_y = 0. \quad (10)$$

In boundary areas where water flows in, the following conditions are used: for meridional sections

$$u = u^p, \nabla^2 u = v_x = \nabla^2 v_x = 0, T = T^p, S = S^p, (\nabla^2 T)_x = (\nabla^2 S)_x = 0, \quad (11)$$

for zonal sections

$$v = v^p, \nabla^2 v = u_y = \nabla^2 u_y = 0, T = T^p, S = S^p, (\nabla^2 T)_y = (\nabla^2 S)_y = 0. \quad (12)$$

For the Upper Bosphorus Current and for the Kerch Strait, when the current is directed from the Black Sea to the Sea of Azov

$$v = v^s, \nabla^2 v = u_y = \nabla^2 u_y = 0, T_y = 0, S_y = 0, (\nabla^2 T)_y = (\nabla^2 S)_y = 0. \quad (13)$$

When $t = t^0$, the following initial conditions are set:

$$u = u^0(x, y, z), v = v^0(x, y, z), \zeta = \zeta^0(x, y), T = T^0(x, y, z), S = S^0(x, y, z). \quad (14)$$

Based on the system of equations (1)–(6), the Ertel equation is derived. Applying the corresponding operation from relations (1)–(2) and taking into account the continuity equation (3), the equation for $\vec{\xi}$ is obtained

$$\frac{\partial \vec{\xi}}{\partial t} + \vec{U}(\nabla \vec{\xi}) - \vec{\xi} \nabla \vec{U} = \nabla \times (\vec{g} \rho + \vec{F}^\xi), \quad (15)$$

where $\vec{F}^\xi = (F^u, F^v, 0)$.

A consequence of equations (4), (5) is the equation for density

$$\frac{\partial \rho}{\partial t} + \text{div}(\vec{U} \rho) = \Phi(D^T, D^S), \quad (16)$$

where the following designations are introduced

$$D^T = (\kappa^T T_z)_z - \kappa^H \nabla^4 T, \quad D^S = (\kappa^S S_z)_z - \kappa^H \nabla^4 S. \quad (17)$$

The potential vorticity of an incompressible fluid in the quasi-static approximation has the following form:

$$\omega = \bar{\xi} \nabla \rho = -\frac{\partial v}{\partial z} \frac{\partial \rho}{\partial x} + \frac{\partial u}{\partial z} \frac{\partial \rho}{\partial y} + \left[\left(\frac{\partial v}{\partial x} - \frac{\partial u}{\partial y} \right) + f^z \right] \frac{\partial \rho}{\partial z}. \quad (18)$$

Then, from equations (15), (16), taking into account expressions (3), (17) and (18), the Ertel equation follows in the quasi-static approximation for a viscous fluid

$$\frac{\partial \omega}{\partial t} + \text{div}(\bar{U} \omega) = \Phi^\omega, \quad (19)$$

where

$$\Phi^\omega = (\bar{\xi} \nabla) \Phi + [(\nabla \times \bar{F}^\xi) \nabla] \rho. \quad (20)$$

Discrete potential vorticity equation in a quasi-static approximation

In accordance with the difference operators introduced in [7], the following differential-difference equations of model (1)–(6) (differential in time) are written out:

$$\frac{du_{i,j+1/2,k}}{dt} - [v, \xi^z]_{i+1/2,j,k} + [w, \xi^y]_{i+1/2,j,k} = -\delta_x (E_{i+1/2,j,k} + P_{i+1/2,j,k}) + F_{i+1/2,j,k}^u, \quad (21)$$

$$\frac{dv_{i,j+1/2,k}}{dt} + [u, \xi^z]_{i,j+1/2,k} - [w, \xi^x]_{i,j+1/2,k} = -\delta_y (E_{i,j+1/2,k} + P_{i,j+1/2,k}) + F_{i,j+1/2,k}^v, \quad (22)$$

$$\delta_z P_{i,j,k+1/2} = g \rho_{i,j,k+1/2}, \quad (23)$$

$$\delta_x u_{i,j,k} + \delta_y v_{i,j,k} + \delta_z w_{i,j,k} = 0, \quad (24)$$

$$\begin{aligned} \frac{dT_{i,j,k}}{dt} + \delta_x (u_{i,j,k} T_{i,j,k}) + \delta_y (v_{i,j,k} T_{i,j,k}) + \delta_z (w_{i,j,k} T_{i,j,k}) = \\ = \delta_z (\kappa_{i,j,k}^T \delta_z T_{i,j,k}) - \kappa^H \nabla_{xy}^2 (\nabla_{xy}^2 T_{i,j,k}), \end{aligned} \quad (25)$$

$$\begin{aligned} \frac{dS_{i,j,k}}{dt} + \delta_x (u_{i,j,k} S_{i,j,k}) + \delta_y (v_{i,j,k} S_{i,j,k}) + \delta_z (w_{i,j,k} S_{i,j,k}) = \\ = \delta_z (\kappa_{i,j,k}^S \delta_z S_{i,j,k}) - \kappa^H \nabla_{xy}^2 (\nabla_{xy}^2 S_{i,j,k}), \end{aligned} \quad (26)$$

$$\rho_{i,j,k} = \rho_0 + \alpha_1^T T_{i,j,k} + \alpha_1^S S_{i,j,k} + \alpha_2^T T_{i,j,k}^2 + \alpha^{ST} S_{i,j,k} T_{i,j,k}. \quad (27)$$

In the quasi-static approximation, the components of the velocity vortex (Fig. 1) have the following form:

$$\xi_{i,j+1/2,k+1/2}^x = -\delta_z v_{i,j+1/2,k+1/2}, \quad \xi_{i+1/2,j,k+1/2}^y = \delta_z u_{i+1/2,j,k+1/2},$$

$$\xi_{i+1/2,j+1/2,k}^z = \delta_x v_{i+1/2,j+1/2,k} - \delta_y u_{i+1/2,j+1/2,k} + f_{j+1/2}^z. \quad (28)$$

Representation (28) follows that at the vertices of the box (i, j, k) (Fig. 1) an important relation is satisfied

$$\delta_x \xi_{i+1/2,j+1/2,k+1/2}^x + \delta_y \xi_{i+1/2,j+1/2,k+1/2}^y + \delta_z \xi_{i+1/2,j+1/2,k+1/2}^z = 0.$$

We believe that the terms in square brackets on the left side of equations (21)–(22) are written in a form that ensures conservation of enstrophy and energy [9] for the shallow water approximation and correspond to formulas (32) in [10].

Equations for the components of the absolute velocity vortex (analogous to the equation (15)) – for ξ^x at the point $i, j+1/2, k+1/2$, for ξ^y at $i+1/2, j, k+1/2$ and for ξ^z at $i+1/2, j+1/2, k$ – taking into account viscosity, follow from relations (21)–(24) and have the following form:

$$\begin{aligned} \frac{d\xi^x}{dt} + \delta_z ([w, \xi^x]) - \delta_z ([u, \xi^z]) &= g \delta_y \bar{\rho}^z - \delta_z F^v, \\ \frac{d\xi^y}{dt} + \delta_z ([w, \xi^y]) - \delta_z ([v, \xi^z]) &= -g \delta_x \bar{\rho}^z + \delta_z F^u, \end{aligned} \quad (29)$$

$$\frac{d\xi^z}{dt} + \delta_x ([u, \xi^z]) + \delta_y ([v, \xi^z]) - \delta_x ([w, \xi^x]) - \delta_y ([w, \xi^y]) = \delta_x F^v - \delta_y F^u.$$

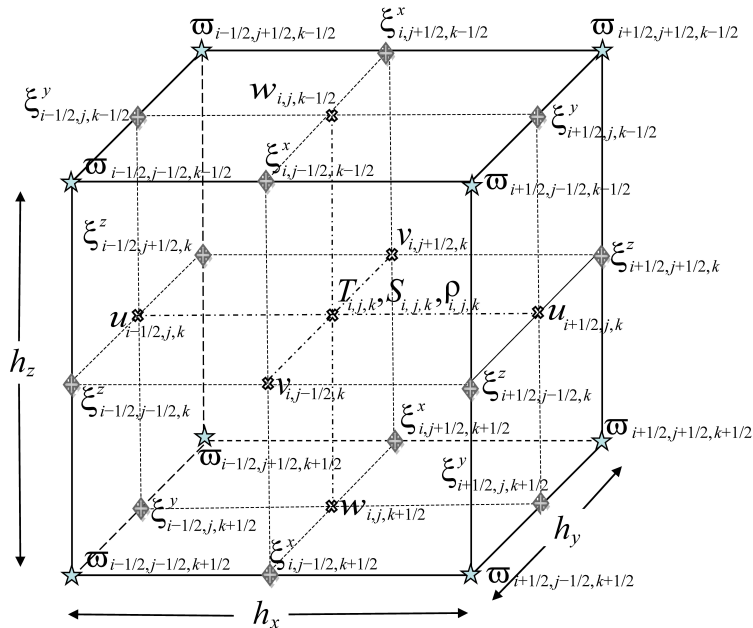


Fig. 1. Distribution of variables in box (i, j, k) . At the box vertices indicated by asterisks, PV (ω) is determined and on its edges – the components of absolute vortex velocity

The following designations are introduced:

$$\Lambda_{i,j+1/2,k+1/2}^x = -\delta_z F_{i,j+1/2,k+1/2}^v,$$

$$\Lambda_{i+1/2,j,k+1/2}^y = \delta_z F_{i+1/2,j,k+1/2}^u,$$

$$\Lambda_{i+1/2,j+1/2,k}^z = \delta_x F_{i,j+1/2,k+1/2}^v - \delta_y F_{i+1/2,j+1/2,k}^u.$$

The density equation at the point (i, j, k) is a consequence of relations (25)–(27) and is written as follows:

$$\frac{d\rho}{dt} + \delta_x(u\rho) + \delta_y(v\rho) + \delta_z(w\rho) = D_V^\rho + \kappa^H D_H^\rho = D^\rho, \quad (30)$$

where

$$D_V^\rho = \alpha_1^T \delta_z [\kappa^V (\delta_z T)] + \alpha_1^S \delta_z [\kappa^V (\delta_z S)] + 2\alpha_2^T [\delta_z [\kappa^V T] (\delta_z T)] + \\ + \alpha^{TS} [T \delta_z [\kappa^V (\delta_z S)] + S \delta_z [\kappa^V (\delta_z T)]],$$

$$D_H^\rho = \alpha_1^T \nabla_{xy}^2 T + \alpha_1^S \nabla_{xy}^2 S + 2\alpha_1^T T \nabla_{xy}^2 T + \alpha^{TS} [T \nabla_{xy}^2 S + S \nabla_{xy}^2 T].$$

Carrying out similar [5] transformations with equations (29), (30), the equation of potential vorticity is obtained at the point $i+1/2, j+1/2, k+1/2$ in the quasi-static approximation

$$\frac{d\omega}{dt} + \delta_x (\Upsilon^x \bar{\rho}^{\overline{yz}} + \xi^x R^x) + \delta_y (\Upsilon^y \bar{\rho}^{\overline{xz}} + \xi^y R^y) + \delta_z (\Upsilon^z \bar{\rho}^{\overline{xy}} + \xi^z R^z) = \overline{\Lambda^x}^x \delta_x (\bar{\rho}^{\overline{yz}}) + \\ + \overline{\Lambda^y}^y \delta_y (\bar{\rho}^{\overline{xz}}) + \overline{\Lambda^z}^z \delta_z (\bar{\rho}^{\overline{xy}}) + \xi^x \delta_x (\overline{D^\rho}^{\overline{yz}}) + \xi^y \delta_y (\overline{D^\rho}^{\overline{xz}}) + \xi^z \delta_z (\overline{D^\rho}^{\overline{xy}}), \quad (31)$$

where the right side of equation (31) is a difference analog of expression (20). Taking into account the quasi-static approximation and equations (29), the following notations are adopted:

$$\Upsilon_{i,j+1/2,k+1/2}^x = \delta_z ([w, \xi^x])_{i,j+1/2,k} - \delta_z ([u, \xi^z])_{i,j+1/2,k},$$

$$\Upsilon_{i+1/2,j,k+1/2}^y = \delta_z ([w, \xi^y])_{i+1/2,j,k+1/2} - \delta_z ([v, \xi^z])_{i+1/2,j,k+1/2},$$

$$\Upsilon_{i+1/2,j+1/2,k}^z = \delta_x ([u, \xi^z])_{i+1/2,j+1/2,k} + \delta_y ([v, \xi^z])_{i+1/2,j+1/2,k} - \\ - \delta_x ([w, \xi^x])_{i+1/2,j+1/2,k} - \delta_y ([w, \xi^y])_{i+1/2,j+1/2,k},$$

$$\overline{\rho}_{i,j+1/2,k+1/2}^{\overline{yz}} = \overline{\rho}_{i+1/2,j,k+1/2}^{\overline{xz}} = \overline{\rho}_{i+1/2,j+1/2,k}^{\overline{xy}} = \overline{\rho}_{i+1/2,j+1/2,k+1/2}^{\overline{xyz}},$$

$$\overline{R}_{i,j+1/2,k+1/2}^x = \overline{R}_{i+1/2,j,k+1/2}^y = \overline{R}_{i+1/2,j+1/2,k}^z = \delta_x (u_{i+1/2,j+1/2,k+1/2} \overline{\rho}_{i+1/2,j+1/2,k+1/2}) + \\ + \delta_y (v_{i+1/2,j+1/2,k+1/2} \overline{\rho}_{i+1/2,j+1/2,k+1/2}) + \delta_z (w_{i+1/2,j+1/2,k+1/2} \overline{\rho}_{i+1/2,j+1/2,k+1/2})^{\overline{xyz}}.$$

The difference analogue of the Ertel potential vorticity has the following form:

$$\begin{aligned} \varpi_{i+1/2, j+1/2, k+1/2} = & \overline{\xi_{i+1/2, j+1/2, k+1/2}^x} \delta_x \overline{\rho_{i+1/2, j+1/2, k+1/2}^{-yz}} + \overline{\xi_{i+1/2, j+1/2, k+1/2}^y} \delta_y \overline{\rho_{i+1/2, j+1/2, k+1/2}^{-xz}} + \\ & + \overline{\xi_{i+1/2, j+1/2, k+1/2}^z} \delta_z \overline{\rho_{i+1/2, j+1/2, k+1/2}^{-xy}} = \varpi^x + \varpi^y + \varpi^z, \end{aligned} \quad (32)$$

where the designations $\varpi^x, \varpi^y, \varpi^z$ are obvious.

The difference between equation (31) and equation (45) in [7] is not only that viscosity and diffusion are taken into account, but also that the components of the absolute velocity vortex have the form (28).

Numerical analysis of components of the potential vorticity equation based on calculation results of circulation with atmospheric conditions for 2011.

In numerical forecasting experiments, the following parameters were set. Calculations were carried out with a uniform step along horizontal coordinates of 1.6 km; 27 horizons were used vertically with condensation in the upper sea layer. Accounting for the runoff of the Black Sea rivers and flows through the Bosphorus and Kerch Straits (conditions (9)–(13)) corresponded to the data in [11]. The water temperature at the mouths of rivers (conditions (11)–(12)), except for the rivers of Turkey, was set from [11]. It was assumed that the temperature of the Turkish rivers is equal to the temperature of the coastal sea waters. In the Upper Bosphorus Current, the temperature and salinity were assumed to be the same as in the sea, in accordance with conditions (11). In the Lower Bosphorus stream, the salinity was taken to be 35‰ with the temperature of 16 °C.

SKIRON data for 2011 [12] were used to set the atmospheric effect in equations (7), (8); based on the Mellor–Yamada theory [8], vertical mixing was described. The initial conditions (14) in this calculation corresponded to 1 January 2011. The calculation was carried out for a year of model time, its parameters and results are described in detail in [13].

As an example, the PV is considered (formula (32)) for two points in time – winter (Fig. 2, *a*) and summer (Fig. 2, *b*) periods, when the circulation structure is noticeably different.

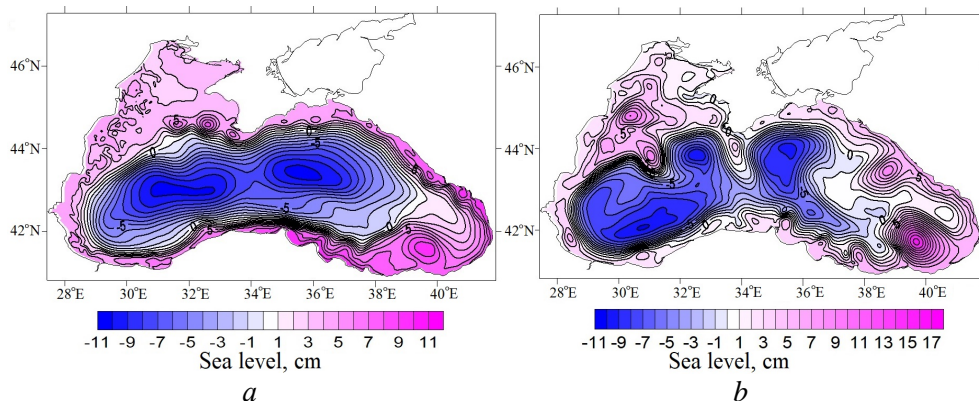


Fig. 2. Specified sea level on 1 February (*a*) and 1 August (*b*) 2011

As of 1 January 2011, the specified sea level was an extensive cyclonic gyre with two synoptic eddies – the Sevastopol and the southwestern anticyclones. In contrast to the winter circulation, the cyclonic circulation splits into two in the summer season (Fig. 2, *b*). In the western part of the basin along the deep slope, the Black Sea Rim Current spreads in the form of a narrow jet current (Fig. 2, *a*). In winter, powerful meanders form along the northern periphery of the northwestern shelf and an intense anticyclone forms in the southeastern corner of the sea.

Winter circulation corresponds to the potential vorticity shown in Fig. 3, *a – d*. There are qualitative differences in its structure in depth. In the upper 30-meter layer, large PV values are concentrated in two areas (Fig. 3, *a, b*). The first is the northwestern part of the sea, limited approximately by coordinates 44°–46°N, 29°–31°E, where water dynamics is largely determined by the river runoff, primarily the Danube. Therefore, there are large spatial gradients in the density field, which determine ϖ values in this sea area. The second area is a deep slope, where the Anatolian coast and the southern periphery of the northwestern shelf stand out (Fig. 3, *b*).

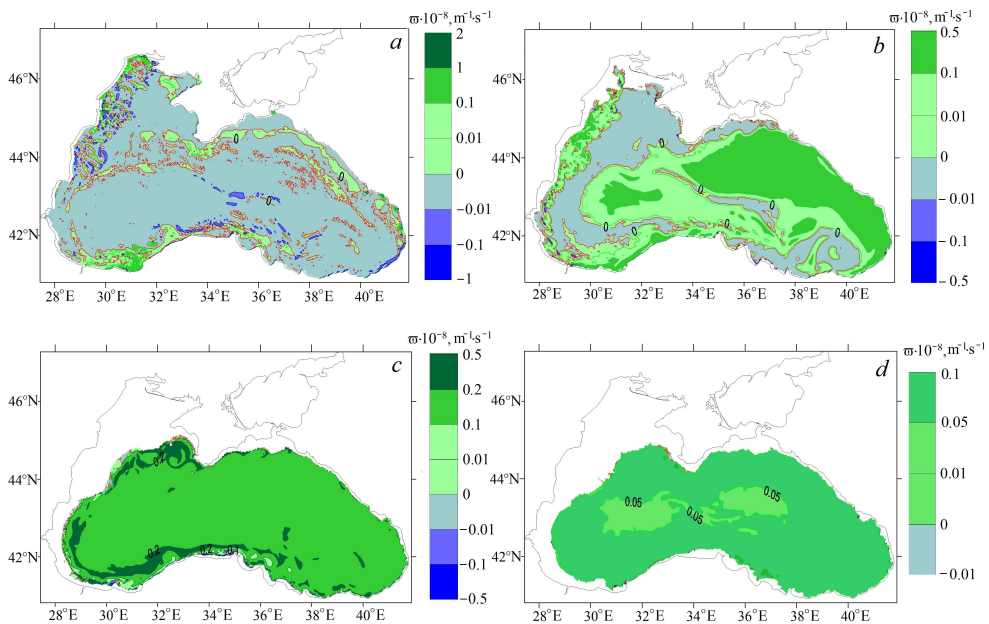


Fig. 3. PV at horizons 3.75 (*a*), 35 (*b*), 106.25 (*c*) and 350 m (*d*) on 1 February 2011

In the area of the Sevastopol and the southwestern vortex, no extreme values of ϖ are observed. The reason is that it is a scalar quantity equal to the product of density gradient and absolute velocity vortex and, therefore, its large value does not necessarily mean an increase in vorticity and, moreover, its sign does not determine the vortex rotation sign [2]. Below the upper 50-meter layer, the highest values of ϖ in the coastal strip are observed (Fig. 3, *c, d*). Local maxima are concentrated in

relatively small zones (~ 10 km), which are clearly visible at a depth of 100 m (Fig. 3, *c*). In the central part of the sea, the PV structure is quite homogeneous in space.

An illustration for the PV analysis is its calculation for summer period, when the circulation is less regular and its vortex structure is more pronounced (see Fig. 2, *b*). Two features appear in the structure of potential vorticity in August 2011. The band of small values $\overline{\omega}$ in the upper layer (Fig. 4, *a*, *b*) corresponds to the region of greatest mixing along the vertical density field, that is, the value $\delta_z \overline{\rho}^{\overline{xy}}$ is very small – two to three orders of magnitude less than vertical density gradients of the surrounding water. The second feature is a homogeneous structure and low PV values in areas approximately corresponding to the cores of the southeastern anticyclone, southwestern and eastern gyres. These features are also determined by the structure $\delta_z \overline{\rho}^{\overline{xy}}$, which varies slightly over space. This type of potential vorticity in central parts of gyres is consistent with the conclusions of the work [4], where the PV reconstructed from observational data in the Lofoten gyre area has a similar structure. On the lower horizons (Fig. 4, *c*, *d*) along the area boundary, there is a narrow band of heterogeneous values due to differences in the bottom topography; a small spatial variability of this value is observed in the central part.

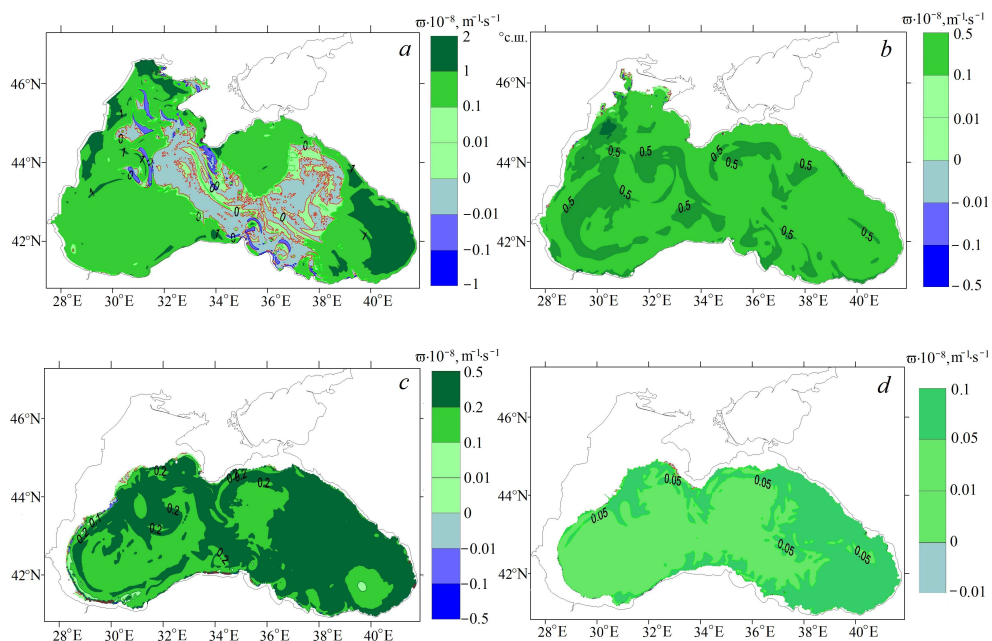


Fig. 4. PV at horizons 3.75 (*a*), 35 (*b*), 106.25 (*c*) and 350 m (*d*) on 1 August 2011

The main contribution to the vortex structure, as a rule, is made by the component $\overline{\omega}^z$ [4]. Its magnitude is determined by the quasi-geostrophic nature

of the movement and the vertical stratification of sea water. In areas where there is an inflow of fresh (river mouths) or salt (straits) waters, horizontal components of potential vorticity may be of predominant importance. As an example, Fig. 5 shows the values at horizons of 3.75 and 106.25 m.

Comparison of Fig. 5, *a*, *c*, *e* and 3, *a* shows that horizontal component ϖ^x (Fig. 5, *a*) makes the main contribution in the zone of the Danube fresh water inflow in the northwestern part of the sea, in the rest of the area ϖ^z determines vortex structure (Fig. 5, *e*).

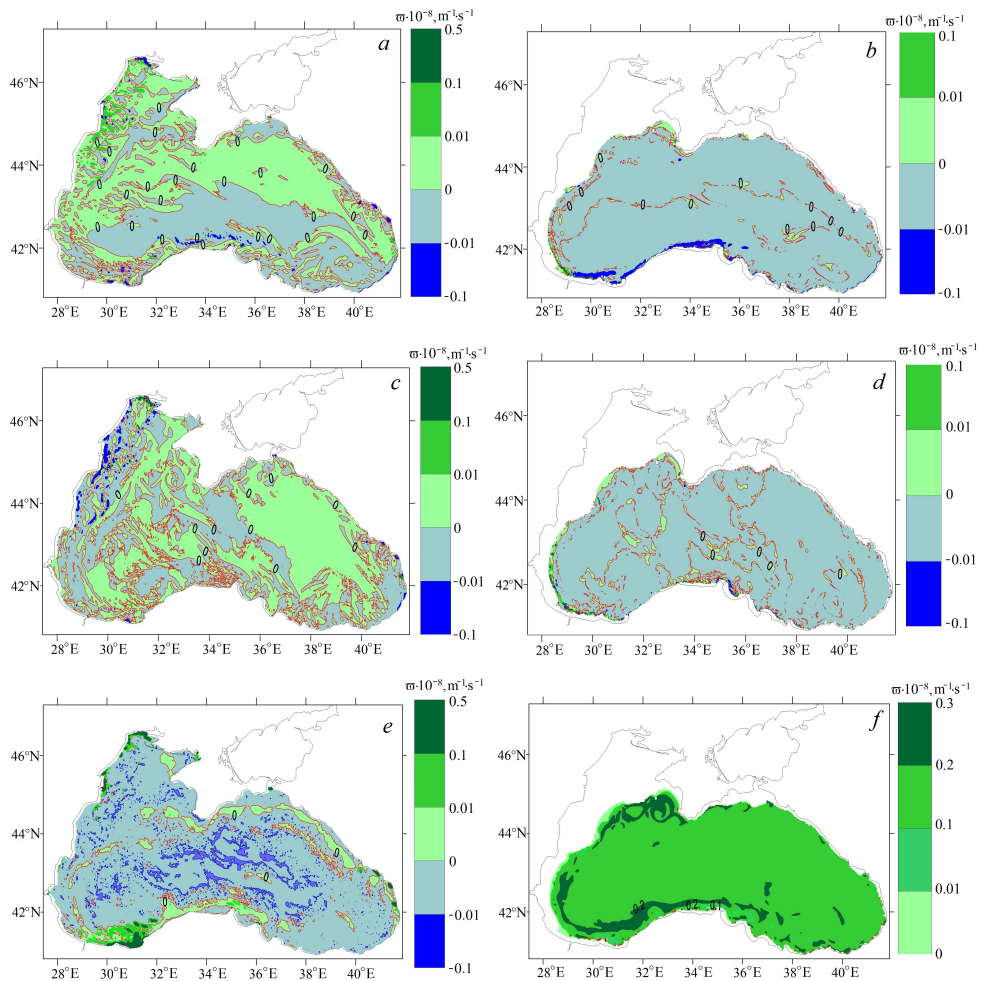


Fig. 5. PV components: ϖ^x at horizons 3.75 (*a*) and 106.25 m (*b*); ϖ^y at horizons 3.75 (*c*) and 106.25 m (*d*); ϖ^z at horizons 3 (*e*) and 106.25 m (*f*) on 1 February 2011

At the horizon 106.25 m (Fig. 5, *b*, *d*, *f*), the vertical component is larger than ϖ^x (Fig. 5, *b*) and ϖ^y (Fig. 5, *d*), so it (Fig. 5, *f*) quite accurately determines potential vorticity type at the horizon 106.25 m (see Fig. 3, *c*).

Direct calculations establish that in the upper layer of the sea the form of the component ϖ^z corresponds qualitatively to $\delta_z \bar{\rho}^{-xy}$, but its absolute value is several orders of magnitude smaller than $\bar{\xi}^z$. In turn, the absolute vortex structure is quite homogeneous and positive, therefore, when $\delta_z \bar{\rho}^{-xy}$ is multiplied by the potential vorticity structure $\bar{\xi}^z$, it characterizes $\delta_z \bar{\rho}^{-xy}$ and its quantitative value depends on $\bar{\xi}^z$. The value $\bar{\xi}^z$ is determined by two terms – relative and planetary vorticity. If we evaluate f^z contribution to the absolute vortex, f^z is comparable in magnitude to the relative vortex and increases the values of $\bar{\xi}^r$. On average, the $\bar{\xi}^z$ magnitude is two orders of magnitude larger than $\delta_z \bar{\rho}^{-xy}$. During this season, as a result of winter convection, the factor due to the vertical density gradient in the upper layer of the sea is small, with the exception of the river runoff area, where its value can be significant.

At the horizon of 106.25 m (Fig. 5, *f*), both factors are positive and $\bar{\xi}^z$, on average, is smaller by several orders of magnitude. PV variability is observed in the coastal area; PV is homogeneous in the central part of the sea. It should be noted that, firstly, at the lower horizons (approximately below 50 m depth) the relative vortex is in absolute value smaller than f^z . Secondly, since the integral over the horizontal surface of $\bar{\xi}^r$, whose difference from zero is determined by the river runoff and the water exchange through the straits, is small, then the $\bar{\xi}^r$ structure contains zones of cyclonic and anticyclonic rotation of waters. At the same time, planetary vorticity is positive and greater than $\bar{\xi}^r$ and, therefore, it determines quantitative values of PV with corrections introduced by the relative vortex to the qualitative structure of potential vorticity at deep horizons.

Let us consider the contribution of nonlinear forces to evolution of ϖ . The following designations are introduced:

$$C^x = \delta_x (Y^x \bar{\rho}^{-yz}) + \delta_x (\xi^x R^x) = C_1^x + C_2^x, \quad C^y = \delta_y (Y^y \bar{\rho}^{-xz}) + \delta_y (\xi^y R^y) = C_1^y + C_2^y, \\ C^z = \delta_z (Y^z \bar{\rho}^{-xy}) + \delta_z (\xi^z R^z) = C_1^z + C_2^z, \quad C^S = C^x + C^y + C^z.$$

The main contribution to the temporal evolution of PV is made by nonlinear forces in the upper layer in the coastal sea area (Fig. 6, *a, b*). Their contribution is different for various areas: it is greater in the northwestern part (Fig. 6, *a*) and along the Anatolian coast (Fig. 6, *b*). The estimates show that their quantitative differences in absolute value between the central part of the sea and its periphery are several

orders of magnitude. At the lower horizons (Fig. 6, *c, d*), the largest values of the nonlinear terms in Ertel's equation are concentrated in the form of a narrow alongshore strip with a more pronounced character near the southern coast.

Let us consider the contribution of individual terms C^x, C^y, C^z into C^S .

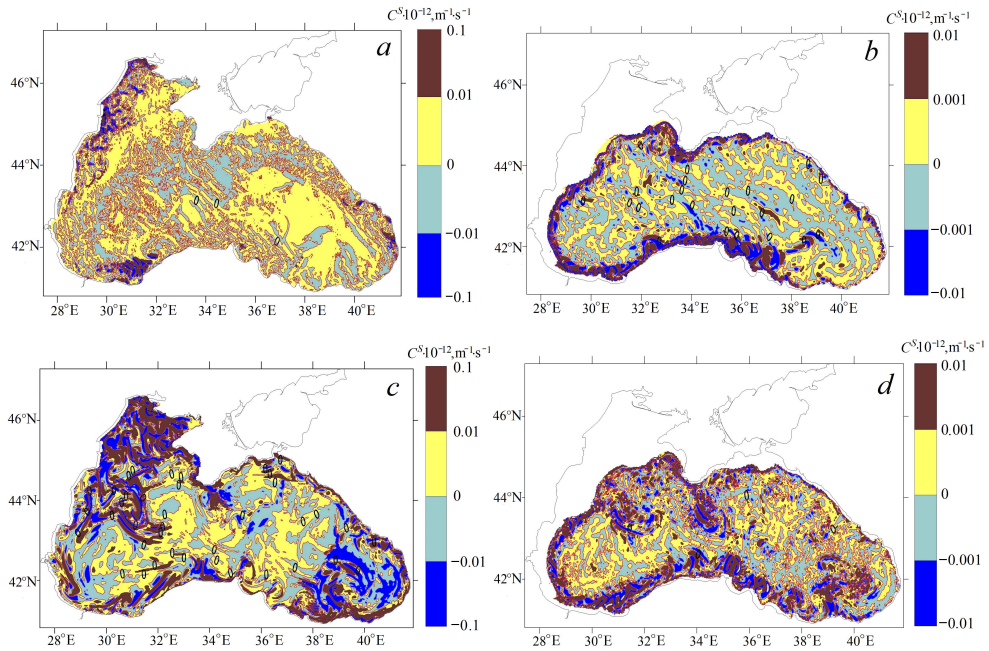


Fig. 6. C^S at horizons 3 (*a*) and 106.25 m (*b*) on 1 February 2011, and at horizons 3.75 (*c*) and 106.25 m (*d*) on 1 August 2011

In the upper layer (Fig. 7, *a, c, e*), areas of large absolute values C^x, C^y, C^z have a similar structure. In the southeastern corner of the basin and in the northeastern part of the sea, limited by coordinates $42^\circ - 44^\circ\text{N}$, $37^\circ - 39^\circ\text{E}$ etc., areas of C^x, C^y, C^z values close to zero are observed. The calculated average and maximum C^x, C^y, C^z values (Fig. 7, *a, c, e*) in comparison with C^S (Fig. 6, *a*) indicate that the extreme values differ by an order of magnitude, the average values – by two orders of magnitude. This means that C^x, C^y, C^z are mutually compensated and the result is the structure shown in Fig. 6, *a*. The direct calculations establish that the main contribution to the nonlinear terms C^x, C^y, C^z in the upper layer is made by C_1^x, C_1^y, C_1^z accordingly, that is $\delta_x(Y^x \bar{\rho}^{yz}), \delta_y(Y^y \bar{\rho}^{xz}), \delta_z(Y^z \bar{\rho}^{xy})$. The estimate of the order of magnitude shows that C^S is on average two orders of magnitude less than each of the terms C^x, C^y, C^z .

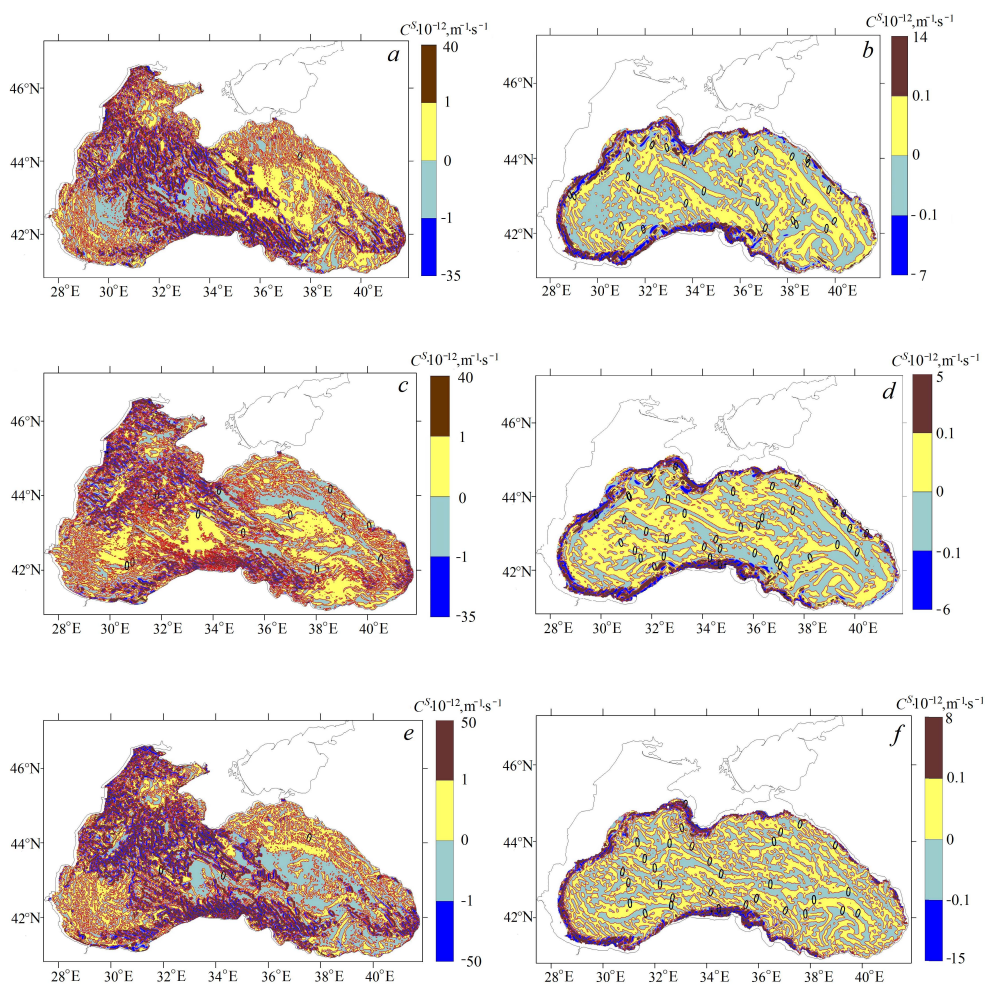


Fig. 7. Components: at horizons 3.75 (a) and 106.25 m (b), at horizons 3.75 (c) and 106.25 m (d) and at horizons 3.75 (e) and 106.25 m (f) on 1 February 2011

A similar situation occurs for the calculated fields as of 1 August 2011.

Conclusion

For a system of discrete equations of sea dynamics in the hydrostatic approximation and taking into account viscosity, diffusion, a finite-difference equation for the potential vorticity of a stratified incompressible fluid is obtained. Just as in the more general case, it has a divergent appearance and differs from its differential counterpart. Because a nonlinear state is used to calculate the density, the resulting discrete equation for PV is not an exact consequence of the finite-difference equations of the model. Additional research to estimate the influence of the nonlinear nature of the equation of state on the results obtained is needed.

Analysis of the magnitude of potential vorticity itself confirmed previously obtained results that its vertical component is the main one. Horizontal components

make a noticeable contribution in river runoff areas, water exchange through straits and in zones of sharp density field gradients. The qualitative appearance of PV in the upper layer of the sea has similar features recorded from observational data. The homogeneous structure for the central part of the vortex formations and the intense nature in the area of large transverse gradients in the density field in the frontal zones determine potential vorticity structure. In the deep layers of the sea, its highest values are concentrated in the form of a narrow coastal strip; in the rest of the sea, PV values are small.

Calculation of ϖ^z components in winter on the upper horizons showed that in the upper layers of the sea, except coastal zones of river runoff, ξ^z is determined, which is the sum of the relative vortex and f^z (value of approximately the same order). In the lower layers of the sea, the quantitative values of PV are determined to a greater extent by planetary vorticity and its qualitative features – by the relative vortex structure.

From the analysis of nonlinear terms in the PV equation, it follows that in the upper layer of the sea the main contribution to the advection of potential vorticity C^S is made in the northwestern part and along the Anatolian coast. At lower horizons, the highest C^S values are observed along the coastal strip with a more pronounced character near the southern coast of the sea, which corresponds to the PV structure.

The calculation of C^x, C^y, C^z terms for winter and summer periods enabled to establish two facts. Firstly, the magnitude of each C^x, C^y, C^z is determined by $\delta_x(\Upsilon^x \bar{\rho}^{-yz}), \delta_y(\Upsilon^y \bar{\rho}^{-xz}), \delta_z(\Upsilon^z \bar{\rho}^{-xy})$, that is, by the divergence from the product of nonlinear terms in the equations of motion and density. Secondly, C^S is one and a half to two orders of magnitude less than each of C^x, C^y, C^z components, that is, locally, the total sum of the vertical and horizontal advection of potential vorticity is two orders of magnitude less than each separately. A possible explanation for this result is as follows. Assume that the finite-difference analogues of the nonlinear terms in the PV equation are close to the differential form $\text{div}(\bar{U}\omega)$. Then, representing $\omega = \omega^S + \varpi^*$, where ω^S is a quantity averaged over space, at each point of the domain we have $\text{div}(\bar{U}\omega^S) = \omega^S \text{div}(\bar{U}) = 0$ or close to zero. Since the time variability of potential vorticity depends predominantly on $\text{div}(\bar{U}\omega^*)$, mutual compensation of nonlinear components along x, y, z occurs when calculating PV advection.

The general nature of the results obtained is a matter for further research.

REFERENCES

1. Ertel, H., 1942. Ein Neuer Hydrodynamischer Wirbelsatz. *Meteorologische Zeitschrift*, 59(9), pp. 277-281. <https://doi.org/10.1127/0941-2948/2004/0013-0451> (in German).
2. Müller, P., 1995. Ertel's Potential Vorticity Theorem in Physical Oceanography. *Reviews of Geophysics*, 33(1), pp. 67-97. <https://doi.org/10.1029/94rg03215>
3. Kurgansky, M.V. and Pismichenko I.A., 2000. Modified Ertel's Potential Vorticity as a Climate Variable. *Journal of the Atmospheric Sciences*, 57(6), pp. 822-835. [https://doi.org/10.1175/1520-0469\(2000\)057<0822:MESPVA>2.0.CO;2](https://doi.org/10.1175/1520-0469(2000)057<0822:MESPVA>2.0.CO;2)
4. Zhmur, V.V., Novoselova, E.V. and Belonenko, T.V., 2021. Potential Vorticity in the Ocean: Ertel and Rossby Approaches with Estimates for the Lofoten Vortex. *Izvestiya, Atmospheric and Oceanic Physics*, 57(6), pp. 632-641. <https://doi.org/10.1134/S0001433821050157>
5. Rossby, C.-G., 1940. Planetary Flow Patterns in the Atmosphere. *Quarterly Journal of the Royal Meteorological Society*, 66(S1), pp. 68-87. <https://doi.org/10.1002/j.1477-870X.1940.tb00130.x>
6. Hoskins, B.J., McIntyre, M.E. and Robertson, A.W., 1985. On the Use and Significance of Isentropic Potential Vorticity Maps. *Quarterly Journal of the Royal Meteorological Society*, 111(470), pp. 877-946. <https://doi.org/10.1002/qj.49711147002>
7. Demyshev, S.G., 2024. Finite-Difference Approximation of the Potential Vorticity Equation for a Stratified Incompressible Fluid and an Example of its Application for Modeling the Black Sea Circulation. Part I. Finite-Difference Equation of Potential Vorticity of Ideal Fluid. *Physical Oceanography*, 31(2), pp. 149-160.
8. Mellor, G.L. and Yamada, T., 1982. Development of a Turbulence Closure Model for Geophysical Fluid Problems. *Reviews of Geophysics*, 20(4), pp. 851-875. <https://doi.org/10.1029/RG020i004p00851>
9. Arakawa, A. and Lamb, V.R., 1981. A Potential Enstrophy and Energy Conserving Scheme for the Shallow Water Equations. *Monthly Weather Review*, 109(1), pp. 18-36. [https://doi.org/10.1175/1520-0493\(1981\)109<0018:APEAEC>2.0.CO;2](https://doi.org/10.1175/1520-0493(1981)109<0018:APEAEC>2.0.CO;2)
10. Demyshev, S.G., 2005. Numerical Experiments Aimed at the Comparison of Two Finite-Difference Schemes for the Equations of Motion in a Discrete Model of Hydrodynamics of the Black Sea. *Physical Oceanography*, 15(5), pp. 299-310. <https://doi.org/10.1007/s11110-006-0004-2>
11. Simonov, A.I. and Altman, E.N., eds., 1991. *Hydrometeorology and Hydrochemistry of Seas in the USSR. Vol. IV. Black Sea. Issue 1. Hydrometeorological Conditions*. St. Petersburg: Gidrometeoizdat, 428 p. (in Russian).
12. Kallos, G., Nickovic, S., Papadopoulos, A., Jovic, D., Kakaliagou, O., Misirlis, N., Boukas, L., Mimikou, N., Sakellaris [et al.], 1997. The Regional Weather Forecasting System SKIRON: An Overview. In: G. B. Kallos, V. Kotroni and K. Lagouvardos, eds., 1997. *Proceedings of the Symposium on Regional Weather Prediction on Parallel Computer Environments (Athens, 15-17 October 1997)*. Athens, Greece: University of Athens, pp. 109-122.

13. Demyshev, S.G. and Dymova, O.A., 2018. Numerical Analysis of the Black Sea Currents and Mesoscale Eddies in 2006 and 2011. *Ocean Dynamics*, 68(10), pp. 1335-1352. <https://doi.org/10.1007/s10236-018-1200-6>

About the author:

Sergey G. Demyshev, Head of Wave Theory Department, Chief Research Associate, Marine Hydrophysical Institute of RAS (2 Kapitanskaya Str., Sevastopol, 299011, Russian Federation), DSc (Phys.-Math.), **Scopus Author ID: 6603919865**, **ResearcherID: C-1729-2016**, **ORCID ID: 0000-0002-5405-2282**, demyshev@gmail.com

The author has read and approved the final manuscript.


The author declares that he has no conflict of interest.

Original article

Errors in Calculating Density Using the CTD probe data in Suboxic Layer of the Black Sea

N. Yu. Andrulionis , O. I. Podymov

P. P. Shirshov Institute of Oceanology of RAS, Moscow, Russian Federation

 natalya@ocean.ru

Abstract

Purpose. The purpose of this work is to study the density of water in two ways in the suboxic layer of the Black Sea, to assess errors in calculating density using a standard method based on hydrophysical equipment data, to compare the results obtained with other characteristics of sea waters and to analyze the causes of these errors.

Methods and Results. The waters of the Black Sea suboxic layer were studied in May 2021 and October 2022. Water density was measured with a high-precision laboratory density meter and calculated from the CTD probe data using electrical conductivity by the EOS-80 equation of state. The turbidity values were measured by a turbidimeter while sampling. The concentrations of major ions of the major ion-salt composition in the studied samples were determined by a potentiometric titration, and their difference from the standard sea water IAPSO was assessed in the laboratory. The assessing procedure showed that, as compared to the standard sea water, the contents of SO_4^{2-} and HCO_3^- were higher on average by 0.2 and 0.6%, respectively, both K^+ and Ca^{2+} – by 0.2%, and the contents of Cl^- and Na^+ were lower on average by 0.4 and 0.3%, respectively. The content of Mg^{2+} was close to its content in standard sea water. It was found that within the range of conditional density (σ_t) 15.9–16.2 kg/m³, the vertical distribution of major ions was not linear, especially in relation to chlorides and sulfates.

Conclusions. As a result of determining the density of the waters of the suboxic layer of the Black Sea in two ways and comparing the obtained values, it was found that the errors in calculating the density according to the CTD probe data amount to 0.05–0.2 kg/m³ and are due to variations in the ion-salt composition and the presence of a large suspension concentrations. The density gradient measured by a density meter is approximately twice as large as that measured by a CTD probe.

Keywords: Black Sea, suboxic layer, water density, water salinity, density measurement, CTD sounding, hydrochemical characteristics of water, ionic composition

Acknowledgments: The research was carried out with the support of Ministry of Education and Science of Russian Federation, Agreement No. 07-15-2021-941. The authors are grateful to Senior Researcher of Andreyev Acoustics Institute and Chief Specialist of IO RAS V. A. Soloviev for his assistance in studies and preparation of the paper.

For citation: Andrulionis, N.Yu. and Podymov, O.I., 2024. Errors in Calculating Density Using the CTD probe data in Suboxic Layer of the Black Sea. *Physical Oceanography*, 31(3), pp. 336-349.

© 2024, N. Yu. Andrulionis, O. I. Podymov

© 2024, Physical Oceanography

Introduction

Since the late 20th century, salinity measurements have been carried out mainly using CTD (conductivity, temperature, depth) probes and have been based on the ratio of seawater electrical conductivity to the conductivity of a special seawater reference sample (IAPSO Standard Seawater) (hereinafter SSW) [1]. The relationship between density, temperature, salinity and pressure is determined by the EOS-80 equation of state and salinity is calculated from electrical conductivity. Accurate salinity calculation from electrical conductivity is possible if



the relative major ion-salt composition (MIC) of seawater is constant and violation of this constancy leads to errors. The MIC undergoes some changes, leading to a variation of the electrical conductivity – salinity – density relationship, which is currently most accurately determined only for SSW obtained from a certain region of the North Atlantic. Research reveals that SSW may have chemical anomalies [2] and its electrical conductivity may vary slightly from batch to batch [3]. Variation in the electrical conductivity – salinity – density relationship is a source of error when determining seawater thermodynamic properties using the *EOS-80* equation of state, since electrical conductivity directly depends on the seawater ionic components and, to a greater extent, on the major ions [2–4]. The greatest differences between the relative MIC and the SSW composition are observed in deep ocean waters due to dissolution of carbonates, silicates and oxidation of plant residues, etc. [5, 6], in waters with high dissolved organic carbon concentrations and total alkalinity. The most pronounced ion variations are in such parts of the World Ocean as estuaries, basins with anoxic zones, as well as in thermal springs, evaporation basins, etc. [4, 5, 7].

Unlike most seas, the Black Sea has a clearly defined two-layer structure of the water column with oxic and anaerobic layers. Low-salinity waters are located in the upper sea layer, high-salinity waters – in the lower layer. Thermohaline properties of the upper layer are affected by river runoff and interaction with the atmosphere on various time scales; the properties of the lower layer depend on the influence of Marmara (Mediterranean) waters entering with the Lower Bosphorus Current, as well as vertical exchange processes [8, 9].

There is a layer of the main pycnocline (density gradient) waters between the upper and lower main layers, which differs in salinity and density from the above- and underlying layers. It is a boundary of vertical convective mixing and maintains vertical separation of oxic, suboxic and anoxic waters of the Black Sea [10]. Vertical distribution of oxygen and hydrogen sulfide depends on the depth and characteristics of the main pycnocline, which determines the existence of oxidized and restored forms of various elements: carbon, nitrogen, sulfur, manganese, iron and others. The vertical distribution of oxygen in the Black Sea is quite strongly related to density stratification [10, 11]. The main pycnocline, due to high density gradients, significantly limits the intensity of vertical turbulent exchange, and therefore the oxygen flux into deeper water layers, and is the cause for the existence of cold intermediate layer (CIL) determining its properties.

There is an oxycline below the CIL, where oxygen concentration decreases. The lower oxycline boundary corresponds to a sharp change in the vertical gradient of oxygen concentration and the density σ_t in this layer is 15.2–16.0 [12].

A suboxic layer is located below the oxycline. It was first described in [13] and its study has been the subject of many scientific papers. A suboxic layer, or zone, begins at $\sigma_t = 15.6$ – 15.9 kg/m³ and its occurrence is explained by the features of forming vertical and horizontal O₂ fluxes, vertical fluxes of suspended organic matter and H₂S. In this zone, a complex chain of redox transformations occurs through bacteria in the process of sulfate reduction, in the process of chemosynthesis, mainly involving manganese compounds, as well as nitrogen

removal (denitrification and anammox). [14, 15]. There is also a layer with an increased turbidity value; the main element of suspension mineral component is insoluble manganese oxide (MnO_2) [16, 17].

Numerous studies of complex hydrochemical structure of the Black Sea indicate significant differences in the MIC of its waters from the MIC of the World Ocean waters and IAPSO Standard Seawater, which leads to errors in calculations with the *EOS-80* equation [16–19]. This conclusion is also valid when using the *TEOS-10* equation (thermodynamic equation of state), if it was not appropriately amended by taking into account hydrochemical anomalies of macrocomponent composition relative to the SSW composition, as recommended, for example, in [20]. Complex biogeochemical processes leading to metamorphization of ionic composition in the suboxic layer can contribute to a significant underestimation of electrical conductivity values here and, therefore, salinity and density.

Previous studies of the Black Sea suboxic layer suggest that the density in this layer increases sharply – it has a leap. Then the presence of a frequently occurring layer of increased turbidity there can be explained by the presence of the largest density gradient, as was previously assumed [5, 20]. This prevents rapid deposition and dispersion of suspended particles in the water column. This study expands the understanding of the degree of biogeochemical processes influence on the seawater physical properties under non-oceanic conditions and the accuracy of their determination. Ionic variations in the deep-water composition affect the conductivity – density relationship and even small density variations can affect global circulation of ocean waters along constant-density surfaces.

This paper is purposed at studying the water density of the Black Sea suboxic layer using two methods to identify errors in determining density from CTD probe data using the *EOS-80* equation of state, as well as to compare the results obtained with other seawater characteristics and analyze the causes of these errors. To achieve these goals, the following tasks were set: study the MIC of each sample, compare it with the composition of SSW and evaluate the differences found; calculate salinity values from the sum of major ions, compare them with the values determined from the CTD probe data and calculate deviations. The obtained density and salinity values were compared with the turbidity profile and major chemical composition of the water from the samples under study.

Materials and methods

Water sampling and measurements were carried out at the Black Sea test site of P.P. Shirshov Institute of Oceanology of RAS in the Black Sea suboxic layer in the continental slope area with a maximum depth of 1300 m; sampling and measurements were taken from R/V *Ashamba* on 26 May 2021 and 13 October 2022. A total of 12 samples were taken – per 6 each year. Station coordinates: in 2021 – 44.51667°N, 37.90967°E, in 2022 – 44.51775°N, 37.90723°E. The samples were taken along isopycnals, which were located at appropriate depths during the sampling (Table 1).

Table 1

Isopycnals and depths recorded by CTD probe at the time of sampling

Depth, m	σ_t , kg/m ³	Depth, m	σ_t , kg/m ³
2021		2022	
142.2	15.86	140.6	15.92
148.1	15.98	148.1	15.99
151.3	16.04	152.6	16.05
155.1	16.09	157.3	16.11
159.4	16.15	161.4	16.16

The sampling was carried out with six 4-liter plastic Niskin bathometers mounted on a rosette equipped with an SBE 19plus CTD probe. The water samples from the bathometer were placed in sealed 1-liter containers and transported to the laboratory for subsequent analysis. Deionized water (electrical conductivity less than 0.2 $\mu\text{S}/\text{cm}$) was applied to prepare reagent solutions and dilute samples. The analyzed sample mass was measured by weighing on OHAUS laboratory analytical balances of the first accuracy class with an error of 0.001 g.

Density determination. During the sampling, seawater electrical conductivity was measured using a SeaBird 19plus CTD probe. The density from CTD data is calculated using the EOS-80 equation of state developed for ocean waters with a certain ion-salt composition. The effect of ion-salt composition variations on the accuracy of determining salinity in seawater was studied in [2, 20] and in water bodies with a composition significantly different from the oceanic one – in [21].

The water density of the studied samples was measured in the laboratory by Anton Paar DMA 5000M (Austria) precision density meter (DMA) at *in situ* temperature and atmospheric pressure. The similar device has been used as instrument from this manufacturer when developing the new thermodynamic equation of seawater state TEOS-10 [22, 23]. The samples were first filtered through GF/F Whatman membrane filter of 0.7 μm pore size to remove mineral and organic suspended matter and placed in glass containers of 250–300 ml volume. The instrument was calibrated according to the instructions. The error¹ of water density measuring was $\pm 10^{-5}$ g/cm³. Standard deviations during density measuring did not exceed $0.02 \cdot 10^{-3}$ g/cm³.

To assess the density meter accuracy, a study on SSW sample from Osil P162 (batch 162) was carried out. Modern studies of salinity of SSW various batches and assessment of their calibration accuracy, including sample P162, are discussed in [3]. The results of recent studies demonstrating high accuracy of DMA-series Anton Paar density meter are presented in [24]. The SSW density values obtained from the density meter were compared with the ones calculated using EOS-80 and TEOS-10. The density meter values differed from those calculated using EOS-80 and TEOS-10 by an average of 0.003 kg/m³, which is within the measurement error.

¹ Anton Paar, 2010. *Operating Manual DMA 4100 M, DMA 4500 M, DMA 5000 M*. Software Version: V1.70. Copyright. Anton Paar GmbH. Graz, Austria, 135 p.

This result corresponds to the conclusion from [24, p. 4] that “the results for IAPSO P160 water agree with TEOS-10 within the present measurement uncertainty”.

Density data in the work were compared in conditional density units σ_t (kg/m³) for consistency with literature sources. It is worth noting that at the depths under study, σ_t deviations from potential density σ_θ do not exceed thousandths, and *in situ* temperature differs from potential temperature by hundredths of a degree. These values are within the error range of the measuring instruments used.

Turbidity determination. During sampling, turbidity values in NTU (nephelometric turbidity unit) were measured using a Seapoint turbidimeter.

Determination of ion-salt composition. Concentrations of the major salt composition components of the samples under study (Cl^- , SO_4^{2-} , HCO_3^- , Na^+ , K^+ , Ca^{2+} , Mg^{2+}) were determined in accordance with the methods selected for the hyperhaline water analysis [21], but with regard to the Black Sea water mineralization. Reagent solutions were prepared at lower concentrations compared to that of reagent solutions for the analysis of hyperhaline waters. For example, to determine total dissolved inorganic carbon (T_{CO_2}) [25], which was calculated in grams per kilogram as HCO_3^- , we took a 0.05 M HCl solution, sulfates were titrated with 0.01 M and 0.05 M BaCl_2 solutions and chlorides – with 0.05 M solution of silver nitrate. To determine calcium and magnesium content, we used an EDTA solution (disodium salt of ethylenediaminetetraacetic acid, Trilon-B) of 0.05 M concentration. The amount of sample for analysis was adjusted as necessary. The concentrations of Cl^- , SO_4^{2-} , HCO_3^- , Ca^{2+} and Mg^{2+} were determined by potentiometric titration, K^+ – gravimetrically. Na^+ concentration was determined as the difference between the sum of anions and cations in mole equivalents. This method provides good results in case all other ions are determined with sufficiently high accuracy² [6, 26, 27]. Similar composition studies were carried out on a sample (SSW) with a practical salinity of 34.993, which was analyzed in the laboratory of P.P. Shirshov Institute of Oceanology of RAS (IO RAS) and had good agreement with the composition published in [27]. The deviations of the ion sum in the SSW from the work [27] from the ion sum obtained in the IO RAS laboratory amounted to 0.3%. This is equivalent to 0.06 g/kg for water samples from the Black Sea with a salinity of 21.

Study of the major ion concentration made it possible to determine the total mineralization of water samples, as well as to calculate an important hydrochemical characteristic of the basin – sulfate-chlorine ratio ($\text{SO}_4^{2-}/\text{Cl}^-$).

The work presents the values of major ion relative contribution to the total mineralization of each studied water sample from the Black Sea suboxic layer. The obtained values are compared with those for SSW.

Table 2 presents standard deviations when measuring the concentration of major ions in the Black Sea water, expressed as a percentage of the average mass values.

² Federal Service of Russia for Hydrometeorology and Environmental Monitoring, 1993. *Guide to the Chemical Analysis of Sea Waters: RD 52.10.243-92*. Saint Petersburg: Gidrometeoizdat, p. 130. [online] Available at: http://oceanography.ru/images/stories/lmz/docs/rd_52_10_243-92.pdf [Accessed: 14 January 2019] (in Russian).

Table 2

Value of sd (%) when determining mass concentrations of major ions

σ_t , kg/m ³	Cl ⁻	SO ₄ ²⁻	HCO ₃ ⁻	Ca ²⁺	Mg ²⁺	K+
<i>May 2021</i>						
15.86	0.2	0.8	0.8	2.1	0.5	2.1
15.98	0.2	0.3	2.3	1.8	0.4	2.2
16.04	0.1	2.1	0.9	2.0	0.3	2.3
16.09	0.1	0.6	0.4	0.7	0.2	2.1
16.15	0.4	0.7	0.2	0.4	0.4	3.3
16.20	0.2	0.8	0.2	1.4	0.7	2.3
<i>October 2022</i>						
15.92	0.5	2.9	0.5	0.5	0.3	1.8
15.99	0.3	1.9	0.2	0.9	0.3	2.1
16.05	0.2	1.2	0.5	1.4	0.2	2.0
16.11	0.1	1.3	0.4	0.5	0.3	1.9
16.16	0.6	0.6	0.0	0.7	0.2	2.1
16.21	0.1	2.5	0.8	0.4	0.3	2.2

Standard deviations during sodium calculation did not exceed 0.5%. In general, the error in determining the concentrations of the major ions was hundredths of a gram.

Salinity determination. Salinity was calculated in two ways: practical salinity (SP) was calculated from the CTD probe data and practical salinity scale, as well as from the sum of major ions (SS) of the MIC. The accuracy of salinity calculation depends on the error of equipment and methods; according to [6], when calculated using electrical conductivity $\pm 0.1 \cdot 10^{-2}$ $\mu\text{S/cm}$, the sum of the major ions is $0.1 \cdot 10^{-1}$ g/kg.

Results

The results of studying water samples from the Black Sea suboxic layer, obtained in May 2021 and October 2022, are presented in Fig. 1.

Practical salinity (SP) value in 2021 according to the CTD probe data was lower than the sum of MIC components (SS) by an average of 2%, and in 2022 – by an average of 1.5%. This difference is due to the relation from [28] for ocean water:

$$SA = \frac{35.16504 \cdot SP}{35}, \quad (1)$$

where SA is absolute salinity; SP is practical salinity; 35.16504 is reference salinity value (SR). SA and SR are higher than SP by about 0.47%, since SP does not take into account carbonate content, but only the products of their decomposition – metal

oxides [28]. This is the first cause for errors in the salinity calculation from *CTD* probe data.

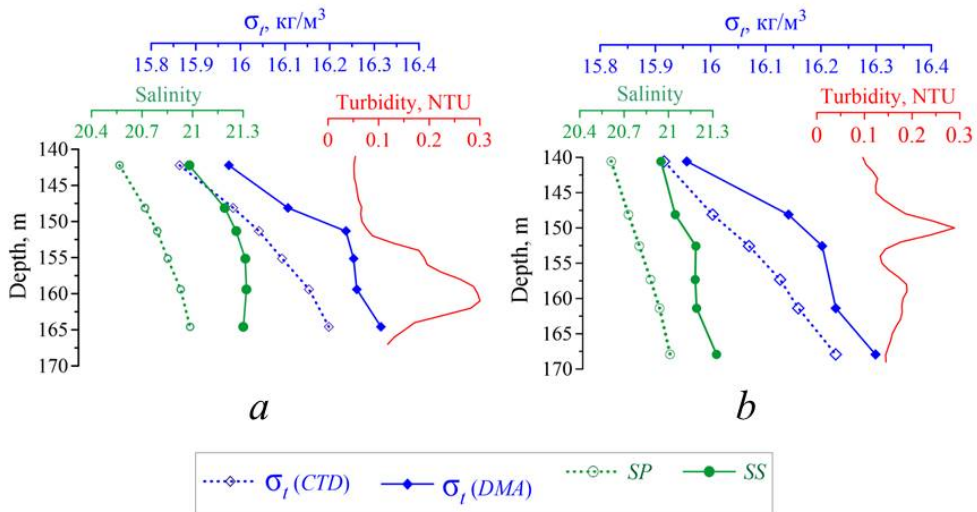


Fig. 1. Hydrophysical characteristics of water samples from the Black Sea suboxic layer: *a* – in May 2021, *b* – in October 2022. Green lines denote the results of calculating salinity and blue ones – density σ_ρ . Red line is the turbidity profile. Solid lines denote density measured by a density meter and salinity determined by a sum of major ions (SS); dotted lines indicate density and salinity calculated using the *CTD* probe data

Figure 1 shows that the density values calculated from the *CTD* probe data were lower than those measured via the density meter by 0.11–0.19 kg/m³ in 2021 and by 0.05–0.15 kg/m³ in 2022. This indicates that the density in the main pycnocline lower part actually has higher values than those calculated from electrical conductivity. In 2021, the density gradient in the suboxic zone according to the *CTD* probe was 0.02 kg/m³ per 1 m, and according to the density meter – 0.04 kg/m³ per 1 m, as well as in 2022 – 0.01 kg/m³ per 1 m and 0.02 kg/m³ per 1 m, respectively. On average, the actual density gradient in this layer was twice as large as that acquired from the *CTD* probe readings.

Fig. 1 demonstrates that a more pronounced density gradient in the suboxic zone and the upper part of the hydrogen sulfide zone is accompanied by a peak in the turbidity profile located in the region of these gradients. The turbidity peak indicates the presence of a layer of high suspended matter concentration in a given area. Suspended matter (organic and mineral) accumulation in the pycnocline region may also indicate the presence of a significant density gradient. The presence of large amounts of suspended organic matter in the Black Sea waters was noted in earlier works³ [29]. According to literature sources, this layer of increased suspended matter concentration is regularly observed in the suboxic zone. Its formation is preceded by multiple processes of water metamorphization and the main

³ Skopintsev, B.A., 1975. [Formation of the Modern Chemical Composition of the Black Sea Waters]. Leningrad: Gidrometeoizdat, 335 p. (in Russian).

element of the suspension mineral component is insoluble manganese oxide (MnO_2), which is formed due to Mn(II) oxidation [17, 30].

When suspended particles, which, as a rule, do not have electrical conductivity, enter the CTD probe measuring cell, electrical conductivity values are underestimated due to the displacement of some of the seawater ions, which are electrical charge carriers. An error in determining electrical conductivity leads to errors in calculating density and salinity. This is the second cause for different values when determining hydrophysical parameters in two ways. To determine the degree of suspended matter and variations in ion-salt composition effect on the accuracy of density measurements with a CTD probe, it is advisable to study the Black Sea suboxic layer waters using *AutoSal* precision laboratory salinity meter.

The deviation of density value measured by the density meter from the one calculated using electrical conductivity is the density determination error ($\Delta\sigma_t$), and the deviation of practical salinity value from the sum of the major ions is the salinity determination error (ΔS). The relationship of $\Delta\sigma_t$ and ΔS with density (depth) in the water column within the range of σ_t values of 15.9–16.2 is shown in Fig. 2. In 2021, $\Delta\sigma_t$ value ranged from 0.05 to 0.19 kg/m^3 and ΔS ranged from 0.32 to 0.47.

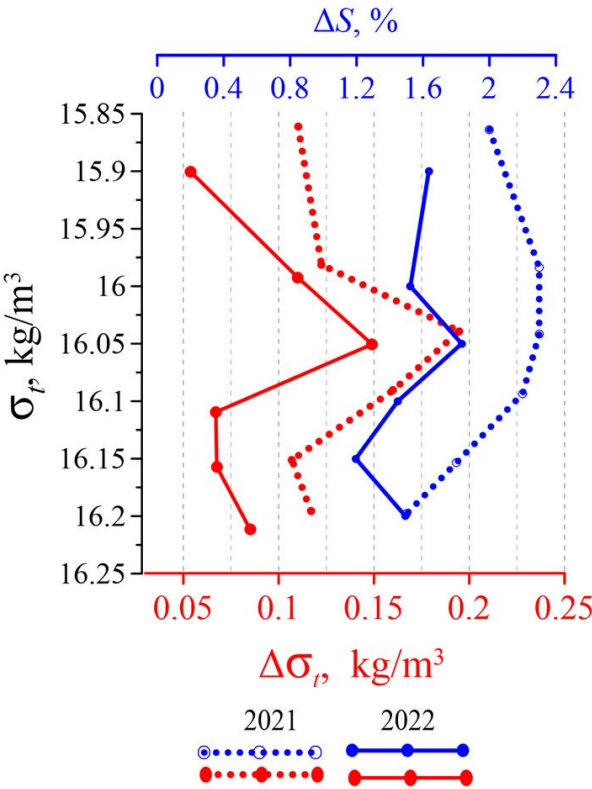


Fig. 2. Relationship between $\Delta\sigma_t$ and ΔS , and density based on the results of laboratory studies and calculations using the CTD probe data in 2021 and 2022

Fig. 2 particularly contrasts the layer with maximum $\Delta\sigma_t$ and ΔS deviations in 2021 at $\sigma_t = 16.04 \text{ kg/m}^3$ (at 151.3 m depth) and in 2022 at $\sigma_t = 16.05 \text{ kg/m}^3$ (at 152.6 m depth), i.e., under almost identical conditions. This layer corresponds to the turbidity peak shown in Fig. 1. This Black Sea layer represents the upper boundary of hydrogen sulfide zone and the lower boundary of suboxic zone [12, 14]. Figure 2 is a detailed version of Fig. 1 and allows us to see that the pycnocline has pronounced density and salinity gradients and its core is located at $\sigma_t \sim 16.05 \text{ kg/m}^3$. However, its depth can vary since the main Black Sea pycnocline is characterized by short-period fluctuations [9].

The third cause for errors in calculating salinity using EOS-80 and, to a lesser extent, TEOS-10 is due to hydrochemical anomalies in the Black Sea waters relative to the SSW. Fig. 3 presents these anomalies as relative content deviations of major ions (ΔC) in the Black Sea water samples under study from their content in the SSW and the relationship between ΔC and density. The content of ions in the SSW composition on the graph corresponds to zero. Negative values on x-axis mean that ion content is less than in SSW, and positive values – that more. The figure reveals that ΔC distribution over depth is uneven. The relative content of Cl^- and SO_4^{2-} experiences noticeable fluctuations at the suboxic layer lower boundary where the hydrogen sulfide zone begins and sulfate reduction and other biogeochemical processes causing metamorphization of waters intensify. From Fig. 3 it can be seen that the highest ΔC value corresponds to the content of chlorides and bicarbonates, sodium and calcium ions and indicates the degree of difference between the Black Sea waters and the oceanic ones. In general, the content of chlorides in the studied samples was lower by, on average, 0.4% than in SSW, and sulfate content was close to the ones in SSW (deviations amounted to an average of 0.14% – within the determination error). HCO_3^- relative content in the studied samples was consistently higher than in SSW, by $\sim 0.6\%$, and Na^+ content was lower than in SSW, by $\sim 0.4\%$ in 2021 and by $\sim 0.2\%$ in 2022.

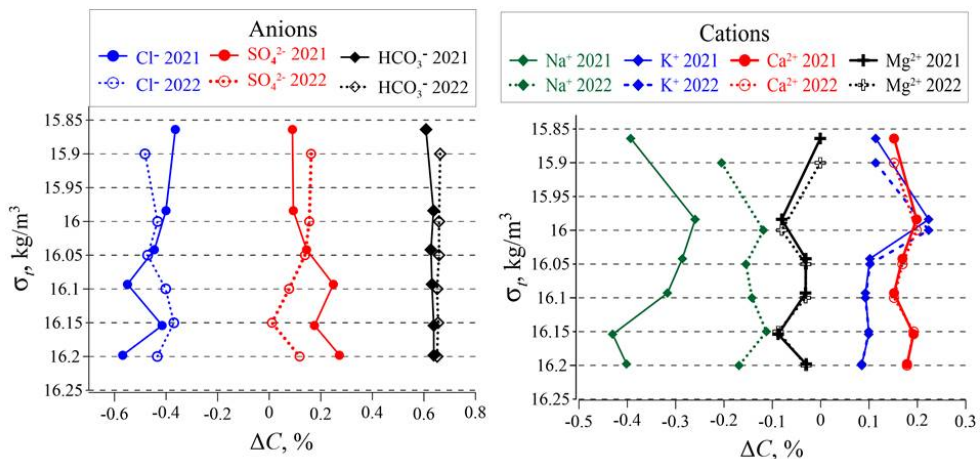


Fig. 3. Deviation (ΔC) of the relative content of major ions in the Black Sea water from their content in SSW, and their distribution by density (depth) in the suboxic layer of the Black Sea

Relative content of Mg^{2+} ions in the Black Sea water was very close to their content in the SSW; K^+ and Ca^{2+} were higher than in the SSW by $\sim 0.2\%$. The profiles of relative content of ions, and especially cations, demonstrate good correlation between 2021 and 2022.

Sulfate-chlorine ratio, being an important characteristic of a basin, reflects the constancy or variability of its ionic composition. The $\text{SO}_4^{2-}/\text{Cl}^-$ distribution in the Black Sea suboxic layer using the studied samples as an example is shown in Fig. 4.

Figure 4 indicates that $\text{SO}_4^{2-}/\text{Cl}^-$ distribution is not uniform in the studied σ_t range. The sulfate-chlorine ratio, which monotonically decreases to 1200 m depth [15], changes its values abruptly by 1–2% in the suboxic layer. The correlation of these changes in both 2021 and 2022 indicates a pattern of this phenomenon. In [15], a linearity violation of SO_4^{2-} concentration distribution with reference to chlorinity in the upper part of the anaerobic zone – in the area of hydrogen sulfide occurrence and to ~ 200 m depth, is also noted. The area of sulfate deficiency in relation to chlorinity coincides with the layer of increasing bacterioplankton mass, where the processes of CO_2 fixation and sulfate reduction are accelerated. The loss of sulfates in this layer, where a local maximum of suspended organic matter is frequently present, is a consequence of their reduction during sulfate reduction process.

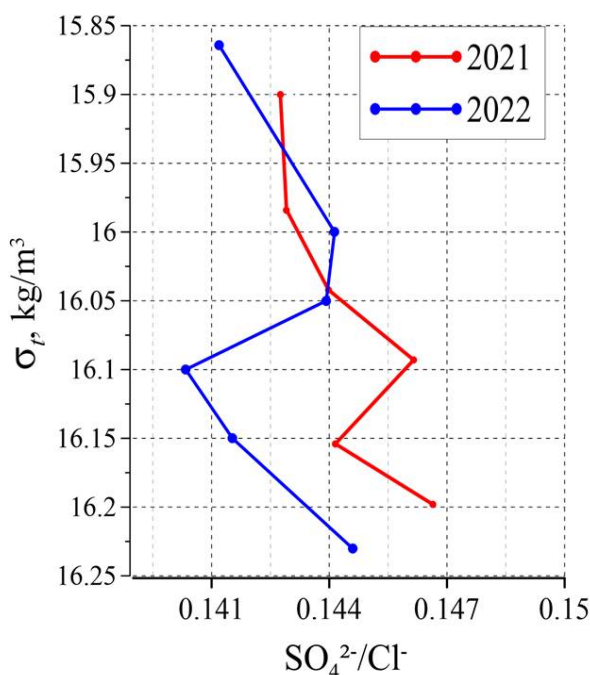


Fig. 4. Distribution of $\text{SO}_4^{2-}/\text{Cl}^-$ by density (depth) in 2021 and 2022

Variations in the seawater ionic composition are factors that cause errors in calculations of density and salinity from electrical conductivity in the sea and in their laboratory determinations. MIC hydrochemical anomalies mainly affect electrical conductivity and the accuracy of its determination, and, accordingly, all subsequent

calculations related to it. Early studies show that electrical conductivity of solutions, including sea water, depends on the nature of the ions (unequal electrical conductivity of different ions), their concentration and variations, as well as viscosity and temperature of the water ^{4, 5} [28–31]. Increased concentrations of some ions, especially sulfates, calcium and magnesium (which enter the sea during the decay of organic residues, as a result of ion exchange reactions occurring at geochemical barriers when terrigenous suspended matter enters with continental runoff, as well as other processes [7, 20]) contribute to underestimation of salinity and density values calculated from electrical conductivity [3, 22, 27]. Hydrochemical anomalies of the Black Sea water ionic composition are the cause of deviations in the density and salinity values obtained from the CTD probe data on electrical conductivity from the values obtained in the laboratory. These deviations are especially noticeable in the surface [21, 31] and suboxic layers of the Black Sea.

Conclusions

Based on field measurements carried out with CTD probe and turbidity meter in the Black Sea, laboratory determinations of density, salinity and MIC, as well as comparison of the results obtained, it was found that CTD sounding underestimates density and salinity values in the suboxic layer. Density underestimation was 0.11–0.19 kg/m³ in 2021, 0.05–0.15 kg/m³ in 2022, and salinity underestimation was up to 2%. Density gradient obtained from the density meter data was approximately twice as large as that calculated from the CTD probe data using the EOS-80 equation.

The first cause for errors while determining density by EOS-80 using *SP* is due to practical salinity calculation, which takes into account not the carbonate content, but only the products of their decomposition – metal oxides. This results in *SP* being approximately 0.47% lower than absolute salinity.

The study and comparison of the MIC of the Black Sea suboxic layer and the SSW resulted in determination of the Black Sea water hydrochemical anomalies. Their assessment revealed that SO₄²⁻ and HCO₃⁻ contents in the Black Sea samples are on average 0.2 and 0.6% higher, respectively, K⁺ and Ca²⁺ are 0.2% higher, Cl⁻ and Na⁺ contents are on average 0.4 and 0.3% lower, respectively, than in SSW, and Mg²⁺ content is close to the one in SSW.

It was found that nonlinear distribution of major ions (ionic variations) in the chemical composition of suboxic layer waters is most strongly expressed in an abrupt SO₄²⁻/Cl⁻ variation by 1–2%. Ionic variations, and especially SO₄²⁻/Cl⁻ change, are the second cause of errors in determining salinity and density from electrical conductivity, i.e., from CTD probe data.

As a result of determining density values of the samples under study obtained in two ways and comparing them with the turbidity profile, it was found that

⁴ Mushkambarov, N.N., 2008. *Physical and Colloidal Chemistry. Textbook for Universities (With Problems and Solutions)*. 3rd Ed., Expanded. Moscow: Medical Information Agency LLC, 295 p. (in Russian).

⁵ Svarovskaya, N.A., Kolesnikov, I.M. and Vinokurov, V.A., 2017. *Electrochemistry of Electrolyte Solutions. Part I. Electrical Conductivity: Study Guide*. Moscow: Publishing Centre of I.M. Gubkin Russian State University of Oil and Gas (NRU), 66 p. (in Russian).

the layer of increased suspended matter concentration (turbidity peak) was in the range of maximum $\Delta\sigma_t$ values in ~ 160 m layer at σ_t equal to 16.04–16.05 kg/m³). It follows from this that the increased concentration of suspended matter underestimates the electrical conductivity values, and, consequently, the values of salinity and density calculated using it; this is the third cause of errors in determining density and salinity from CTD probe data.

REFERENCES

1. Culkin, F. and Smed, J., 1979. The History of Standard Seawater. *Oceanologica Acta*, 2(3), pp. 355-364.
2. Pawlowicz, R., 2013. Key Physical Variables in the Ocean: Temperature, Salinity, and Density. *Nature Education Knowledge*, 4(4), 13.
3. Uchida, H., Kawano, T., Nakano, T., Wakita, M., Tanaka, T. and Tanihara, S., 2020. An Expanded Batch-to-Batch Correction for IAPSO Standard Seawater. *Journal of Atmospheric and Oceanic Technology*, 37(8), pp. 1507-1520. <https://doi.org/10.1175/JTECH-D-19-0184.1>
4. Pawlowicz, R., Wright, D.G. and Millero, F.J., 2011. The Effects of Biogeochemical Processes on Oceanic Conductivity/Salinity/Density Relationships and the Characterization of Real Seawater. *Ocean Science*, 7(3), pp. 363-387. <https://doi.org/10.5194/os-7-363-2011>
5. Brewer, P.G. and Bradshaw, A., 1975. The Effect of the Non-Ideal Composition of Sea Water on Salinity and Density. *Journal of Marine Research*, 33(2), pp. 157-175.
6. Millero, F.J., 2013. *Chemical Oceanography*. 4th Edition. Boca Raton: CRC Press, 591 p. <https://doi.org/10.1201/b14753>
7. Savenko, A.V., Savenko, V.S. and Pokrovskii, O.S., 2021. Sorption-Desorption Transformation of the Runoff of Dissolved Microelements at River-Sea Geochemical Barrier (Based on Data of Experimental Laboratory Simulation). *Water Resources*, 48(2), pp. 285-290. <https://doi.org/10.1134/S0097807821020159>
8. Ivanov, V.A. and Belokopytov, V.N., 2013. *Oceanography of Black Sea*. Sevastopol: ECOSI-Gidrofizika, 210 p.
9. Hiscock, W.T. and Millero, F.J., 2006. Alkalinity of the Anoxic Waters in the Western Black Sea. *Deep Sea Research Part II: Topical Studies in Oceanography*, 53(17-19), pp. 1787-1801. <https://doi.org/10.1016/j.dsr2.2006.05.020>
10. Vinogradov, M.E. and Nalbandov, Y.R., 1990. Influence of Water Density Variations on the Distribution of the Physical, Chemical and Biological Characteristics of the Open Regions of the Black Sea. *Oceanology*, 30(5), pp. 769-777 (in Russian).
11. Zatsepin, A.G., Ostrovskii, A.G., Kremenetskii, V.V., Piotukh, V.B., Kuklev, S.B., Moskalenko, L.V., Podymov, O.I., Baranov, V.I., Korzh, A.O. [et al.], 2013. On the Nature of Short-Period Oscillations of the Main Black Sea Pycnocline, Submesoscale Eddies, and Response of the Marine Environment to the Catastrophic Shower of 2012. *Izvestiya, Atmospheric and Oceanic Physics*, 49(6), pp. 659-673. <https://doi.org/10.1134/S0001433813060145>
12. Kononov, S.K., Vidnichuk, A.V. and Orekhova, N.A., 2018. Spatio-Temporal Characteristics of the Hydrochemical Structure of Water in the Deep-Sea Part of the Black Sea. In: A. P. Lisitzin, ed., 2018. *The Black Sea System*. Moscow: Scientific World, pp. 106-119. <https://doi.org/10.29006/978-5-91522-473-4.2018.106> (in Russian).
13. Murray, J.W., Jannasch, H.W., Honjo, S., Anderson, R.F., Reeburgh, W.S., Top, Z., Friederich, G.E., Codispoti, L.A. and Izdar, E., 1989. Unexpected Changes in the Oxidic/Anoxic Interface in the Black Sea. *Nature*, 338(6214), pp. 411-413. <https://doi.org/10.1038/338411a0>
14. Kirkpatrick, J.B., Fuchsman, C.A., Yakushev, E.V., Staley, J.T. and Murray, J.W., 2012. Concurrent Activity of Anammox and Denitrifying Bacteria in the Black Sea. *Frontiers in Microbiology*, 3, 256. <https://doi.org/10.3389/fmicb.2012.00256>

15. Dubinin, A.V., Dubinina, E.O., Kossova, S.A. and Berezhnaya, E.D., 2017. Ventilation of the Black Sea Anoxic Zone: Evidence from the Sulfur Isotope Composition of Sulfate. *Doklady Earth Sciences*, 475(2), pp. 877-882. <https://doi.org/10.1134/S1028334X17080037>
16. Volkov, I.I., Kontar, E.A., Lukashev, Yu.F., Neretin, L.N., Nyffeler, F. and Rozanov, A.G., 1997. Upper Boundary of Hydrogen Sulfide: Implications for the Nepheloid Redox Layer in Waters of the Caucasian Slope of the Black Sea. *Geochemistry International*, 35, pp. 540-550.
17. Yilmaz, A., Coban-Yildiz, Y., Telli-Karakos, F. and Bologa, A., 2006. Surface and Mid-Water Sources of Organic Carbon by Photoautotrophic and Chemoautotrophic Production in the Black Sea. *Deep Sea Research Part II: Topical Studies in Oceanography*, 53(17-19), pp. 1988-2004. <https://doi.org/10.1016/j.dsr2.2006.03.015>
18. Kremling, K., 1974. Relation between Chlorinity and Conductometric Salinity in Black Sea Water. In: E. T. Degens and D. A. Ross, 1974. *The Black Sea – Geology, Chemistry, and Biology*. Tulsa, USA: American Association of Petroleum Geologists, pp. 151-154. <https://doi.org/10.1306/M20377C44>
19. Gershonovich, D.E., Ryabinin, A.I. and Simonov, A.I., eds., 1992. *Hydrometeorology and Hydrochemistry of Seas in the USSR. Vol. 4. The Black Sea. Issue 2. Hydrochemical Conditions and Oceanological Basis for the Formation of Biological Productivity*. Saint Petersburg: Gidrometeoizdat, 220 p. (in Russian).
20. Pawlowicz, R., 2010. A Model for Predicting Changes in the Electrical Conductivity, Practical Salinity, and Absolute Salinity of Seawater due to Variations in Relative Chemical Composition. *Ocean Science*, 6(1), pp. 361-378. <https://doi.org/10.5194/os-6-361-2010>
21. Andrulionis, N.Yu. and Zavyalov, P.O., 2019. Laboratory Studies of the Main Component Composition of Hyperhaline Lakes. *Physical Oceanography*, 26(1), pp. 13-31. <https://doi.org/10.22449/1573-160X-2019-1-13-31>
22. Millero, F.J., 2010. History of the Equation of State of Seawater. *Oceanography*, 23(3), pp. 18-33. <https://doi.org/10.5670/oceanog.2010.21>
23. Millero, F.J. and Huang, F., 2009. The Density of Seawater as a Function of Salinity (5 to 70 g kg⁻¹) and Temperature (273.15 to 363.15 K). *Ocean Science*, 5(2), pp. 91-100. <https://doi.org/10.5194/os-5-91-2009>
24. Kayukawa, Y. and Uchida, H., 2021. Absolute Density Measurements for Standard Sea-Water by Hydrostatic Weighing of Silicon Sinkers. *Measurement: Sensors*, 18, 100200. <https://doi.org/10.1016/j.measen.2021.100200>
25. Khoruzhii, D.S., Ovsyanyi, E.I. and Konovalov, S.K., 2011. Comparison of the Results of Determination of the Carbonate System and the Total Alkalinity of Seawater According to the Data Obtained by Using Different Analytic Methods. *Physical Oceanography*, 21(3), pp. 182-194. <https://doi.org/10.1007/s11110-011-9114-6>
26. Kremling, K., 1999. Determination of the Major Constituents. In: K. Grasshoff, K. Kremling and M. Ehrhardt, eds., 1999. *Methods of Seawater Analysis*. Weinheim: WILEY-VCH. Chapter 11, pp. 229-251. <https://doi.org/10.1002/9783527613984.ch11>
27. Millero, F.J., Feistel, R., Wright, D.G. and McDougall, T.J., 2008. The Composition of Standard Seawater and the Definition of the Reference-Composition Salinity Scale. *Deep Sea Research Part I: Oceanographic Research Papers*, 55(1), pp. 50-72. <https://doi.org/10.1016/j.dsr.2007.10.001>
28. McDougall, T.J., Jackett, D.R., Millero, F.J., Pawlowicz, R. and Barker, P.M., 2012. An Algorithm for Estimating Absolute Salinity in the Global Ocean. *Ocean Science*, 8(6), pp. 1123-1134. <https://doi.org/10.5194/os-8-1123-2012>
29. Sauerheber, R. and Heinz, B., 2015. Temperature Effects on Conductivity of Seawater and Physiologic Saline, Mechanism and Significance. *Chemical Sciences Journal*, 6(4), 1000109. <https://doi.org/10.4172/2150-3494.1000109>

30. Stunzhas, P.A. and Yakushev, E.V., 2006. Fine Hydrochemical Structure of the Redox Zone in the Black Sea According to the Results of Measurements with an Open Oxygen Sensor and with Bottle Samplers. *Oceanology*, 46(5), pp. 629-641. <https://doi.org/10.1134/S0001437006050031>
31. Andrulionis, N.Yu., Zavialov, I.B. and Rozhdestvenskiy, S.A., 2024. Major Ion Composition of Waters in the Kerch Strait and the Adjacent Areas. *Physical Oceanography*, 31(1), pp. 79-98.

About the authors:

Natalia Yu. Andrulionis, Research Associate, Laboratory of Land-Ocean Interaction and Anthropogenic Impact, P.P. Shirshov Institute of Oceanology of RAS (36 Nakhimoskiy Ave., Moscow, 117997, Russian Federation); CSc (Geogr.), **ORCID ID: 0000-0001-9141-1945**, **Web of Science Researcher ID: AGP-4038-2022**, **Scopus Author ID: 57209575290**, natalya@ocean.ru

Oleg I. Podymov, Senior Research Associate, Laboratory of Hydrophysics and Modelling, Southern Branch of P.P. Shirshov Institute of Oceanology of RAS (1G Prostornaya Str., Gelendzhik, 353467, Russian Federation), CSc (Phys.-Math.), **ORCID ID: 0000-0002-6591-9160**, **Web of Science Researcher ID: C-7182-2014**, **Scopus Author ID: 10639563400**, huravela@yahoo.com

Contribution of the co-authors:

Natalia Yu. Andrulionis – setting the goal and objectives of the research work; selection of methods for studying ionic-salt composition of waters; performing laboratory studies of ionic-salt composition, salinity and density of samples; obtained data analysis; preparation of graphic material and the article text

Oleg I. Podymov – field hydrophysical measurements and water sampling; provision of necessary data; participation in the discussion of the obtained results

The authors have read and approved the final manuscript.


The authors declare that they have no conflict of interest.

Original article

Trends in the Interannual Variability of Salinity Field in the Upper 1000-Meter Layer of the Northeastern Pacific Ocean under Conditions of Modern Global Warming

I. D. Rostov , E. V. Dmitrieva

*V. I. Il'ichev Pacific Oceanological Institute, Far Eastern Branch of RAS, Vladivostok,
Russian Federation*

 rostov@poi.dvo.ru

Abstract

Purpose. The study is purposed at determining the trends and the regional features of interannual changes in salinity and salt content in the upper 1000-m layer of the extratropical zone in the northeastern Pacific Ocean, and at analyzing their possible cause-and-effect relations with large-scale and regional processes in the ocean and the atmosphere over the last two decades of the current period of global warming.

Methods and Results. The NOAA climate data sets including the GODAS oceanographic data assimilation system in the nodes of a regular grid, as well as the data on the amount of atmospheric precipitation and the series of climate indices were used in the study. The monthly average ERA5 reanalysis data on precipitation and evaporation from the underlying surface were also applied. The methods of cluster, correlation and regression analysis, as well as the apparatus of empirical orthogonal functions were involved. The conducted research resulted in identifying the regional spatial and temporal features of the changes in salinity and salt content in the upper 1000-m water column of the study area under conditions of the current warming phase accompanied by the intensification of global and local hydrological cycles. The quantitative characteristics of the noted trends and their statistical significance were assessed.

Conclusions. The spatial distribution of evaporation-precipitation ($E-P$) difference trends demonstrates a predominant evaporation pattern over most of the water area that differs from the global trends in a hydrological cycle in the middle and high latitudes of the Northern Hemisphere, especially over the previous period. In general, a statistically significant positive trend in salt content was observed in the upper 1000 m of the water column in the northern area, whereas in other regions and on the average over the whole water area, small statistically insignificant negative trends were noted in the above-mentioned layer. The correlation relations between the changes in average annual salinity and salt content values, on the one hand, and different large-scale regional processes and climate variables, on the other hand, are most manifested through the following parameters: climate indices $NPGO$, IPO , PDO and AD , the first mode of EOF of fluctuations in the $PC1$ values of evaporation-precipitation ($E-P$) difference, and the second mode of EOF of anomaly of the isobaric surface AT_{500} geopotential.

Keywords: northeastern part of the Pacific Ocean, extratropical zone, climate changes, hydrological cycle, salinity, salt content, trends, regional features, climate indices, correlations

Acknowledgments: The study was carried out within the framework of the theme of state assignment of POI FEB of RAS No. 121021700346-7 “Study of the main processes which determine state and variability of oceanological characteristics of the marginal seas of Asia and the adjacent regions of the Pacific and Indian oceans”. The authors are grateful to the developers for the opportunity to use the climatic data posted on the NOAA websites.

For citation: Rostov, I.D. and Dmitrieva, E.V., 2024. Trends in the Interannual Variability of Salinity Field in the Upper 1000-Meter Layer of the Northeastern Pacific Ocean under Conditions of Modern Global Warming. *Physical Oceanography*, 31(3), pp. 350-363.

© 2024, I. D. Rostov, E. V. Dmitrieva

© 2024, Physical Oceanography



Introduction

Modern climate changes in various geospheres are accompanied by an intensification of the global water cycle (hydrological cycle) and significant changes in the ocean surface salinity and the salt content of its water column on the scales from regional to global [1–5]. A salinity field (S) reflects a large-scale long-term balance between various components of the surface freshwater flow, processes of horizontal advection and mixing in the ocean [5–7]. Over the open ocean away from coastal areas and high latitudes, where the influence of river flow and ice melt is limited, evaporation minus precipitation is the main factor affecting freshwater flow, which, together with dynamic processes in the ocean, leads to the ocean salinity variability [8]. The corresponding response to changes in the hydrological cycle is characterized by a significant spatiotemporal heterogeneity and can be observed in the form of areas of anomalies and trends in salinity and salt content of different values and signs both on the surface and in the water column of oceans and seas [9, 10]. Moreover, due to their small volume in relation to the surface area, the water areas of marginal seas react to changing freshwater balance characteristics more strongly than in the open ocean [7, 11]. In contrast to thermal characteristics, formation of salinity field features in different World Ocean areas has a more complex, comprehensive and ambiguous nature [7, 9, 11–15].

In the course of studies of modern changes in the thermal conditions of the North Pacific Ocean, caused by a shift in the climate regime and global warming, large-scale spatiotemporal inhomogeneities in the interannual variability of thermal characteristics of water and air were identified and estimates of their quantitative values and statistical significance at the turn of the 20th–21st centuries were given [16]. Since about 2013, following the end of the “global warming pause” [17], marine heatwaves – localized areas of extremely high ocean surface temperatures (SSTs) associated with the atmospheric conditions resulting from disruption of the Earth’s energy balance [17, 18], have become common in the northeastern Pacific Ocean. In 2014–2016 and 2019–2020, these areas of SST anomalies up to 2.5–3 °C spread along the west coast of North America and much of the northeastern Pacific Ocean forming three-dimensional thermal structures that cover the upper ocean layer several hundred meters thick and persist for a long time [19]. During the past 20-year period at the beginning of the 21st century, the northeastern extratropical Pacific region generally experienced higher rates of warming (SST) compared to the previous period, while the adjacent northwestern region experienced the opposite trend [16]. Recent studies [20] enabled to identify and characterize regional spatiotemporal features of accelerated changes in salinity and water column salinity of the upper 1000 m of the northwestern Pacific Ocean in the first decades of the 21st century, accompanied by the intensification of global and local hydrological cycles. It was shown that statistically significant negative trends in the evaporation-precipitation difference were observed throughout the entire area, corresponding to the increasing trends in the humidification regime at the ocean surface. During this period, there were also significant changes in various indicators of atmospheric and ocean circulation accompanied by increased water exchange in the extratropical zone of the ocean with adjacent regions. It led to the formation of vast volumes of water columns subject to both desalination and salinization, as well as subsequent transformation. In general, in the water area of

the extratropical zone of the northwestern Pacific Ocean, there was a tendency for a gradual decrease in average salinity values at the surface and desalination of waters in the upper 1000-meter layer [5, 10].

It is of interest to consider the regional features of the interannual variability of the spatial structure of the water column salinity field and salt content of the upper 1000-meter layer of the northeastern Pacific Ocean and to compare the results obtained with the corresponding characteristics for adjacent regions. It will enable to clarify more general similar estimates previously made for the World Ocean in general [5, 9, 10].

The present paper is aimed at trends and regional features of interannual changes in salinity and salt content in the upper 1000-m layer of the extratropical zone in the northeastern Pacific Ocean and at analyzing their possible cause-and-effect relations with large-scale and regional processes in the ocean and atmosphere at the beginning of the 21st century.

Data and methods

As in the previous work [20], the data on salinity and current speed of the GODAS oceanographic observation assimilation system at $0.3^\circ \times 1^\circ$ grid points from <https://www.esrl.noaa.gov/psd/data/gridded/data.godas.html> for 2000–2022 were used. The monthly average precipitation (P) data from the ERA5 reanalysis on a $0.25^\circ \times 0.25^\circ$ grid from http://apdrc.soest.hawaii.edu/erddap/griddap/hawaii_soest_d124_2bb9_c935.html and evaporation (E) from the underlying surface WHOI OAFflux version3 on a $1^\circ \times 1^\circ$ grid (http://apdrc.soest.hawaii.edu/erddap/griddap/hawaii_soest_6b5a_df06_3eeb.html?page=1) was also used. With the help of these data, the $E-P$ difference at the nodes of a one-degree grid was calculated.

The reanalysis data of pressure fields and series of climate (circulation) indices (CI) [16]: NP , $NPGO$, PDO , SOI , PTW , IPO , WP , $NINO.WEST$ and $WPWP$ for the same years were also taken. The data listed were obtained from the NOAA websites <https://psl.noaa.gov/data/gridded/index.html> and <https://psl.noaa.gov/data/climateindices/list/>. Additionally, the Asian Depression (AD) index was calculated using the surface atmospheric pressure.

Statistics were calculated and anomaly fields of various characteristics were decomposed into principal EOF components (PC) using a unified method [16, 20]. Also, using GODAS data on salinity at 31 levels (upper level of 5 m), the values of salt content (Qs) and their anomalies (ΔQs) were calculated in various layers from the surface to 1000 m depth according to the equation given in [21, p. 3520].

Based on the data averaged over the entire period of interannual changes in salinity at various levels of the upper 500-meter layer in each grid node using the cluster analysis method for the three principal EOF $S(z)$ components, four separate areas, located in different parts of the sea: northern (N), western (W), eastern (E) and southern (S) were identified (Fig. 1, e). Using the cluster analysis method to zonate the studied water area based on interannual fluctuations in salt content ΔQs in the 5–200 m layer (as was done previously for the adjacent area [20]), the results turned out to be uninformative due to excessive fragmentation of the research area.

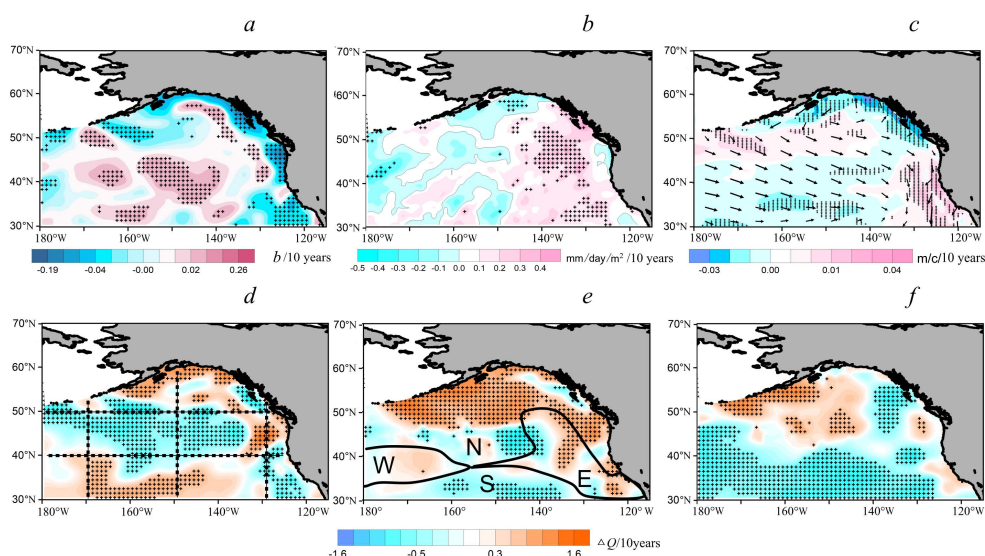


Fig. 1. Trends in average annual salinity at the 5 m level (*a*), trends in annual average values of evaporation-precipitation differences (*b*), currents (arrows) and current velocity trends (highlighted in color) at the 5 m level based on the GODAS data (*c*), trends in the normalized salt content values in the 5–200 m (*d*), 200–460 m (*e*), and 460–950 m (*f*) layers in 2000–2022. Fig. 1, *d* shows the location of sections, and Fig. 1, *e* – the location of selected regions (W, N, E and S). Here and in other figures, crosses indicate the areas where the estimates are statistically (95%) significant

Subsequently, by simple grid data averaging within the water areas of these areas, the long-term variation of salinity at each of 31 levels and salt content in individual layers was calculated: upper (5–200 m), intermediate (200–460 m) and deep (460–950 m).

Interannual spatiotemporal variability features of salinity field characteristics

In the studied water area, northern (N) and eastern (E) areas are distinguished with characteristic features inherent in the subarctic structure of waters, as well as western (W) and southern (S) ones – with features characteristic of the area of mixing waters of subarctic and subtropical structures (Fig. 1, *e*)¹ [22]. Within the entire water area, the components of the flows of the Subarctic and North Pacific currents, the Californian and Alaskan current systems can be observed [22, 23], in the interannual changes of which there are statistically significant trends in the current velocity module of different signs (Fig. 1, *c*).

During the considered period, statistically significant trends of both signs with maximum values of $-0.19 \dots 0.06/10$ years were expressed in the interannual variation of the average annual salinity at the surface level of 5 m. The areas with maximum negative salinity trends are located on the studied area periphery – in the areas adjacent to the North American continent and the Aleutian Islands. These

¹ Dobrovolsky, A.D., ed., 1968. *Pacific Ocean. Volume II. The Pacific Ocean Hydrology*. Moscow: Nauka, 524 p. (in Russian).

areas of coastal waters are affected by changes in continental runoff and water exchange with the Bering Sea. On average for the studied region, there was a tendency for a slight salinity increase at this level, in contrast to the area of the northwestern Pacific Ocean, where significant negative salinity trends were observed [20]. All areas with positive and negative salinity trends (Fig. 1, *a*) are expressed in the water area both in the warm and cold periods of the year.

At the 200 m level of the lower boundary of the upper layer, statistically significant trends in the average annual salinity of both signs were expressed with maximum values of $-0.03 \dots 0.14/10$ years at the 500 m depth – up to $-0.03 \dots 0.05/10$ years. At the same time, in the lower part of the deep layer, only small statistically significant negative salinity gradients up to $-0.02/10$ years were observed at the levels located deeper than 900 m throughout the entire water area of the northeastern Pacific Ocean.

In general, for the study area, statistically significant trends in interannual fluctuations in the average annual amount of precipitation and evaporation – indicators of the humidification regime of the underlying surface – are not expressed. Averaged over the entire water area, the maximum positive trend in both precipitation and evaporation (~ 0.04 mm/day/m² for 10 years) was expressed in the warm period of the year. These results are consistent with similar precipitation estimates obtained from <https://psl.noaa.gov/data/gridded/data.cmap.html> on a $2.5^\circ \times 2.5^\circ$ grid. The spatial distribution of trends in the evaporation-precipitation difference (*E-P*) demonstrates the predominant influence of evaporation over most of the water area, which is statistically significant in its eastern part (Fig. 1, *b*). It does not agree with the distribution of salinity trends at the ocean surface and salinity content in different layers (Fig. 1, *a, d–f*) and does not correspond to the general global trends of the hydrological cycle in the middle and high latitudes of the Northern Hemisphere [5, 7, 9], especially for the previous period of 1950–2000². As noted earlier [5, 20], in contrast to long-term changes in the characteristics of the ocean surface salinity and humidification on a global scale [10], in the middle and high latitudes, trends in spatial changes in the *E-P* difference may not be consistent with the corresponding regional trends in changes in salinity, since ocean dynamics and local factors can also play a controlling role in salinity changes on the surface and in the ocean water column ensuring a regional balance of the salinity field [9].

The patterns of spatial features of interannual changes in salt content (*Qs*) trends in the upper, intermediate and deep layers differ significantly (Fig. 1, *d–f*), as was noted for the adjacent area of the northwestern part of the extratropical zone [20]. At the same time, the patterns of spatial distribution of salt content trends in the upper and intermediate layers in the warm and cold periods of the year do not show noticeable differences.

² Stocker, T.F., Qin, D., Plattner, G.-K., Tignor, M., Allen, S.K., Boschung, J., Nauels, A., Xia, Y., Bex, V. and Midgley, P.M., eds., 2014. *Climate Change 2013 – The Physical Science Basis: Working Group I Contribution to the Fifth Assessment Report of the Intergovernmental Panel on Climate Change*. Cambridge, United Kingdom: Cambridge University Press, 1535 p. doi:10.1017/CBO9781107415324

Note that the structures of the patterns of spatial distribution of salt content in the deep layer are in good agreement with each other in both northeastern and northwestern areas [20], where a clear zonal orientation of the boundary ($\sim 40\text{--}45^\circ\text{N}$) of large-scale areas with the opposite sign of salt content trends is observed. The noted trends in the salinity and salt content decrease in the deep layer under the conditions of intensification of the global hydrological cycle are consistent with the results of other researchers [7, 9, 10]. At the same time, vast areas can be traced within each of the layers, where over the past two decades either desalination or salinization of the water column has occurred at different velocities. On average, a velocity of $-1.4 \dots 0.8 \text{ kg/m}^2/10 \text{ years}$ can be observed over the water area (Fig. 1, *d–f*, Table 1).

Table 1

Estimates of the linear trend of salt content (Q_s , $\text{kg/m}^2/10 \text{ years}$) of various layers of the water column in the identified areas and the entire water area in 2000–2022

Regions	Layer boundaries, m			
	5-200	200-460	460-950	5-950
N	-0.33	1.85	0.28	0.60
W	0.74	0.66	-2.40	-0.33
E	-0.38	0.55	-0.80	-0.21
S	3.12	-1.04	-2.83	-0.25
Average over the entire water area	0.79	0.51	-1.44	-0.05

Note. Here and in Table 2, statistically significant (95%) estimates are highlighted in bold.

Generalization for the water areas of individual regions: the greatest significant positive trends in salinity are observed in the upper layer of the southern region ($3.12 \text{ kg/m}^2/10 \text{ years}$) and in the intermediate layer of the northern region ($1.85 \text{ kg/m}^2/10 \text{ years}$); the greatest significant negative trends ($-2.83 \text{ kg/m}^2/10 \text{ years}$) are in the deep layer of the southern region. In general, for the region, a statistically significant positive trend in salt content was observed in the upper ~ 1000 -meter water column of the northern region, while in other areas and on average for the water area, small statistically insignificant negative trends were observed in this layer (Table 1). These estimates of tendencies, trends and regional features of interannual changes in the salinity field structure enable to detail previously obtained estimates of changes occurring on a global scale under the conditions of the hydrological cycle intensification [1, 7, 9, 10].

As in the adjacent region of the northwestern Pacific Ocean [20], the main features of the spatial structure of trends in the salinity content of the upper layer (Fig. 1, *d*) are in good agreement with the distribution scheme of the coefficients of the first mode *EOF1* of this layer Q_s anomaly decomposition, which makes it possible to use the principal component (*PC1*) of this method of parameterizing Q_s fluctuations to establish correlations with various climate parameters.

Interannual variability of the vertical structure of salinity in the upper 1000-m layer

Formation and variability of the vertical structure of a salinity field takes place as a result of a continuous interaction of various processes on the surface, vertical

mixing and intra-water exchange. Fig. 2 shows average profiles of the vertical distribution of salinity $S(z)$, amplitude structure of $S(z)$ anomaly fluctuations – the principal EOF component $PC1$ and salinity trends $b(z)$ at various levels within the selected areas according to the data of interannual variability $S(z)$ for 2000–2022.

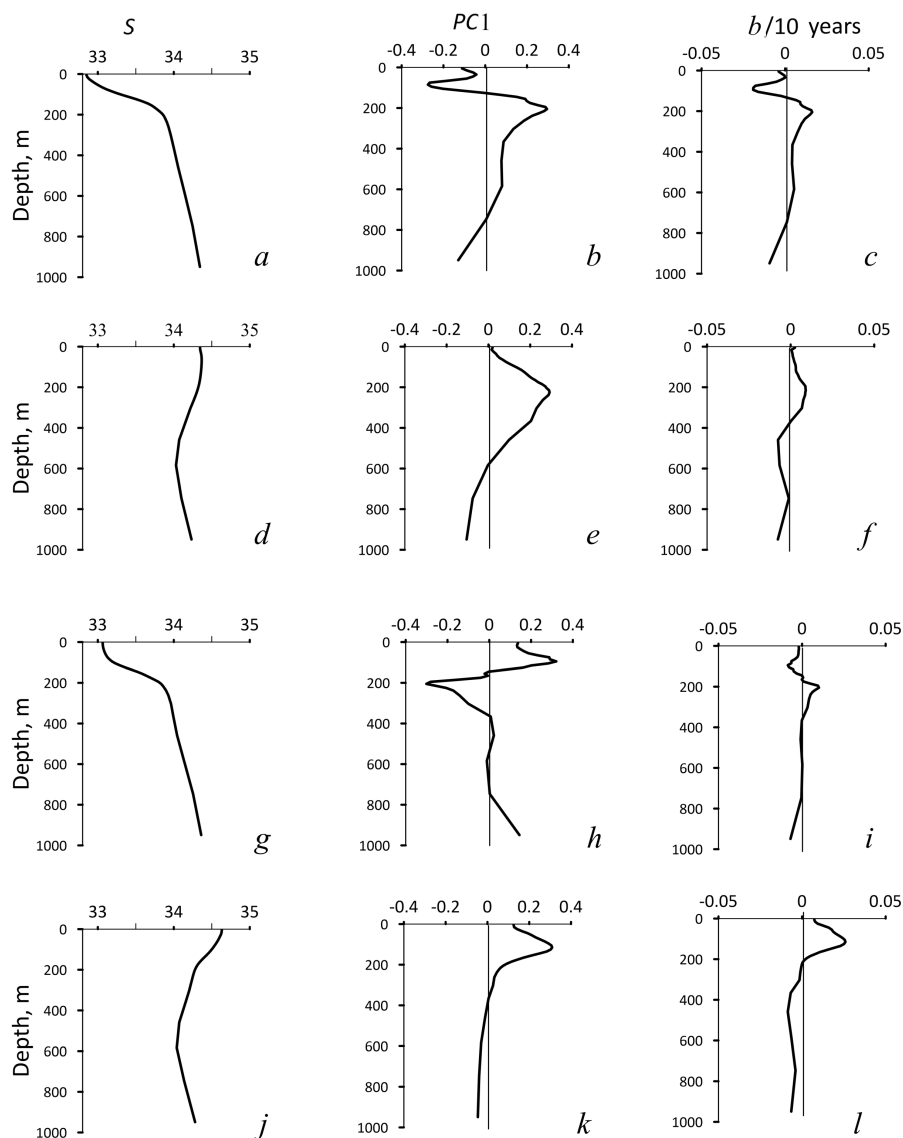


Fig. 2. Generalized curves of vertical distribution of salinity (*a, d, g, j*), principal component $PC1$ of EOF of salinity anomalies (*b, e, h, k*) and salinity trend (*b*) at different levels (*c, f, i, l*) for 2000–2022. From top to bottom: the N, W, E and S areas according to Fig. 1, *e*

As noted above, the features of the vertical structure of salinity in *N* and *E* areas are specific for the subarctic structure of waters with a monotonic increase in S with depth (Fig. 2, *a, g*), and in *W* and *S* areas – for the area of mixing waters of subarctic

and subtropical structures with a non-monotonic change salinity (Fig. 2, *d, j*) [22]. The $PC1(z)$ curves (Fig. 2, *b, e, h, k*) approximately correspond to the vertical distribution of the values of the range of its changes in the interannual variation (up to 0.07–0.09 in the upper 200-meter layer of the western and southern areas) and vertical distribution of salinity trends $b(z)$ in all areas (Fig. 2, *c, f, i, l*). The correlation coefficient (R) of fluctuations $PC1(z)$ and $b(z)$ is statistically significant and amounts to ± 0.84 –0.98. In general, the principal component $PC1$ of the interannual variability of salinity profiles in the studied areas accounts for 43% (area *E*) to 63–83% (for other areas) of the total salinity variance at different levels.

The analysis of interannual trends of statistically significant changes in the vertical structure of salinity on average for individual areas showed that the maximum negative trends ($-0.02/10$ years) were observed in the northern region (Fig. 2, *c*), and the maximum positive ones ($0.03/10$ years) – in the southern region (Fig. 2, *l*), in the layer of the upper halocline. The indicators of general trends in large-scale interannual changes in the salinity field of the studied region are the characteristics of the salinity content of the water column. According to the data in Table 1 and Fig. 1, *d–f*, within the extratropical zone of the northeastern part of the Pacific Ocean, trends in both salinization and desalination of waters in the upper, intermediate and deep layers of individual areas have prevailed in recent decades. However, in contrast to the northwestern sector of this zone [20], no statistically significant trends in salt content indicating trends in salinization or desalination of the water column of the upper 1000-m layer of the entire northeastern sector were identified. The increase in trends in the heat content of this layer of the extratropical zone of the northeastern Pacific Ocean ($\sim 2\%$) [24] was also statistically insignificant.

The spatial features of the vertical structure of the water column with different values of desalination and salinization trends are displayed on zonal and meridional sections crossing the water area of the region (Fig. 3). Over most of the area in the plane of all sections, statistically significant salinity trends of different values and signs are expressed forming the structures of large-scale salinity anomalies in various water column layers (Fig. 1, *d–f*).

The southern zonal section along 40°N crosses the western and eastern areas and the southern part of the northern one (Fig. 3, *a; 1, d*). The greatest positive salinity trends up to 0.02 – $0.03/10$ years can be seen in the upper 30-meter layer in this section center and in the 120–220 m layer in its eastern part; the greatest negative trends up to $-0.07/10$ years are observed in the upper 100-meter layer off the North American coast influenced by continental runoff and upwelling [22].

The formation of trends in interannual changes in salinity on the northern zonal section (Fig. 3, *b; 1, d*), in contrast to the southern one, takes place in the absence of noticeable horizontal latitudinal gradients in the spatial distribution of salinity within the entire 1000-meter layer. In the lower part of the upper 150-meter layer of the western part of the section, negative salinity trends with maximum values of up to $-0.08/10$ years prevail in this layer. In the upper part of the 150-meter layer in the western and eastern parts of the section at 50°N , local areas with positive S trends

are observed. The position of these areas is consistent with the horizontal distribution pattern of the $E-P$ difference values (Fig. 1, *b*). In the layer of 150–600 m over most of the section, positive salinity trends are expressed with a maximum value at the 200 m level of up to 0.02–0.04/10 years, and below it, the trend sign changes to the opposite again. The results obtained enable to detail general regional features of the interannual variability of the vertical structure of a salinity field in the northern area (Fig. 2, *c*) and others.

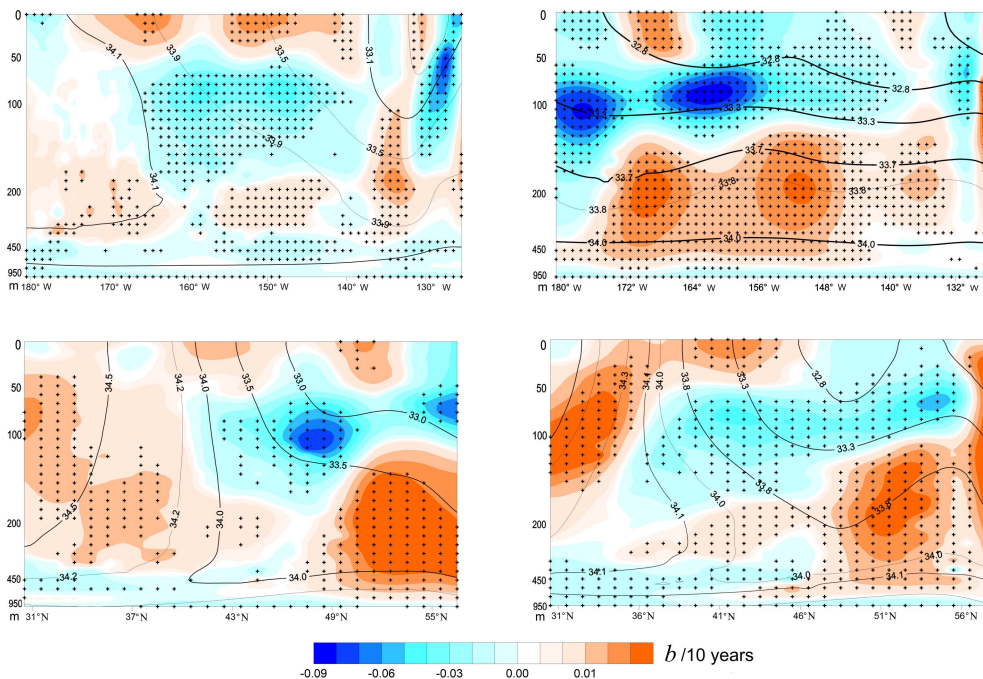


Fig. 3. Combined vertical distribution of salinity (solid lines) and salinity trends (highlighted in color) on the zonal sections along 40°N (*a*) and 50°N (*b*), and on the meridional sections along 170°W (*c*) and 150°W (*d*) in 2000–2022. Section locations are shown in Fig. 1, *d*

Formation of trends in interannual changes in salinity on meridional sections at 170°, 150° and 130°W (no Figure) occurs under the conditions of significant spatial gradients of the salinity field (Fig. 3, *c*, *d*; 1, *d*). Note that the maximum negative salinity trends with values up to $-0.07/10$ years were localized at levels of 70 and 120 m in the northern part of the western section (170°W) near the Aleutian island ridge. Areas with maximum values of positive trends S (0.06/10 years) can be observed in various parts of the upper and intermediate layers in all sections under consideration, where they are elongated in the latitudinal direction.

The analysis of maps of interannual variability of currents at 105 and 205 m levels, constructed according to GODAS data, showed that anomalous extremes of positive and negative salinity trends located near these levels correspond to the areas of localization of statistically significant trends in the current velocity module with a value exceeding ± 0.03 m/s/10 years.

Trends in the vertical and horizontal structure variability of the salinity field are reflected in the corresponding changes in the characteristics of the salinity of different water column layers (Fig. 1, *d–f*). Note that the values of salinity trends in the water column of the studied area are approximately 2–10 times (depending on the sign) less than in the northwestern part of the extratropical zone of the Pacific Ocean [20], which lies in the same climatic zone.

Correlations of interannual changes in characteristics of a salinity field with large-scale and regional processes in the ocean and atmosphere

A mutual correlation and regression analysis of interannual variations in the time series of salinity and time coefficients of the first (*PC1*) and second (*PC2*) *EOF* decomposition modes of *Qs* anomalies in the upper and intermediate layers of the water column with changes in climate indices and other indicators characterizing the dynamics of the atmosphere and ocean climate system, as well as the humidification regime in the studied region was carried out. The main characteristics of these climatic variables and their temporal variability have already been considered by the authors in the previous works [20, 24]

In the region overall, correlations between the changes in the average annual salt content values *Qs* and its principal components *PC1* and *PC2* with various climatic variables are most pronounced with the following parameters: *NPGO* indices (with a time lag of 1 year), *IPO*, *PDO* and *AD*, the first mode of *EOF* fluctuations in difference evaporation-precipitation (*E-P*) values and the second *EOF* mode of the geopotential isobaric surface *AT*₅₀₀ anomaly (Table 2).

Table 2

**Correlation coefficients of principal components and annual average salt
content values (*Qs*) in the 5–200 m and 200–460 m layers with climatic indices
for different regions for 2000–2022**

Components and regions	Parameters					
	<i>NPGO</i>	<i>IPO</i>	<i>PC1(E-P)</i>	<i>PC2(ΔAT₅₀₀)</i>	<i>PDO</i>	<i>AD</i>
5–200 m layer						
<i>PC1</i>	0.7	0.2	–0.4	–0.6	0.5	0.5
<i>PC2</i>	0.8	–0.5	0.4	0.3	–0.6	–0.6
N	0.2	–0.2	0.3	0.0	–0.3	–0.4
W	0.1	–0.4	0.5	0.5	–0.5	–0.5
E	0.5	–0.2	0.0	–0.2	–0.3	–0.3
S	–0.5	–0.6	0.5	0.7	–0.6	–0.6
Entire water area	–0.2	–0.6	0.6	0.6	–0.8	–0.8
200–460 m layer						
<i>PC1</i>	–0.6	0.1	0.0	0.0	0.2	0.1
<i>PC2</i>	–0.3	–0.4	0.5	0.5	–0.4	–0.5
N	–0.6	–0.1	0.2	0.2	–0.1	–0.2
W	0.2	–0.4	0.5	0.2	–0.5	–0.4
E	–0.6	0.0	0.4	0.3	–0.1	–0.2
S	0.3	–0.2	0.3	0.1	–0.3	–0.3
Entire water area	0.0	0.4	0.6	0.3	–0.5	–0.6

Interannual changes in some of these variables are interrelated, which leads to the identity of corresponding estimates of the correlation coefficients given in Table 2 (5–200 m layer) for pairs of variables $PC1(E-P) - PC2(\Delta AT_{500})$, $PDO - AD$. As in other areas [20], the closeness of correlations between the variability of climatic parameters, salinity and salt content fades with depth.

The maps of spatial distribution of paired regression coefficients (Fig. 4) provide visual representation of the nature of spatial features and closeness of correlations between salt content changes and the most important climatic parameters in different areas. Moreover, the corresponding schemes for each of the pairs of variables discussed above are similar. Taking into account different signs of correlation coefficients (Table 2), these features (Fig. 4, *a – c*) are in good agreement with the distribution patterns of salt content trends in the upper layer (Fig. 1, *d*).

Explained variance (R^2) of multiple regression of $PC1(Q_s)$ variability of the upper 5–200 m layer and climate variables $NPGO$, $PC1(E-P)$, $PC2(\Delta H_{500})$ and PDO during 2000–2022 was 60%, i.e. the combination of these variables satisfactorily describes the observed changes in the main salt content component (Fig. 4, *d*).

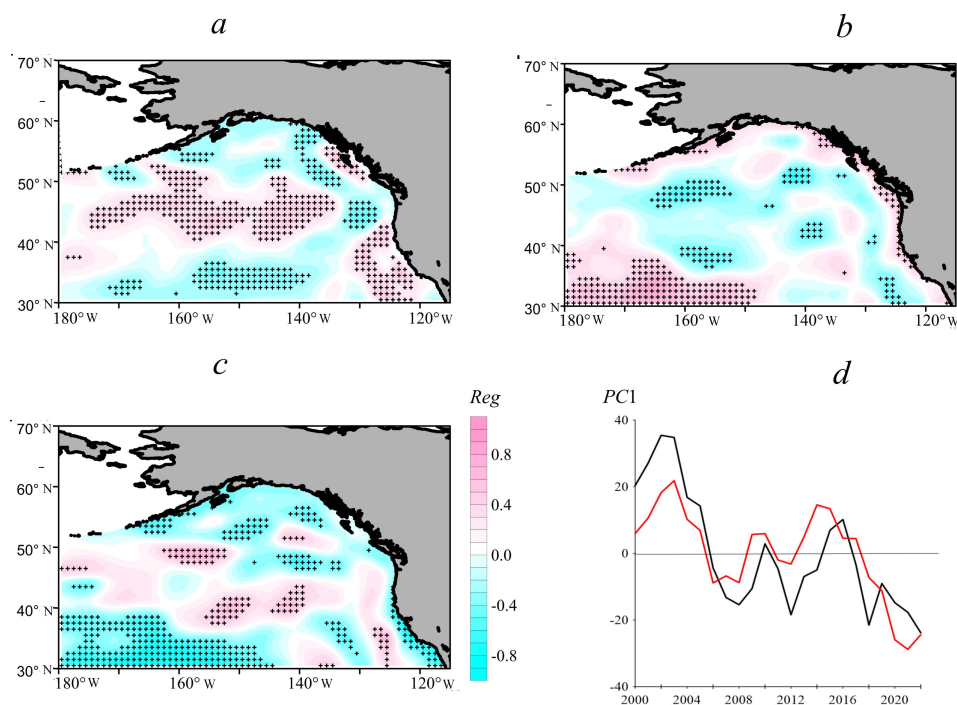


Fig. 4. Linear regression coefficients (Reg) of the fluctuations of average annual salinity anomaly values in the upper 5–200 m layer with $NPGO$ (*a*), $PC1$ of evaporation-precipitation difference (*b*) and PDO (*c*) in 2000–2022; interannual changes in $PC1(Q_s)$ of the upper layer (black curve), and fitting curve of the multiple regression equation (shown in red) with different climatic indices (*d*)

Conclusion

Over the past two decades, the interannual salinity variation at the 5 m surface level has expressed statistically significant trends of both signs with maximum values of $-0.19 \dots 0.06/10$ years. On average for the considered area, there was a tendency for a slight increase in the average salinity at this level, in contrast to the northwestern Pacific Ocean area, where significant negative salinity trends were observed. The trend values decrease with depth. In general, these values in the water column of the studied area are approximately 2–10 times (depending on the sign) less than in the northwestern part of the extratropical zone of the Pacific Ocean, which is in the same climatic zone.

Within the considered area, statistically significant trends in interannual fluctuations in the average annual precipitation and evaporation are not expressed. At the same time, the spatial distribution of trends in evaporation-precipitation ($E-P$) difference values demonstrates a predominant evaporation pattern over most of the water area, which differs from the general global trends in the hydrological cycle in the middle and high latitudes of the Northern Hemisphere, especially over the previous period.

The patterns of spatial distributions of interannual variability in salt content trends in the upper, intermediate and deep layers differ significantly from each other. Summarized: when comparing the water areas of individual considered regions, it was found that the greatest significant positive trends in salt content were observed in the upper layer of the southern region ($3.12 \text{ kg/m}^2/10$ years) and in the intermediate layer of the northern region ($1.85 \text{ kg/m}^2/10$ years), and the greatest negative trends ($-2.83 \text{ kg/m}^2/10$ years) were in the deep layer of the southern region. In general, for the region, a statistically significant positive trend in salt content was observed in the upper 1000-meter water column of the northern region, while in other areas and on average for the water area, small statistically insignificant negative trends were observed in this layer.

Correlation relations between the changes in average annual salt content values and the principal components $PC1-2$ (Qs) with various climatic variables are most pronounced with the following parameters: climate indices $NPGO$, IPO , PDO and AD , the first mode of EOF fluctuations in $PC1$ values of the evaporation-precipitation difference ($E-P$) and the second mode of EOF geopotential anomaly of the isobaric surface AT_{500} .

REFERENCES

1. Lagerloef, G., Schmitt, R., Schanze, J. and Kao, H.-Y., 2010. The Ocean and the Global Water Cycle. *Oceanography*, 23(4), pp. 82-93. <https://doi.org/10.5670/oceanog.2010.07>
2. Zika, J.D., Skliris, N., Nurser, A.J.G., Josey, S.A., Mudryk, L., Laliberté, F. and Marsh, R., 2015. Maintenance and Broadening of the Ocean's Salinity Distribution by the Water Cycle. *Journal of Climate*, 28(24), pp. 9550-9560. <https://doi.org/10.1175/JCLI-D-15-0273.1>
3. Yu, L., Josey, S.A., Bingham, F.M. and Lee, T., 2020. Intensification of the Global Water Cycle and Evidence from Ocean Salinity: A Synthesis Review. *Annals of the New York Academy of Science*, 1472(1), pp. 76-94. <https://doi.org/10.1111/nyas.14354>
4. Liu, M., Vecchi, G., Soden, B., Yang, W. and Zhang, B., 2021. Enhanced Hydrological Cycle Increases Ocean Heat Uptake and Moderates Transient Climate Change. *Nature Climate Change*, 11(10), pp. 848-853. <https://doi.org/10.1038/s41558-021-01152-0>

5. Liu, Y., Cheng, L., Pan, Y., Abraham, J., Zhang, B., Zhu, J. and Song, J., 2022. Climatological Seasonal Variation of the Upper Ocean Salinity. *International Journal of Climatology*, 42(6), pp. 3477-3498. <https://doi.org/10.1002/joc.7428>
6. Durack, P.J. and Wijffels, S.E., 2010. Fifty-Year Trends in Global Ocean Salinities and Their Relationship to Broad-Scale Warming. *Journal of Climate*, 23(16), pp. 4342-4362. <https://doi.org/10.1175/2010JCLI3377.1>
7. Helm, K.P., Bindoff, N.L. and Church, J.A., 2010. Changes in the Global Hydrological-Cycle Inferred from Ocean Salinity. *Geophysical Research Letters*, 37(18), L18701. <https://doi.org/10.1029/2010GL044222>
8. Yu, L., 2021. A Global Relationship between the Ocean Water Cycle and Near-Surface Salinity. *Journal of Geophysical Research*, 116(C10), C10025. <https://doi.org/10.1029/2010JC006937>
9. Li, G., Zhang, Y., Xiao, J., Song, X., Abraham, J., Cheng, L. and Zhu, J., 2019. Examining the Salinity Change in the Upper Pacific Ocean during the Argo Period. *Climate Dynamics*, 53(9–10), pp. 6055-6074. <https://doi.org/10.1007/s00382-019-04912-z>
10. Skliris, N., Marsh, R., Josey, S.A., Good, S.A., Liu, C. and Allan, R.P., 2014. Salinity Changes in the World Ocean since 1950 in Relation to Changing Surface Freshwater Fluxes. *Climate Dynamics*, 43(3–4), pp. 709-736. <https://doi.org/10.1007/s00382-014-2131-7>
11. Durack, P.J., 2015. Ocean Salinity and the Global Water Cycle. *Oceanography*, 28(1), pp. 20-31. <https://doi.org/10.5670/oceanog.2015.03>
12. Cheng, L., Trenberth, K.E., Gruber, N., Abraham, J.P., Fasullo, J.T., Li, G., Mann, M.E., Zhao, X. and Zhu, J., 2020. Improved Estimates of Changes in Upper Ocean Salinity and the Hydrological Cycle. *Journal of Climate*, 33(23), pp. 10357-10381. <https://doi.org/10.1175/JCLI-D-20-0366.1>
13. Cravatte, S., Delcroix, T., Zhang, D., McPhaden, M. and Leloup, J., 2009. Observed Freshening and Warming of the Western Pacific Warm Pool. *Climate Dynamics*, 33(4), pp. 565-589. <https://doi.org/10.1007/s00382-009-0526-7>
14. Friedman, A.R., Reverdin, G., Khodri, M. and Gastineau, G., 2017. A New Record of Atlantic Sea Surface Salinity from 1896 to 2013 Reveals the Signatures of Climate Variability and Long-Term Trends. *Geophysical Research Letters*, 44(4), pp. 1866-1876. <https://doi.org/10.1002/2017GL072582>
15. Shi, H. and Du, L., 2021. The Unexpected Salinity Trend Shifts in Upper Tropical Pacific Ocean under the Global Hydrological Cycle Framework. In: EGU, 2021. *EGU General Assembly 2021*. Gottingen, 2021. EGU21-14698. <https://doi.org/10.5194/egusphere-egu21-14698>
16. Rostov, I.D. and Dmitrieva, E.V., 2021. Regional Features of Interannual Variations in Water Temperature in the Subarctic Pacific. *Russian Meteorology and Hydrology*, 46(2), pp. 106-114. <https://doi.org/10.3103/S1068373921020059>
17. Loeb, N.G., Thorsen, T.J., Norris, J.R., Wang, H. and Su, W., 2018. Changes in Earth's Energy Budget during and after the "Pause" in Global Warming: An Observational Perspective. *Climate*, 6(3), 62. <https://doi.org/10.3390/cli6030062>
18. Bond, N.A., Cronin, M.F., Freeland, H. and Mantua, N., 2015. Causes and Impacts of the 2014 Warm Anomaly in the NE Pacific. *Geophysical Research Letters*, 42(9), pp. 3414-3420. <https://doi.org/10.1002/2015GL063306>
19. Amaya, D.J., Miller, A.J., Xie, S.-P. and Kosaka, Y., 2020. Physical Drivers of the Summer 2019 North Pacific Marine Heatwave. *Nature Communications*, 11, 1903. <https://doi.org/10.1038/s41467-020-15820-w>
20. Rostov, I.D. and Dmitrieva, E.V., 2024. Interannual Salinity Changes in the Upper 1000-Meter Layer of Extratropical Zone in the Northwestern Pacific Ocean under Conditions of the Intensification of Global Hydrological Cycle. *Physical Oceanography*, 31(2), pp. 194-207.
21. Corbett, C.M., Subrahmanyam, B. and Giese, B.S., 2017. A Comparison of Sea Surface Salinity in the Equatorial Pacific Ocean during the 1997–1998, 2012–2013, and 2014–2015 ENSO Events. *Climate Dynamics*, 49(9–10), pp. 3513-3526. <https://doi.org/10.1007/s00382-017-3527-y>

22. Favorite, F., Dodimead, A.J. and Nasu, K., 1976. *Oceanography of the Subarctic Pacific Region, 1960-71*. Tokyo, Japan: Kenkyusha Printing Company, 187 p.
23. Kuroda, H., Suyama, S., Miyamoto, H., Setou, T. and Nakanowatari, T., 2021. Interdecadal Variability of the Western Subarctic Gyre in the North Pacific Ocean. *Deep Sea Research Part I: Oceanographic Research Papers*, 169, 103461. <https://doi.org/10.1016/j.dsr.2020.103461>
24. Rostov, I.D., Dmitrieva, E.V. and Rudykh, N.I., 2023. Trends and Regional Features of Variability of the Northeast Pacific Ocean Thermal Conditions North of 30°N over the Last Four Decades. *Physical Oceanography*, 30(4), pp. 410-427.

About the authors:

Igor D. Rostov, Head of the Informatics and Ocean Monitoring Laboratory, V.I. Il'ichev Pacific Oceanological Institute, Far Eastern Branch of RAS (3 Baltiyskaya Str., Vladivostok, 690041, Russian Federation), CSc (Geogr.), **ORCID ID: 0000-0001-5081-7279**, rostov@poi.dvo.ru

Elena V. Dmitrieva, Senior Research Associate, Informatics and Ocean Monitoring Laboratory, V.I. Il'ichev Pacific Oceanological Institute, Far Eastern Branch of RAS (3 Baltiyskaya Str., Vladivostok, 690041, Russian Federation), CSc (Techn.), **ORCID ID: 0000-0002-0094-5296**, e_dmitrieva@poi.dvo.ru

Contribution of the co-authors:

Igor D. Rostov – development of the article structure, processing and analysis of the data, writing the article text

Elena V. Dmitrieva – collection and processing of oceanographic data, calculations, drawing design, text editing

The authors have read and approved the final manuscript.

The authors declare that they have no conflict of interest.

Original article

Comparison Analysis of Heat and Mass Transport through Fram Strait Calculated Using the Mooring and Ocean Reanalysis Data

A. V. Smirnov¹, ✉, V. V. Ivanov^{1, 2}, A. A. Sokolov¹

¹ Arctic and Antarctic Research Institute, Saint Petersburg, Russian Federation

² M. V. Lomonosov Moscow State University, Moscow, Russian Federation

✉ avsmir@aari.ru

Abstract

Purpose. This paper presents a comparison analysis of water, heat and salt transports through Fram Strait calculated by using mooring and GLORYS2v4, ORAS5, GloSea5 and C-GLORSv7 reanalyses data.

Methods and Results. Mooring data were interpolated into a regular grid with the resolutions of 0.25° over longitude and 10 m over depth using the Ordinary Kriging. Unified algorithms for both mooring and reanalysis data were applied to calculate the transports for 1997–2018 in Fram Strait (8°W, 8°E). The mooring and reanalysis time series were compared, and the results were visualized.

Conclusions. It is shown that the ensemble of reanalyses in general underestimates the transports calculated by using the observation data, by 25%. The best agreement between the results obtained from reanalyses and the observation data is obtained for the West Spitsbergen Current core which is well covered by the observation data. It is revealed that the ensemble of models describes the observation data variability the best, and the FOAM and CGLO reanalyses – the greater part of temporal variability of the flows calculated by the mooring data. The data consistency in the winter period (October – March) is shown to be higher than that in the summer one (April – September). That can be related both to the reanalysis imperfections (ice melt accounting) and the season, namely summer, when moorings are usually replaced, which can result in additional errors in combining the time series.

Keywords: Arctic Ocean, Fram Strait, current, water masses, heat and mass transport, moorings, direct measurements, reanalysis

Acknowledgments: The study was carried out with support of the Russian Science Foundation grant № 24-17-00041. The work by A. A. Sokolov was supported by the Russian Science Foundation grant № 24-27-00221.

For citation: Smirnov, A.V., Ivanov, V.V. and Sokolov, A.A., 2024. Comparison Analysis of Heat and Mass Transport through Fram Strait Calculated Using the Mooring and Ocean Reanalysis Data. *Physical Oceanography*, 31(3), pp. 364–386.

© 2024, A. V. Smirnov, V. V. Ivanov, A. A. Sokolov

© 2024, Physical Oceanography

Introduction

Information about the state of the ocean in modern oceanological research can be obtained using instrumental measurements, numerical modeling, and their combination – reanalysis. Remote and satellite observations allow to monitor the ocean surface and ice cover state, but do not extend to the entire water column, where significant hydrophysical processes develop. Contact observations in modern oceanography include primarily CTD (Conductivity Temperature Depth) soundings, current velocity measurements with an



acoustic Doppler profiler (ADCP), data from autonomous moored ¹ and drifting profiling buoys (ARGO ², ITP ³). Based on the measurement data of thermohaline characteristics, it is possible to calculate relative water transport rates along hydrological sections. The use of data from satellite altimeters and scatterometers allows to reduce relative water transport rates to absolute ones [1, 2]. If measurements are carried out on spatially close sections, these data can be used to study changes in ocean characteristics and determine trends in changes for individual regions or the ocean as a whole [3]. Ocean reanalyses obtained through observational data assimilation in numerical models have recently become an alternative source of information for studying hydrophysical structure of waters and their spatiotemporal variability [4, 5]. Hydrophysical parameters simulated in numerical models and reanalysis products, as a rule, differ from instrumental measurement data, which predetermines the need for an objective estimate of calculation quality by comparison with the data from direct measurements in the ocean.

The present paper studied the Fram Strait, which is the widest deep-sea strait connecting the North European Basin (NEB) with the Arctic Basin (AB) of the Arctic Ocean (AO) [6]. Through the eastern part of the Fram Strait with the West Spitsbergen Current, warm salty waters of Atlantic origin enter the AB, which are commonly called Atlantic waters (AW) [7], and through the western part of the strait, cold surface Arctic waters and cooled desalinated intermediate waters are transported to the NEB. The processes of heat and mass transport through the Fram Strait, primarily associated with AW, the main advective heat source for AB [8], have always been the focus of polar oceanographic research [9–11]. According to the existing historical estimates, the AW flux through the Fram Strait varies within very wide limits: from 1.4 to 7.1 Sv [12]. In this case, a significant part of the dispersion accounts for short-period intra-annual variability [13]. Detailed instrumental measurements of current velocity on a repeating section along 79°N started in 1997 and continuing to the present day within the ASOF international project (Arctic and Subarctic Ocean Fluxes) confirmed Ogard's hypothesis and showed that the total average annual flux in the West Spitsbergen Current is within 6.6 ± 0.4 Sv and the AW flux share (with a temperature over 2 °C) accounts for only 3.0 ± 0.2 Sv and the rest is the share of seasonally varying eddy transport [11].

The aim of the present paper was a quantitative comparison of heat and mass transport processes calculated from long-term instrumental measurements in the Fram Strait within the ASOF project framework with the products of ocean reanalyses. The relevance of such a comparison is due to the widespread use of ocean reanalyses to study the hydrophysical structure of the World Ocean waters, including the AO [14–16], in the virtual absence of objective criteria to judge how adequately the parameters of large-scale transport in the ocean simulated in reanalyses correspond to those observed in real life. The paper presents the results of a comparative analysis of volume, heat and salt fluxes calculated from instrumental observations at moorings in the Fram Strait with similar fluxes calculated from the GLORYS2v4, ORAS5, GloSea5 and C-GLORSv7 reanalyses.

¹ Nansen and Amundsen Basins Observational System. *NABOS*. [online] Available at: <https://uaf-iarc.org/nabos/> [Accessed: 03 June 2024].

² *ARGO*. [online] Available at: <http://www.argo.ucsd.edu/> [Accessed: 03 June 2024].

³ Woods Hole Oceanographic Institution. *Ice Tethered Profilers*. [online] Available at: <https://www2.whoi.edu/site/itp/> [Accessed: 03 June 2024].

Research data and methods

The study used data from instrumental observations in the Fram Strait carried out as part of the ASOF international project (available at: <https://asof.awi.de/science/projects/13-monitoring-of-oceanic-fluxes-across-fram-strait/>) by scientists from the Alfred Wegener Institute, Germany (AWI) and the Norwegian Polar Institute (NPI). AWI moorings cover the eastern part of the strait, while NPI moorings provide monitoring of its western part (Fig. 1).

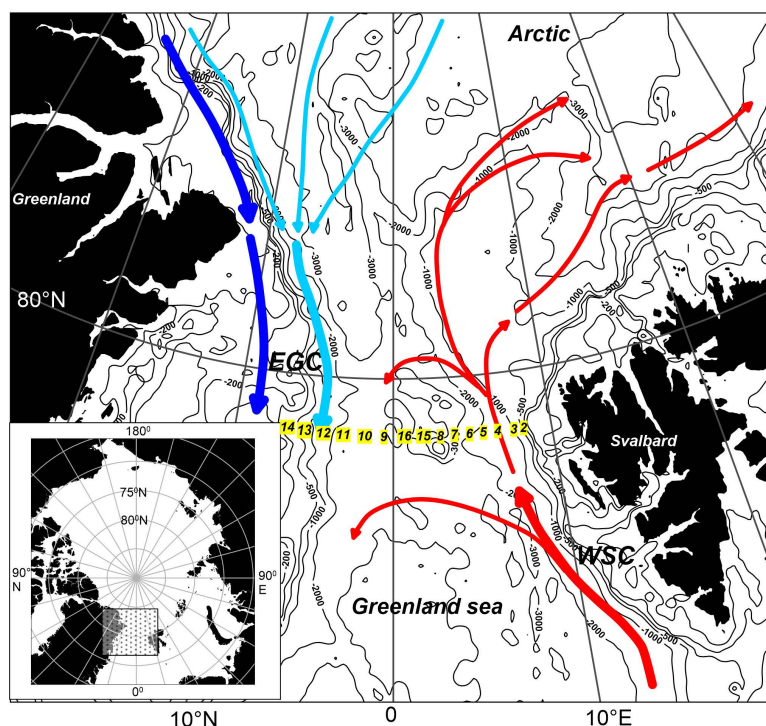


Fig. 1. Spatial positions of moorings (numbers against a yellow background) selected for analysis. Red curves show the West Spitsbergen current (WSC), blue curves – the East Greenland coastal current, and light blue ones – the East Greenland current (EGC)

Both institutes started the Fram Strait monitoring in 1997 and continue to this day. Over the past period, the position of the moorings has changed: some were excluded from the observation network, some were added, some changed their location. To measure temperature and conductivity, SBE 37 with a measurement accuracy of 0.1% pressure, 0.001 °C temperature and 0.001 S/m conductivity was used (available at: www.seabird.com). Current velocity was measured using RCM-7, RCM-9 (with an accuracy of 0.01 m/s) and ADCP 300 KHz (with an accuracy of 0.01 m/s).

Instrumental observations of AWI

AWI measurement data are presented at PANGAEA (available at: www.pangaea.de), which contains two generalizing data sets: 1997–2016⁴ and

⁴ Von Appen, W.-J., Beszczynska-Möller, A., Schauer, U. and Fahrbach, E., 2019. *Physical Oceanography and Current Meter Data from Moorings F1-F14 and F15/F16 in the Fram Strait, 1997-2016* [dataset bibliography]. PANGAEA. <https://doi.org/10.1594/PANGAEA.900883>

2016–2018⁵. Collectively, data from 171 moorings were selected and downloaded from September 1997 to June 2018.

Most moored buoys were positioned to obtain long continuous series of observations. Such time series had the same name (*F1–F10*), although their coordinates differed somewhat from year to year. The downloaded initial data underwent additional processing, which included formatting, grouping by parameters (separately for temperature, electrical conductivity, and current velocity components) and by time. For each day, all available values for a given parameter were selected and recorded in files in the form “latitude, longitude, depth, value”. The values within one day were averaged so that the data discreteness was consistent with the reanalyses data discreteness.

Although the initial data were quality controlled [17], the time series analysis indicated that additional procedures were required. It was revealed that six time series had negative measurement horizons. Such data were rejected. Additionally, the data beyond the boundaries of physical variability were filtered out. The criteria below were selected based on statistical analysis of the original data. The data beyond 3σ were excluded from the analysis. Thus, for temperature the range would be $-2.5 \div 6$ °C, for salinity $30 \div 36$ PSU. The current velocity components were filtered out if the velocity exceeded 2 m/s. The longest time series with moorings located at 78.5°N were selected from the processed data array (Fig. 1). The criterion for selecting measurement data of a particular mooring for subsequent analysis was the duration of the time series and spatial position, which allows the data to be used to construct a vertical section through the Fram Strait.

F1 mooring data were not used due to the short time series, while the *F15* and *F16* mooring series, which also produced relatively short time series, were retained as they were located inside the section and, due to this, allowed to improve spatial interpolation results. The final composition of AWI mooring included in the analysis is given in Table 1.

Table 1

Mooring metadata

Autonomous buoy station	Longitude, °E	Time periods	Autonomous buoy station	Longitude, °E	Time periods
<i>F1</i>	8.6	1997–2009	<i>F16</i>	0.4	2002–2014
<i>F2</i>	8.3	1997–2018	<i>F9</i>	−0.4	1997–2016
<i>F3</i>	8.0	1997–2018	<i>F10</i>	−2.0	1997–2016
<i>F4</i>	7.0	1997–2018	<i>F11</i>	−3.0	1997–2015
<i>F5</i>	6.0	1997–2018	<i>F12</i>	−4.0	1998–2015
<i>F6</i>	5.0	1997–2016	<i>F13</i>	−5.0	1997–2015
<i>F7</i>	4.0	1997–2015	<i>F14</i>	−6.5	1997–2015
<i>F8</i>	2.7	1997–2014	<i>F17</i>	−8.0	2003–2015
<i>F15</i>	1.6	2002–2014			

⁵ Von Appen, W.-J., 2019. *Physical Oceanography and Current Meter Data (Including Raw Data) from FRAM Moorings in the Fram Strait, 2016-2018* [dataset bibliography]. PANGAEA. <https://doi.org/10.1594/PANGAEA.904565>

Instrumental observations of NPI

The data from the NPI moorings are available at <https://www.npolar.no/en/>. Two data sets were downloaded: 1997–2009⁶ and 2009–2015⁷. The downloaded data were converted into a format like that used for the AWI data. The quality control described in the previous subsection was applied to the NPI data. Values outside physical variability boundaries were filtered out, as well as erroneous data and metadata found in the analysis of the original time series. Figure 1 shows the spatial location of NPI moorings, their metadata are shown in Table 1.

F17 mooring was excluded from further analysis due to its insufficiently long time series. F11–F14 moorings changed their position in 2002 from 79°N to 78.5°N to match the position of the AWI buoys.

The processed arrays of AWI and NPI instrumental observations were combined into a single array to obtain the best spatial coverage of the Fram Strait. According to the method [10], monthly data averaging was used. The total time coverage of the single dataset was 217 months (August 1997 – August 2015).

Reanalyses data

Instrumental observations at moorings today are probably one of the most reliable sources of information on the temporal variability of the vertical hydrophysical structure of the World Ocean waters. However, due to objective reasons, the amount of instrumental data is limited in time and space, which requires the use of alternative sources of information. They include ocean reanalysis products obtained by synthesizing observations and mathematical modeling [18] and allowing a significantly more detailed structure and water dynamics simulation.

In the present paper Global Ocean Ensemble Physics Reanalysis⁸ developed by Copernicus Marine Environment Monitoring Service (CMEMS) is used. It is a compilation of four ocean reanalyses:

- GLORYS2V4 (Mercator Ocean, France),
- ORAS5 (ECMWF, EU),
- GloSea5 (Met Office, Great Britain),
- C-GLORSv7 (CMCC, Italy).

Global Ocean Ensemble Physics Reanalysis (further – CMEMS Reanalysis) data presented on a regular grid for the entire World Ocean with a spatial step of 0.25° in latitude and longitude and a time resolution of 1 day. Now, the time range of the array is 27 years (from January 1993 to December 2019). In this study, the values of the following parameters were used: potential temperature, °C; practical salinity, PSU; current velocity components directed to the north (*u*) and east (*v*), m/s. Monthly, seasonal and annual averages were calculated using daily data. Seasonal averaging was carried out over two periods for each year: winter (October – March) and summer (April – September). The CMEMS reanalysis grid (0.25°)

⁶ De Steur, L., 2019. *Moored Current Meter Data from the Western Fram Strait 1997-2009* [data set]. Norwegian Polar Institute. <https://doi.org/10.21334/npolar.2019.8bb85388>

⁷ De Steur, L., 2021. *Moored Current Meter and Hydrographic Data from the Fram Strait Arctic Outflow Observatory since 2009* [data set]. Norwegian Polar Institute. <https://doi.org/10.21334/npolar.2021.c4d80b64>

⁸ Copernicus Marine Service Information (CMEMS). Marine Data Store (MDS). *GLOBAL_MULTIYEAR_PHY_ENS_001_031: Global Ocean Ensemble Physics Reanalysis*. doi:10.48670/moi-00024 [Accessed: 04 June 2024].

permits to avoid additional spatial interpolation. Since the algorithm for calculating the integral transport of volume, heat, and mass (see next section) does not require additional re-interpolation of values to standard horizons, the vertical horizons in the reanalysis grid were not recalculated into the calculation grid.

Spatial interpolation

To carry out the calculation of heat and mass transport processes and subsequent comparative analysis, the initial data of the combined array of instrumental observations were interpolated into regular grid nodes (in the format of a vertical section with a fixed step in depth and longitude) (Fig. 2).

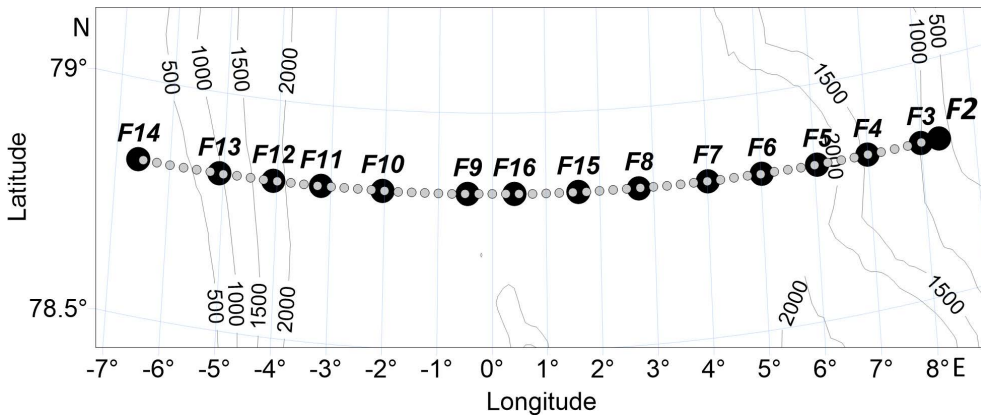


Fig. 2. Geographical location of moorings and regular grid nodes, where spatial interpolation was carried out

Ordinary kriging was chosen as an interpolation method [19]. The term "kriging" refers to a family of linear spatial regression algorithms. The use of kriging methods permits to carry out an interpolation procedure with data that have a few specific features, such as spatial heterogeneity, significant anisotropy, and presence of trends in the data [20]. The Surfer package (available at: <https://www.goldensoftware.com/>) was chosen as a software implementation of the kriging method.

All 217 data files for each month were restored to grid nodes, the horizontal step of which was 0.25° ($6.5^\circ\text{W} - 8^\circ\text{E}$), while the data on the vertical axis were interpolated with a step of 10 m. For further use, the interpolation results were converted into the net CDF format, which allowed to apply a unified program code for subsequent calculations. At the *in situ* conversion stage, the water temperature was converted to potential. Practical salinity and current velocity remained unchanged. By analogy with the reanalysis data, the obtained interpolated measurement data on the moorings were averaged by season (April – September and October – March) and by year.

Figure 3 shows the annual values of meridional current velocities according to the mooring data (Fig. 3, *a*) and reanalysis (Fig. 3, *b*).

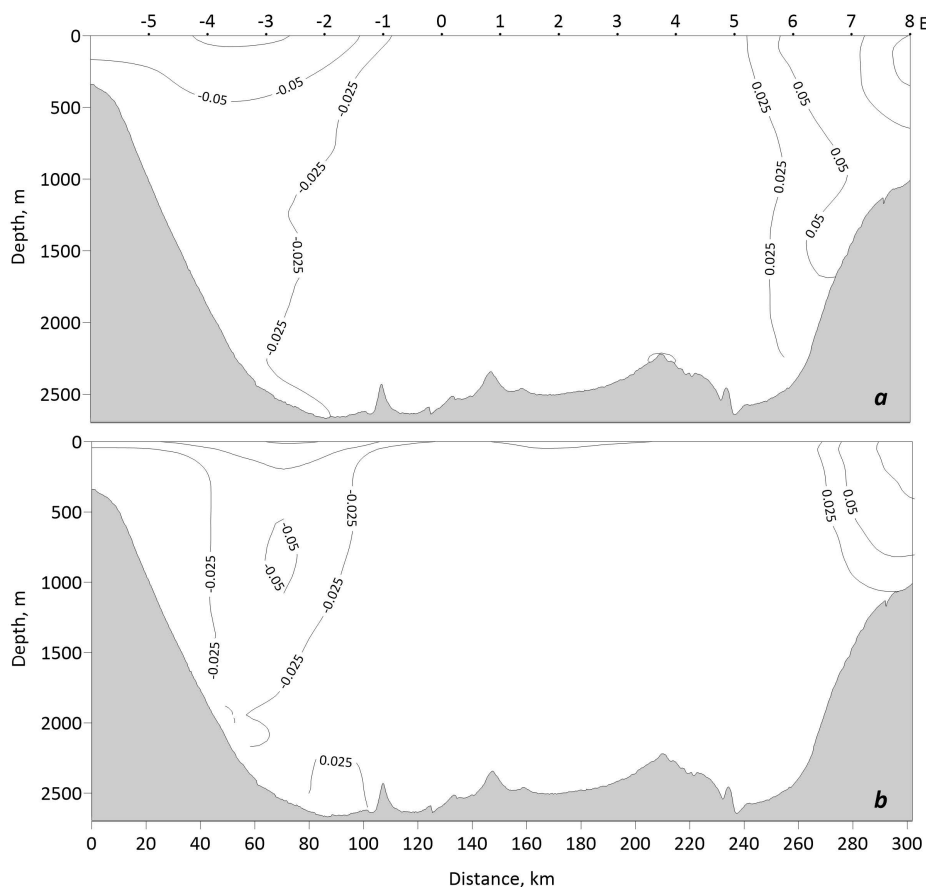


Fig. 3. Annual average values of current meridional velocities based on the mooring (a) and reanalysis (b) data

Calculation of total transport of water, heat and salt

The total transport of volume, heat and salt through the section was chosen as the main characteristic for comparison of measured time series and CMEMS reanalyses data. The total water transport (D_w) represents the integral volume transport in each depth range through a unit segment corresponding to a section node. The integral D_w along the entire length of the section determines the total volume transport through the entire section in the direction normal to the section axis. For the Fram Strait, the following statement is true:

$$Vn = v_0, \quad (1)$$

where Vn is current velocity normal to the section axis; v_0 is northward component of current velocity.

For each node of the section, $Vn(z)$ was integrated vertically to obtain the total water transport D_w ($\text{m}^2 \cdot \text{s}^{-1}$):

$$D_w = \int_{z_l}^{z_{\text{up}}} Vn(z) \approx \sum_j 0,5(Vn_j + Vn_{j+1})(z_{j+1} - z_j), \quad z_l \leq z_j \leq z_{\text{up}}. \quad (2)$$

Product of temperature anomaly ($T(z) - T_{\text{ref}}$) and current velocity proportional to heat flux (D_H , $\text{W} \cdot \text{m}^{-1}$):

$$D_H = \int_{z_l}^{z_{\text{up}}} \rho c_p V n(z) (T(z) - T_{\text{ref}}) dz \approx \sum_j 0.5 \rho c_p [V n(T_j - T_{\text{ref}}) + V n(T_{j+1} - T_{\text{ref}})] (z_{j+1} - z_j), \quad z_l \leq z_j \leq z_{\text{up}}. \quad (3)$$

The product of salinity anomaly ($S(z) - S_{\text{ref}}$) and current velocity is proportional to the salt flux (D_S , $\text{kg} \cdot \text{m}^{-1} \cdot \text{s}^{-1}$):

$$D_S = \int_{z_l}^{z_{\text{up}}} \rho V n(z) (S(z) - S_{\text{ref}}) dz \approx \sum_j 0.5 \rho [V n_j (S_j - S_{\text{ref}}) + V n_{j+1} (S_{j+1} - S_{\text{ref}})] (z_{j+1} - z_j), \quad z_l \leq z_j \leq z_{\text{up}}. \quad (4)$$

In formulas (2)–(4), z_l and z_{up} are the lower and upper integration limits; c_p is specific heat capacity of sea water at constant pressure; ρ is sea water density (c_p and ρ were calculated using the *TEOS-10* equation of state); $V n_j$ is current velocity at z_j level; T_j and S_j are temperature and salinity measured at z_j level, $T_{\text{ref}} = -1.8^\circ\text{C}$, $S_{\text{ref}} = 0$, respectively.

The total transport values (F_W , F_H and F_S) were calculated by horizontally integrating the depth-averaged fluxes along the entire length of the section (L). The following formulas (5)–(7) were used:

$$F_W = \int_{(L)} D_W dl \approx \sum_{i=1}^5 0.5 (D_{W_i} + D_{W_{i+1}}) \Delta l_{i,i+1}, \quad (5)$$

$$F_H = \int_{(L)} D_H dl \approx \sum_{i=1}^5 0.5 (D_{H_i} + D_{H_{i+1}}) \Delta l_{i,i+1}, \quad (6)$$

$$F_S = \int_{(L)} D_S dl \approx \sum_{i=1}^5 0.5 (D_{S_i} + D_{S_{i+1}}) \Delta l_{i,i+1}, \quad (7)$$

where i is section node number relative to its beginning; $\Delta l_{i,i+1}$ is distance between two adjacent nodes, indicated as i and $i + 1$.

It should be noted that the algorithm above was modified for the reanalysis data. For example, in the NEMO model that underlies the GLOR, ORAS and CGLO reanalyses, density is not a function of temperature and salinity. Therefore, in formulas (3)–(4), the c_p and ρ quantities were taken as constants ($c_p = 3989.24495292815 \text{ J/(kg} \cdot \text{K)}$, $\rho = 1035 \text{ kg/m}^3$).

The above method for calculating heat and mass transport was implemented in the *Julia* language. The data from instrumental observations and reanalyses were processed by the same program code. The calculation results are presented in the next section.

Results and their discussion

Total heat and mass transport through the Fram Strait

A comparative analysis of instrumental observation and reanalysis data started with monthly data. Figures 4–6 show time series of volume, heat and salt transport through the Fram Strait for various averaging periods in 1997–2015. The monthly series were smoothed with a moving average over an 11-month window and seasonal and annual data were left unchanged. Integrated values were calculated for the entire section ($6.5^\circ\text{W} - 8^\circ\text{E}$) and throughout the entire water column.

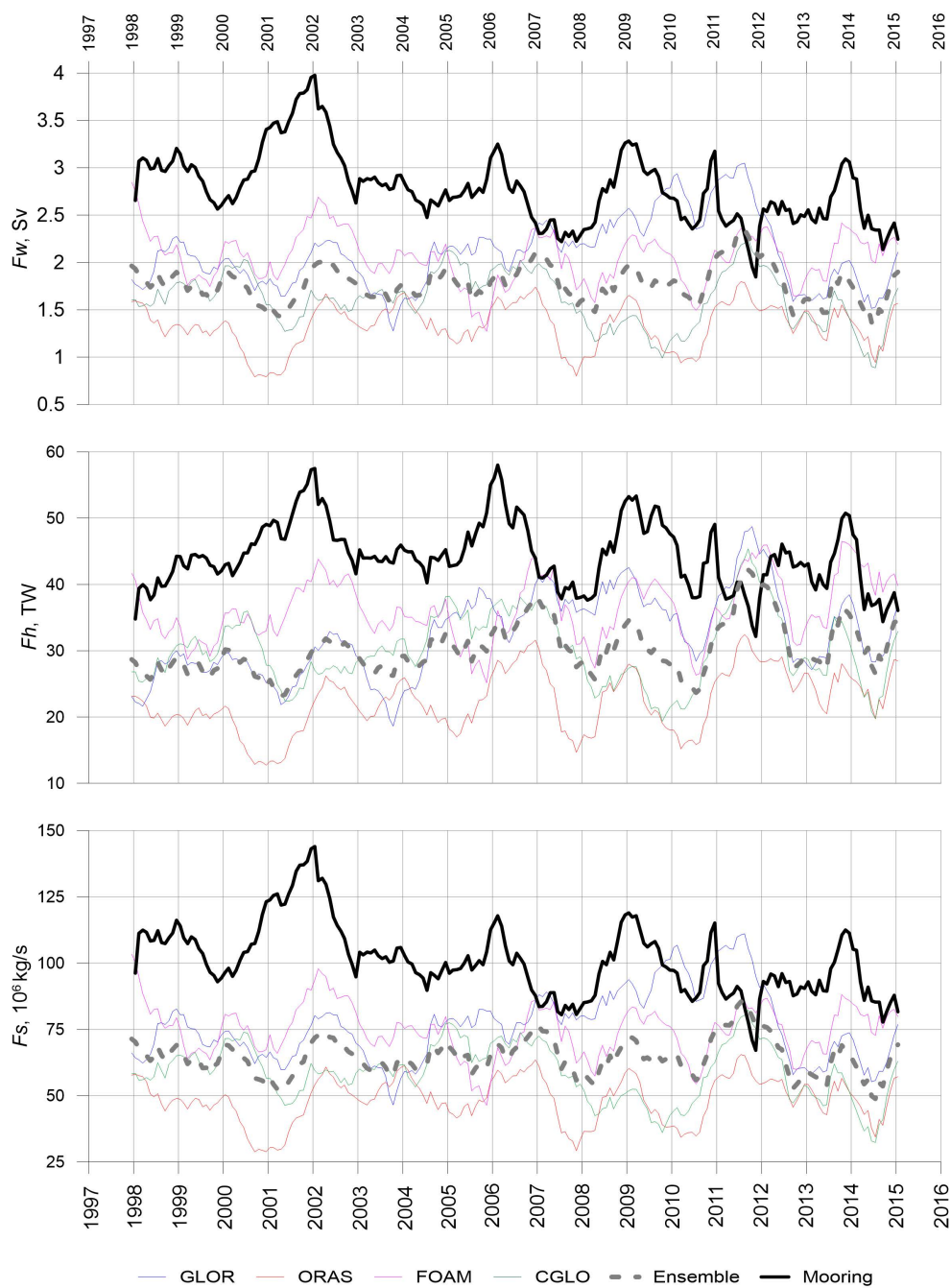


Fig. 4. Time series of heat and mass transport through the Fram Strait calculated by monthly average data

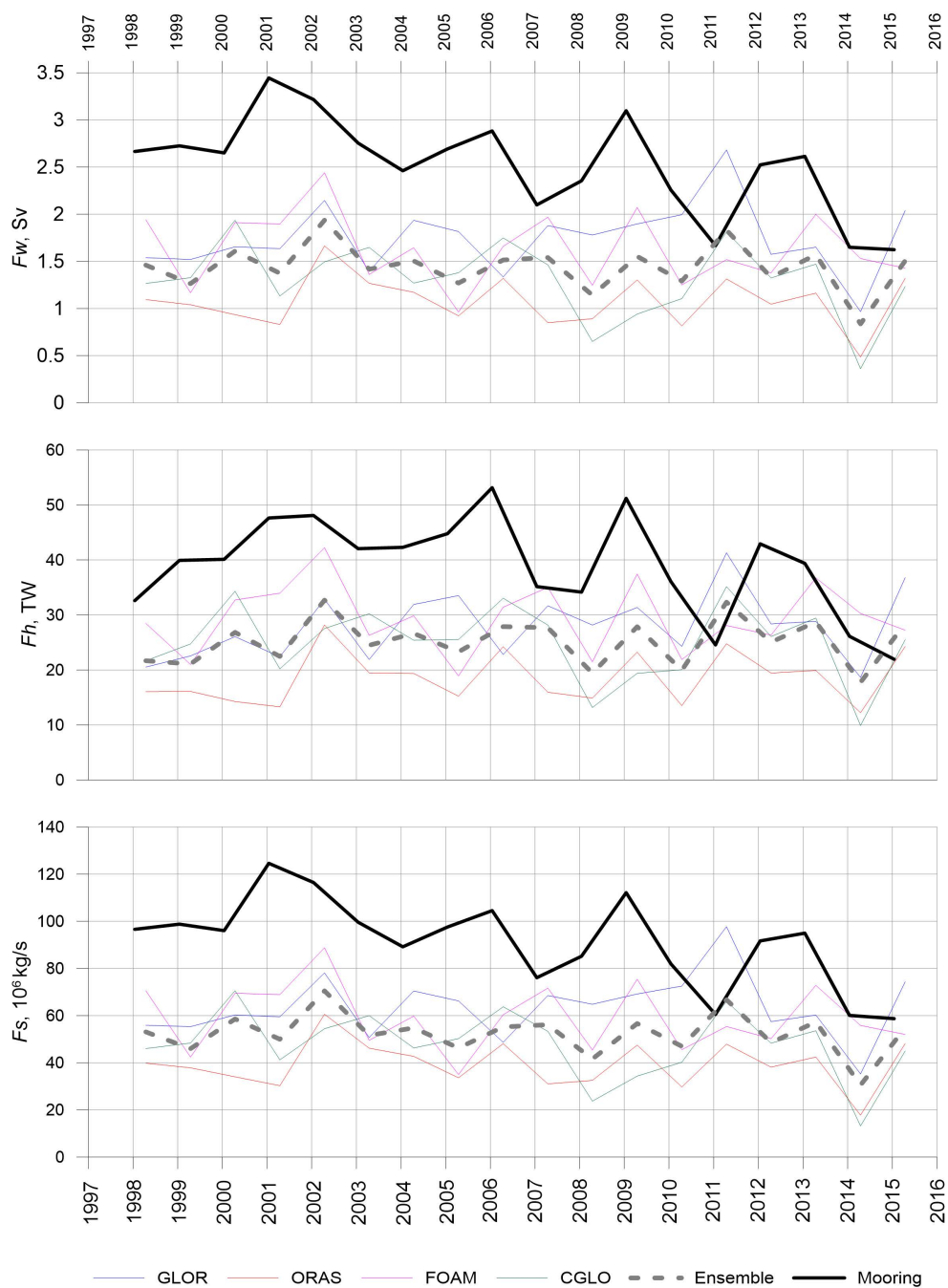
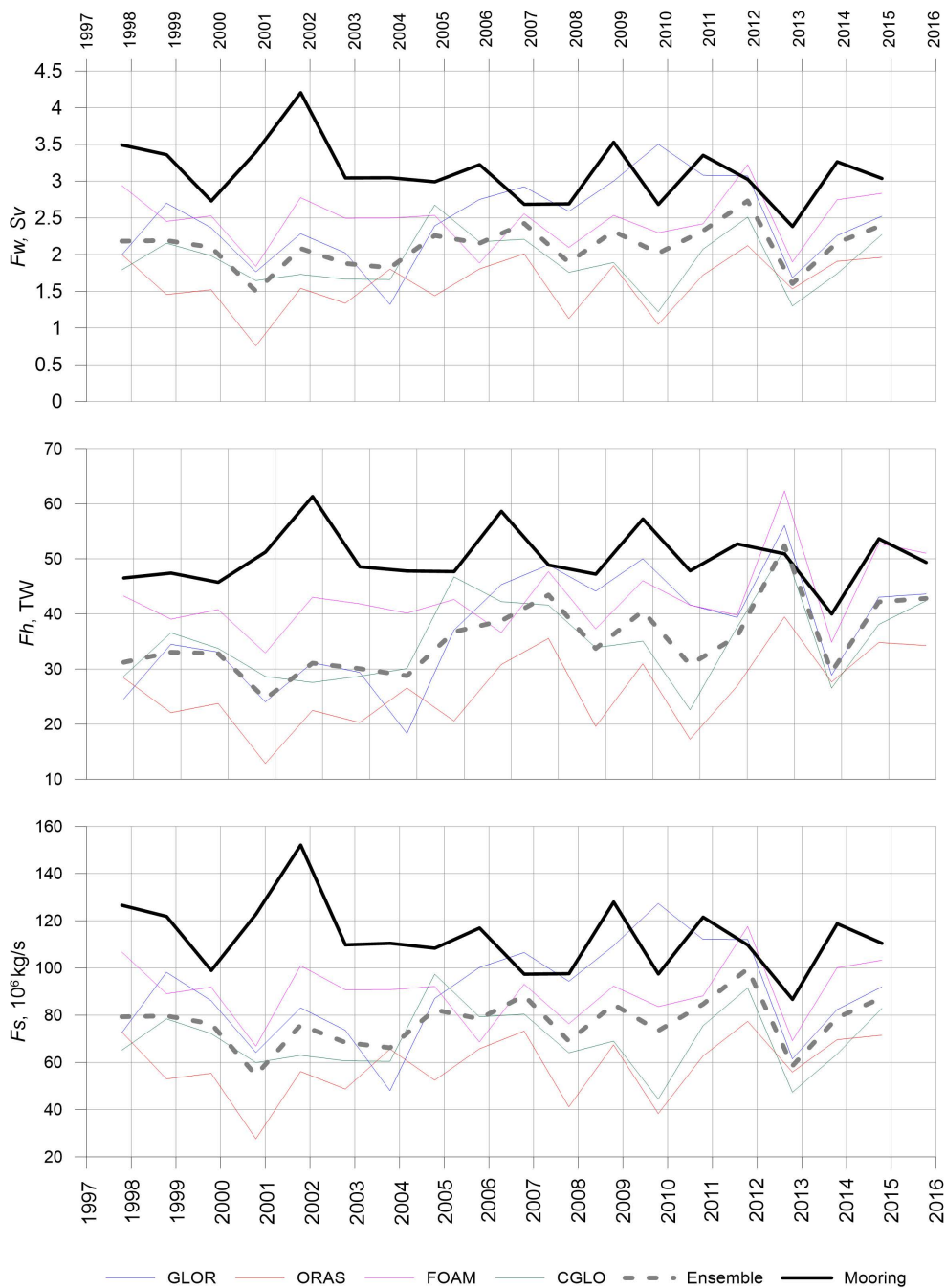


Fig. 5. Time series of heat and mass transport through the Fram Strait calculated by seasonal (April – September) average data



F i g. 6. Time series of heat and mass transport through the Fram Strait calculated by seasonal (October – March) average data

Figure 4 shows that the reanalysis data generally underestimate heat and mass transport value. Thus, the average value of volume transport, according to the mooring data, is higher than the ensemble average by more than 30% and its standard deviation is 50% higher. A similar picture is observed in heat and salt transport (Table 2).

Seasonal time series (Figs. 5–6) show that reanalyses underestimate heat and mass transport in summer, while better consistency is observed in winter. Annual averaging logically occupies an intermediate position (Fig. 7).

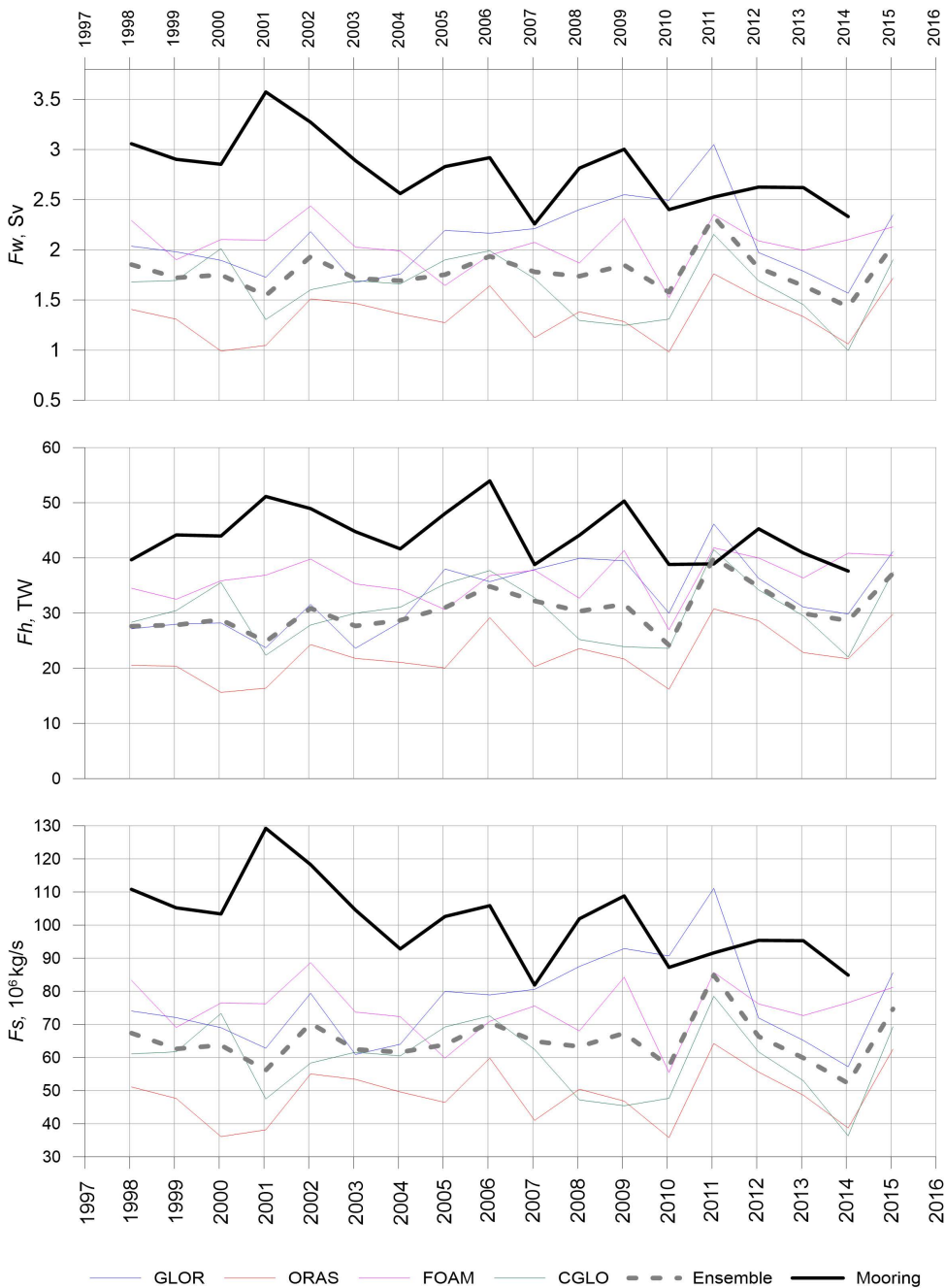


Fig. 7. Time series of heat and mass transport through the Fram Strait calculated by annual average data

Table 2

Basic statistical characteristics of the studied monthly series of data

Parameter	GLOR	ORAS	FOAM	CGLO	Ensemble	Mooring
<i>F_w</i>						
Minimum	1.57	0.98	1.53	1.00	1.43	2.26
Maximum	3.05	1.76	2.44	2.15	2.33	3.57
Average	2.11	1.34	2.05	1.63	1.78	2.79
Standard deviation	0.37	0.24	0.23	0.31	0.20	0.34
Dispersion	0.14	0.06	0.05	0.10	0.04	0.12
<i>F_h</i>						
Minimum	24.0	16.0	27.0	22.0	24.0	38.0
Maximum	46.0	31.0	42.0	42.0	40.0	54.0
Average	33.0	22.0	36.0	30.0	31.0	44.0
Standard deviation	6.0	5.0	4.0	6.0	4.0	5.0
Dispersion	36.0	25.0	16.0	36.0	16.0	25.0
<i>F_s</i>						
Minimum	57.0	36.0	56.0	36.0	52.0	82.0
Maximum	111.0	64.0	89.0	79.0	85.0	129.0
Average	77.0	49.0	75.0	59.0	65.0	101.0
Standard deviation	14.0	9.0	8.0	11.0	7.0	12.0
Dispersion	196.0	81.0	64.0	121.0	49.0	144.0

Discrepancy between the mooring data and reanalyses can be partially explained by measurement data processing method. Unlike reanalyses, where there are no missing values, observational data are not continuous. The spatial averaging algorithms used can make a significant contribution to the simulated field quality. The ordinary kriging used in the present study showed satisfactory results. Kriging is sensitive to linearly arranged data as well as duplicate data. It should be noted that the problem of extrapolation is also acute in mooring data processing. Often the first horizon is below 50 m and the last one does not reach the bottom. To calculate integral transports, we are forced to use a fixed layer (in this study, the entire water column). For this purpose, the first measurement horizon is extrapolated to the surface. Bottom horizons are modelled using interpolation (if there are other observations in the area). Another factor explaining discrepancies in heat and mass transport estimates may be an insufficiently accurate assessment of recirculating waters in the Fram Strait in reanalysis data.

Heat and mass transport in the core of the Atlantic waters

A comparative analysis of series of heat and mass transport values in the AW core (temperature above 2 °C) was carried out to estimate the influence of shortcomings of the instrumental observation data and reanalysis products listed in the previous subsection on the result of comparison of heat and mass transport processes [10, 21]. It permitted to exclude data extrapolation, improve spatial interpolation quality, and avoid AW recirculation branches in the Fram Strait. In addition, the heat and mass transport estimate in the AW core is of fundamental scientific interest [11]. The methodology for calculating the integral transport of volume, heat and mass was like that described above for the entire Fram Strait. The calculation results are presented in Table 3.

Table 3

**Basic statistical characteristics of the studied monthly series of data
for the Atlantic Ocean waters**

Parameter	GLOR	ORAS	FOAM	CGLO	Ensemble	Mooring
<i>F_w</i>						
Minimum	0.00	0.00	0.00	0.00	0.00	0.00
Maximum	2.44	2.58	3.20	2.87	2.52	3.59
Average	1.02	0.78	1.39	1.25	1.11	1.47
Standard deviation	0.60	0.52	0.61	0.52	0.45	0.64
Dispersion	0.36	0.27	0.37	0.27	0.20	0.41
<i>F_h</i>						
Minimum	0.0	0.0	0.0	0.0	0.0	0.0
Maximum	54.0	47.0	69.0	60.0	55.0	87.0
Average	21.0	15.0	29.0	26.0	23.0	32.0
Standard deviation	13.0	11.0	13.0	11.0	10.0	15.0
Dispersion	169.0	121.0	169.0	121.0	100.0	225.0
<i>F_s</i>						
Minimum	0.0	0.0	0.0	0.0	0.0	0.0
Maximum	89.0	94.0	117.0	105.0	92.0	130.0
Average	37.0	28.0	51.0	46.0	40.0	53.0
Standard deviation	22.0	19.0	22.0	19.0	16.0	23.0
Dispersion	484.0	361.0	484.0	361.0	256.0	529.0

Figure 7 shows that the heat and mass transport values within the Atlantic waters have significantly better consistency. The mooring data still show overestimations, but the residual does not exceed 25% of the ensemble mean. It is noteworthy that some reanalyses turned out to be much closer to the mooring data. Thus, the FOAM reanalysis underestimates the average values by only 6% and CGLO by 15%. The correlation analysis demonstrated that the ensemble of reanalyses shows the best agreement with observational data (Table 4).

If we talk about a separate model, then FOAM most closely describes the field data. Analysis of seasonal data showed that in the summer season reanalyses still significantly underestimate heat and mass transport in the Atlantic waters. The better consistency is observed in winter.

T a b l e 4

**Correlation coefficients between monthly averaged mooring data
and reanalyses**

Transport	GLOR	ORAS	FOAM	CGLO	Ensemble
F_w	0.37	0.46	0.52	0.50	0.59
F_h	0.47	0.53	0.55	0.51	0.62
F_s	0.37	0.46	0.52	0.50	0.59

Considering better consistency of the results for the AW core, equations of linear regression were constructed relating the heat and mass transport values calculated from instrumental observations and reanalysis products for the AW core (Fig. 8).

The time series of heat and mass transport through the Fram Strait based on the average monthly, seasonal, and annual data for the Atlantic waters are presented in Figs. 9–12.

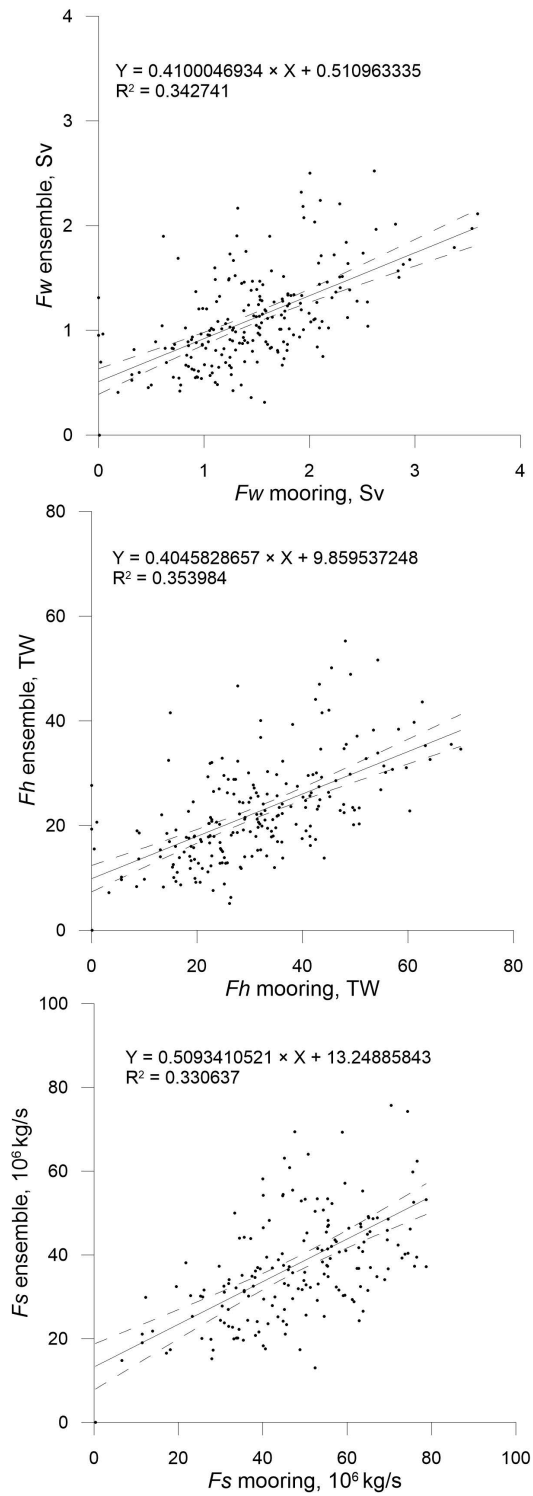


Fig. 8. Equations of linear regression between mooring data and model ensemble

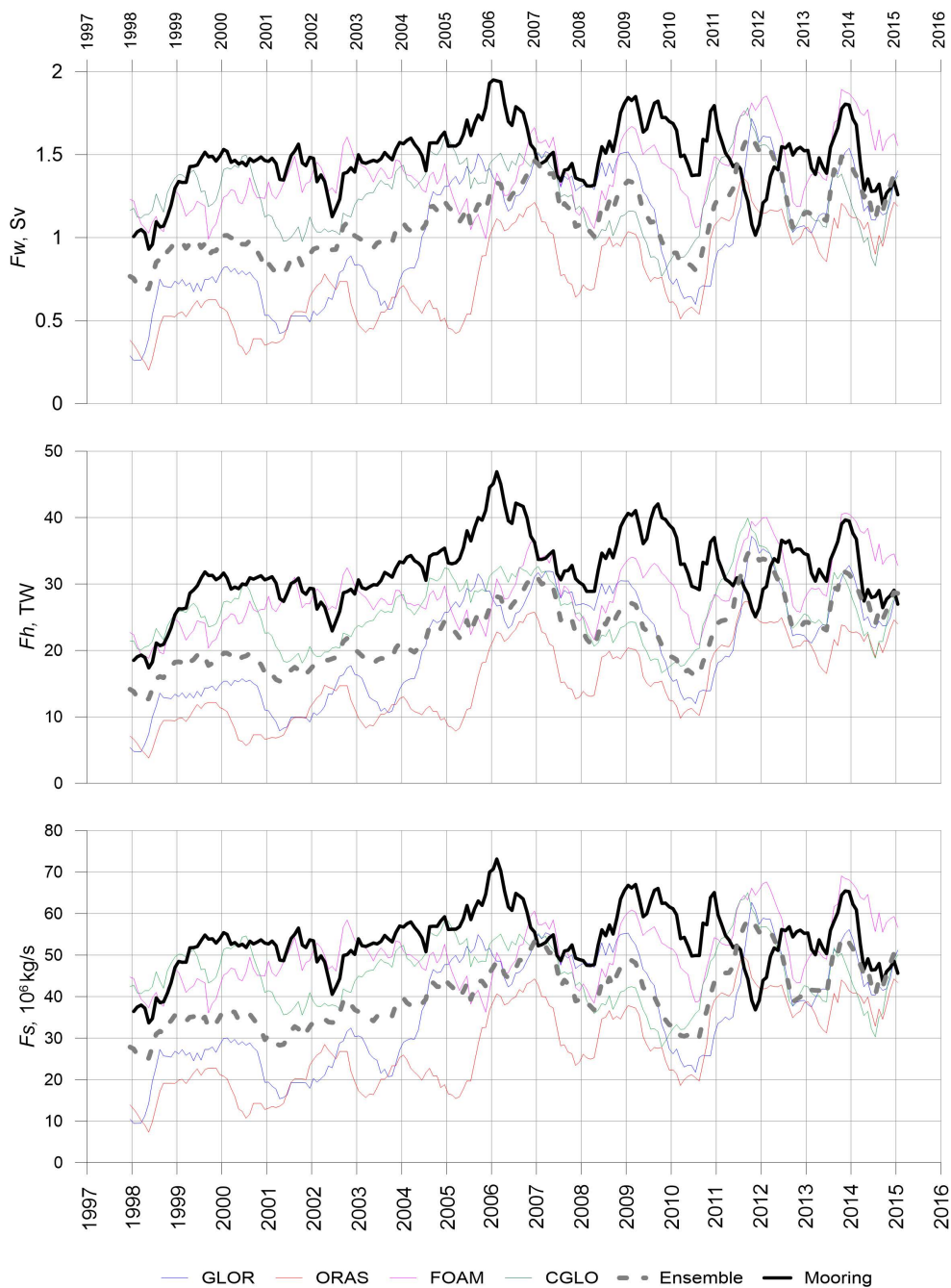


Fig. 9. Time series of heat and mass transport through the Fram Strait calculated by monthly average data for the Atlantic Ocean waters

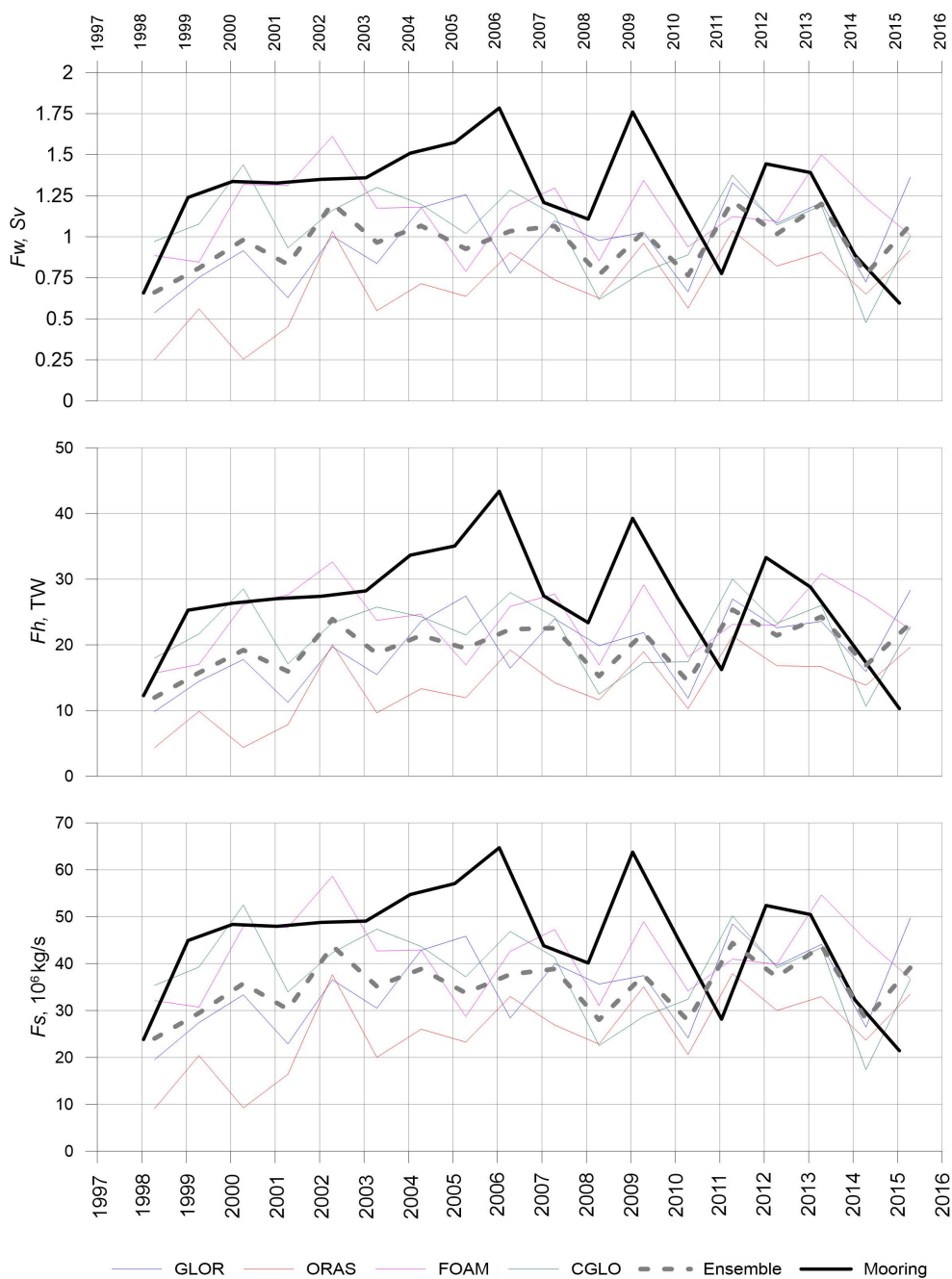


Fig. 10. Time series of heat and mass transport through the Fram Strait over summer season (April – September) for the Atlantic Ocean waters

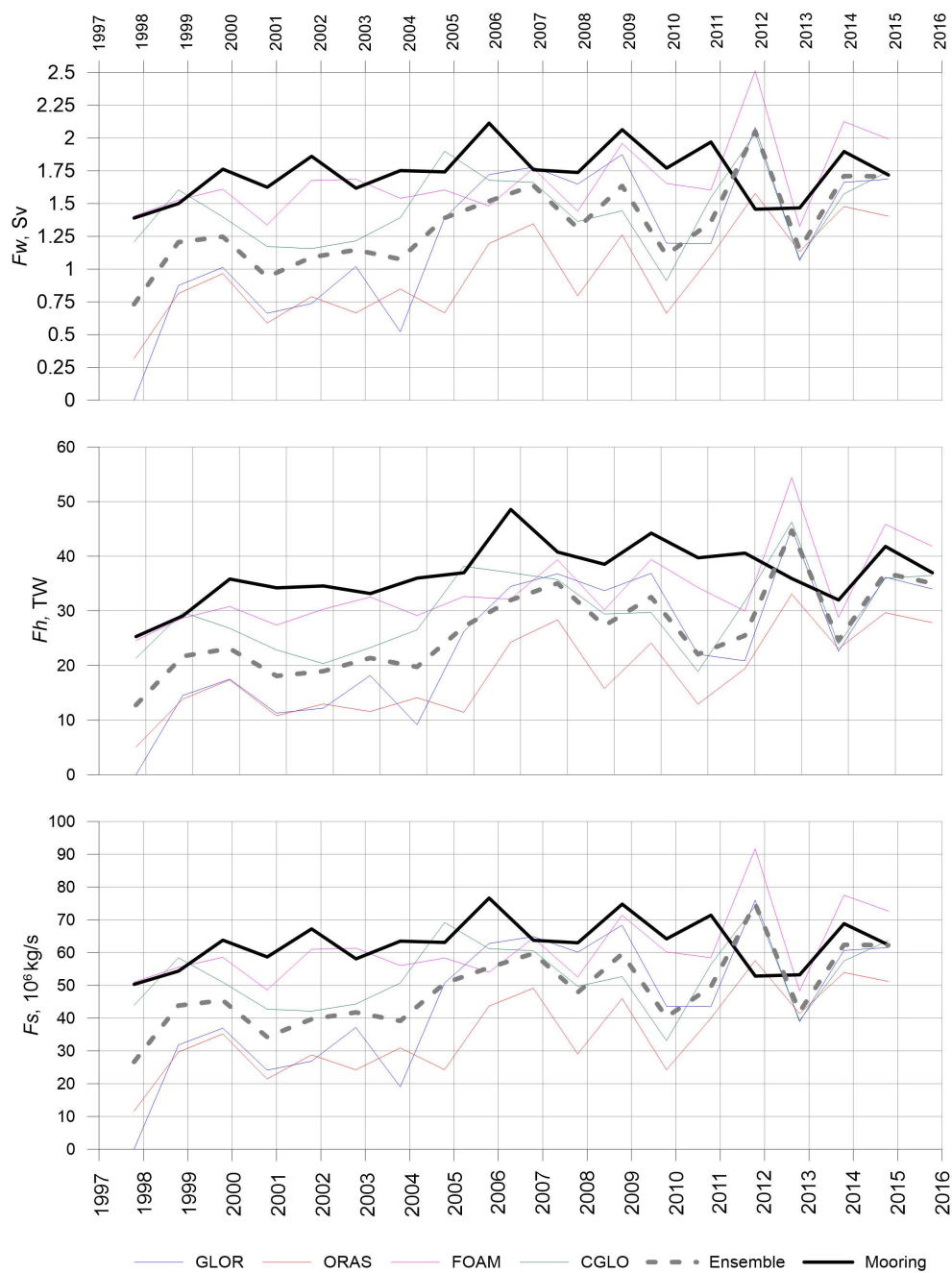


Fig. 11. Time series of heat and mass transport through the Fram Strait over winter season (October – March) for the Atlantic Ocean waters

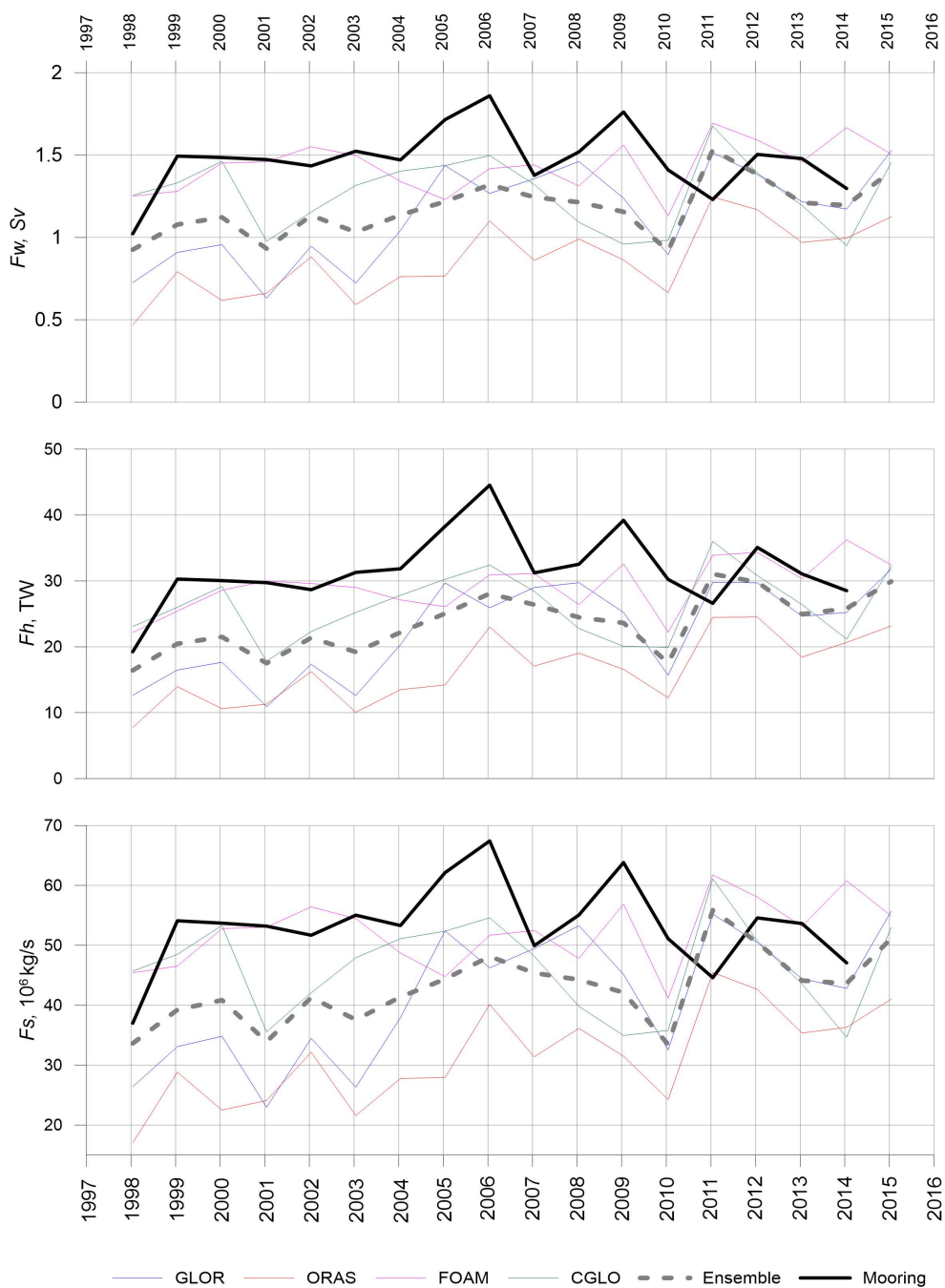


Fig. 12. Annual time series of heat and mass transport through the Fram Strait for the Atlantic Ocean waters

Conclusions

In the present paper, a comparative analysis of heat and mass transport processes in the Fram Strait, calculated from field observations (AWI and NPI moorings) and GLOR, ORAS, FOAM and CGLO reanalyses, was carried out. The mooring data were interpolated to regular grid points using ordinary kriging (6.5°W – 8°E, 25 m vertical).

Monthly data comparison showed that reanalyses generally underestimate volume, heat and salt transports by 30%. This may be due to both the shortcomings of spatial interpolation methods and the fact that the models do not accurately estimate recirculation waters.

Additional analysis of heat and mass transport processes associated with Atlantic waters ($T > 2^{\circ}\text{C}$) showed significantly better results. It is revealed that the ensemble of models describes observation data variability the best. Talking about individual products, preference is given to the FOAM and CGLO reanalyses describing most of the mooring temporal variability.

The data consistency in the winter period (October–March) is shown to be higher than that in the summer period (April–September). It can be related to reanalysis imperfections (counting ice melt) and the season, namely summer, when moorings are usually replaced, which can result in additional errors in combining time series.

REFERENCES

1. Ribal, A. and Young, I.R., 2019. 33 Years of Globally Calibrated Wave Height and Wind Speed Data Based on Altimeter Observations. *Scientific Data*, 6(1), 77. <https://doi.org/10.1038/s41597-019-0083-9>
2. Ribal, A. and Young, I.R., 2020. Calibration and Cross Validation of Global Ocean Wind Speed Based on Scatterometer Observations. *Journal of Atmospheric and Oceanic Technology*, 37(2), pp. 279-297. <https://doi.org/10.1175/JTECH-D-19-0119.1>
3. Levitus, S., Antonov, J.I., Boyer, T.P., Baranova, O.K., Garcia, H.E., Locarnini, R.A., Mishonov, A.V., Reagan, J.R., Seidov, D. [et al.], 2012. World Ocean Heat Content and Thermosteric Sea Level Change (0–2000 m), 1955-2010. *Geophysical Research Letters*, 39(10), L10603. <https://doi.org/10.1029/2012GL051106>
4. Lellouche, J.-M., Le Galloudec, O., Drévilion, M., Régnier, C., Greiner, E., Garric, G., Ferry, N., Desportes, C., Testut, C.-E., Bricaud, C. [et al.], 2013. Evaluation of Global Monitoring and Forecasting Systems at Mercator Océan. *Ocean Science*, 9(1), pp. 57-81. <https://doi.org/10.5194/os-9-57-2013>
5. Lellouche, J.-M., Greiner, E., Le Galloudec, O., Garric, G., Regnier, C., Drevillon, M., Benkiran, M., Testut, C.-E., Bourdalle-Badie, R. [et al.], 2018. Recent Updates to the Copernicus Marine Service Global Ocean Monitoring and Forecasting Real-Time 1/12° High-Resolution System. *Ocean Science*, 14(5), pp. 1093–1126. <https://doi.org/10.5194/os-14-1093-2018>
6. Blindheim, J. and Østerhus, S., 2005. The Nordic Seas, Main Oceanographic Features. In: H. Drange, T. Dokken, T. Furevik, R. Gerdes and W. Berger, eds., 2005. *The Nordic Seas: An Integrated Perspective*. Washington, D.C.: American Geophysical Union, pp. 11-37. <https://doi.org/10.1029/158GM03>
7. Timofeev, V.T., 1960. *Water Masses of the Arctic Basin*. Leningrad: Hydrometeoizdat, 191 p. (in Russian).
8. Polyakov, I.V., Alexeev, V.A., Bhatt, U.S., Polyakova, E.I. and Zhang, X., 2010. North Atlantic Warming: Patterns of Long-Term Trend and Multidecadal Variability. *Climate Dynamics*, 34(2-3), pp. 439-457. <https://doi.org/10.1007/s00382-008-0522-3>

9. Maslowski, W., Marble, D., Walczowski, W., Schauer, U., Clement, J.L. and Semtner, A.J., 2004. On Climatological Mass, Heat, and Salt Transports through the Barents Sea and Fram Strait from a Pan-Arctic Coupled Ice-Ocean Model Simulation. *Journal of Geophysical Research: Oceans*, 109(C3), C03032. <https://doi.org/10.1029/2001JC001039>
10. Schauer, U., Fahrbach, E., Osterhus, S. and Rohardt, G., 2004. Arctic Warming through the Fram Strait: Oceanic Heat Transport from 3 Years of Measurements. *Journal of Geophysical Research: Oceans*, 109(C6), C06026. <https://doi.org/10.1029/2003JC001823>
11. Beszczynska-Möller, A., Fahrbach, E., Schauer, U. and Hansen, E., 2012. Variability in Atlantic Water Temperature and Transport at the Entrance to the Arctic Ocean, 1997–2010. *ICES Journal of Marine Science*, 69(5), pp. 852–863. <https://doi.org/10.1093/icesjms/fss056>
12. Ivanov, V.V., 2002. Atlantic Waters in the Western Arctic. In: A. P. Lisitsyn, M. E. Vinogradov and E. A. Romankevich, eds., 2002. *Integrated Oceanographic Studies in the Arctic Ocean*. Moscow: Nauchniy Mir, pp. 76–91 (in Russian).
13. Aagaard, K., Coachman, L.K. and Carmack, E., 1981. On the Halocline of the Arctic Ocean. *Deep Sea Research Part A. Oceanographic Research Papers*, 28(6), pp. 529–545. [https://doi.org/10.1016/0198-0149\(81\)90115-1](https://doi.org/10.1016/0198-0149(81)90115-1)
14. Wood, K.R., Jayne, S.R., Mordy, C.W., Bond, N., Overland, J.E., Ladd, C., Stabeno, P.J., Ekholm, A.K., Robbins, P.E. [et al.], 2018. Results of the First Arctic Heat Open Science Experiment. *Bulletin of the American Meteorological Society*, 99(3), pp. 513–520. <https://doi.org/10.1175/BAMS-D-16-0323.1>
15. Carton, J.A., Penny, S.G. and Kalnay, E., 2019. Temperature and Salinity Variability in the SODA3, ECCO4r3, and ORAS5 Ocean Reanalyses, 1993–2015. *Journal of Climate*, 32(8), pp. 2277–2293. <https://doi.org/10.1175/JCLI-D-18-0605.1>
16. Janout, M.A., Hölemann, J., Laukert, G., Smirnov, A., Krumpen, T., Bauch, D. and Timokhov, L., 2020. On the Variability of Stratification in the Freshwater-Influenced Laptev Sea Region. *Frontiers in Marine Science*, 7, 543489. <https://doi.org/10.3389/fmars.2020.543489>
17. Fahrbach, E., Meincke, J., Østerhus, S., Rohardt, G., Schauer, U., Tverberg, V. and Verduin, J., 2001. Direct Measurements of Volume Transports through Fram Strait. *Polar Research*, 20(2), pp. 217–224. <https://doi.org/10.3402/polar.v20i2.6520>
18. Lellouche, J.-M., Le Galloudec, O., Drévilion, M., Régnier, C., Greiner, E., Garric, G., Ferry, N., Desportes, C., Testut, C.-E. [et al.], 2013. Evaluation of Global Monitoring and Forecasting Systems at Mercator Océan. *Ocean Science*, 9(1), pp. 57–81. <https://doi.org/10.5194/os-9-57-2013>
19. Wackernagel, H., 1995. Ordinary Kriging. In: H. Wackernagel, 1995. *Multivariate Geostatistics: An Introduction with Applications*. Berlin, Heidelberg: Springer, pp. 74–81. https://doi.org/10.1007/978-3-662-03098-1_11
20. Korablyev, A.A. Pnyushkov, A.V. and Smirnov, A.V., 2008. Technology of Compiling Oceanographic Databases: A Case Study of the Arctic North European Basin. *Proceedings of the Russian State Hydrometeorological University*, (1), pp. 89–108 (in Russian).
21. De Steur, L., Hansen, E., Mauritzen, C., Beszczynska-Möller, A. and Fahrbach, E., 2014. Impact of Recirculation on the East Greenland Current in Fram Strait: Results from Moored Current Meter Measurements between 1997 and 2009. *Deep Sea Research Part I: Oceanographic Research Papers*, 92, pp. 26–40. <https://doi.org/10.1016/j.dsr.2014.05.018>

About the authors:

Aleksandr V. Smirnov, Senior Researcher, Arctic and Antarctic Research Institute (38 Bering Str., Saint Petersburg, 199397, Russian Federation), **ResearcherID: J-5935-2014**, **ORCID ID: 0000-0003-3231-7283**, **Scopus Author ID: 56264603400**, avsmir@aari.ru

Vladimir V. Ivanov, Chief Researcher, M.V. Lomonosov Moscow State University (1 Leninskie Gory, Moscow, 119991, Russian Federation), Arctic and Antarctic Research Institute (38 Bering Str., Saint Petersburg, 199397, Russian Federation)

Andrey A. Sokolov, Leading Engineer, Ice Hydrometeorological Information Center, Arctic and Antarctic Research Institute (38 Bering Str., Saint Petersburg, 199397, Russian Federation)

Contribution of the co-authors:

Aleksandr V. Smirnov – data preparation and analysis, numerical calculations, analysis and interpretation of the results, discussion and graphical representation of the results

Vladimir V. Ivanov – formulation of the research problem, analysis and interpretation of the results obtained in the study, discussion of the work results, formulation of conclusions

Andrey A. Sokolov – statistical data analysis, graphical presentation of the results

The authors have read and approved the final manuscript.

The authors declare that they have no conflict of interest.

Original article

Spatial and Temporal Variability of a Latent Heat Flux in the Northwest Pacific Ocean Based on the ERA5 Reanalysis Data

G. V. Shevchenko^{1, 2, ✉}, D. M. Lozhkin¹

¹ Sakhalin Branch of the Russian Federal Research Institute of Fisheries and Oceanography,
Yuzhno-Sakhalinsk, Russian Federation

² Institute of Marine Geology and Geophysics, Far Eastern Branch of Russian Academy of Sciences,
Yuzhno-Sakhalinsk, Russian Federation
✉ Shevchenko_zhora@mail.ru

Abstract

Purpose. The paper is aimed at studying the spatial and temporal variability of a latent heat flux – one of the important components of heat balance in the Northwest Pacific Ocean and the Far Eastern seas based on the ERA5 reanalysis data.

Methods and results. The ERA5 reanalysis data on a latent heat flux in the area limited by the coordinates 42°–60°N and 135°–180°E and including the Far Eastern seas and the Northwest part of the Pacific Ocean constituted the material for the study. The array of monthly averages at a quarter-degree spatial resolution was analyzed using the standard statistical methods. The average long-term distributions of latent heat flux values for each month were constructed; the amplitudes and phases of annual and semi-annual cycles, and the linear trend coefficients were calculated in each spatial cell, and the decomposition was performed using the empirical orthogonal functions. The range of seasonal variations is significant in the zone of warm currents, and it decreases sharply in the northern part of the area under study in the Pacific Ocean as well as in the Okhotsk and Bering seas. The interannual variations are manifested in the quasi-cyclic changes of the envelope based on the maximum values with a period of about 6 years. The unidirectional trends in the interannual latent heat flux variations are weakly shown.

Conclusions. Among the seasonal variations of a latent heat flux, the annual cyclicity is predominant and most pronounced in the southern part of the Northwest Pacific Ocean (the area influenced by the warm Kuroshio Current) off the Japan Sea coast of the Honshu Island in the Tsushima Current zone. This is conditioned by a significant evaporation increase in these areas during a cold season that, in its turn, is related to a sharper temperature contrast as well as to the impact of a winter monsoon characterized by the strong and stable northwesterly winds bringing dry cold air from the continent. The latent heat flux values are positive in some areas of the studied area in a warm period that indicates the important role of water vapor condensation in the areas with high cloudiness and in the zones of quasi-stationary upwellings.

Keywords: heat balance, latent heat flux, annual cycle, linear trend, empirical orthogonal functions, Northwest Pacific Ocean

Acknowledgments: The study was carried out within the framework of state assignment of the FSBSI “VNIRO” on theme “Study of influence of variability of climatic and oceanological conditions on the main objects of Russian fisheries”.

For citation: Shevchenko, G.V. and Lozhkin, D.M., 2024. Spatial and Temporal Variability of a Latent Heat Flux in the Northwest Pacific Ocean Based on the ERA5 Reanalysis Data. *Physical Oceanography*, 31(3), pp. 387-397.

© 2024, G. V. Shevchenko, D. M. Lozhkin

© 2024, Physical Oceanography



Introduction

The Northwest Pacific Ocean and the Far Eastern seas represent an active fishing area of the Russian fishing companies in the Far Eastern region. A significant number of pelagic fish species, such as Pacific salmon, saury and Far Eastern sardine, are caught here. Most of these species are sensitive to the thermal conditions of their habitat. Changing climate conditions determine the importance of the study of various factors influencing the temperature of the surface water layer in these areas, including the spatial and temporal variability of the heat balance and its elements. One of the important components of this balance is the latent heat flux (LHF). Its data can be obtained on several web pages giving reanalysis materials of various hydrometeorological parameters.

Latent heat flux refers to its costs for phase transitions during the atmosphere and hydrosphere interaction – losses in the ocean during evaporation and melting of ice and intake during condensation and ice formation (heat flux from the atmosphere to the ocean is considered to be positive, and in the opposite direction – negative)¹. Moreover, the heat flux from the ocean during evaporation is considered one of the most important components of the heat balance. In addition to the evaporating surface temperature, this flux magnitude is significantly influenced by air temperature and humidity, as well as wind speed. Despite this parameter importance for climate research, spatial and temporal variability of latent heat flux in the Northwest Pacific Ocean is rarely considered as an independent characteristic. Important results were obtained in [1], although more attention was paid to the tropical regions (as in [2, 3], which indicates the special role of this zone in the interaction between the atmosphere and the ocean) and the northeastern part of the Pacific Ocean. In this regard, the study of sensible and latent heat fluxes in the northwestern part of the Sea of Japan during the cold season is specially noted [4]. The information basis for this study was the NCEP/NCAR reanalysis data which allow a detailed analysis of the spatial and temporal variability of the heat balance components. The present paper uses a different data source, namely the ERA5 reanalysis materials, available at <https://climate.copernicus.eu/climate-reanalysis>.

It is known that in the Northwest Pacific Ocean, in the zone of warm Kuroshio Current influence, one of the most energetically active regions of interaction between the atmosphere and the ocean is located, between which very intense heat exchange occurs across the interface [5]. The region under consideration also contains the Far Eastern seas, in which significant heat fluxes are caused by the ice cover formation and ice melting. Interannual variations of these fluxes associated with global warming processes are also of interest.

The present paper is aimed at studying the spatial and temporal variability of the latent heat flux, one of the important components of heat balance in the Northwest Pacific Ocean and the Far Eastern seas, based on the ERA5 reanalysis data for 1998–2022.

¹ Budyko, M.I., 1956. *The Heat Balance of the Earth's Surface*. Leningrad: Gidrometeoizdat, 256 p. (in Russian).

Materials and methods

The ERA5 reanalysis data were taken as the materials for the research on the latent heat flux over the Northwest Pacific Ocean and the Far Eastern seas for 1998–2022. All fluxes of this product are calculated using the corresponding ECWMF model described at <https://www.ecmwf.int/en/publications/ifs-documentation>.

As noted above, this flux (LHF) reflects the heat exchange associated with phase transitions of water in the surface layer (evaporation, ice formation and melting). The data are given in joules per square meter which means the amount of flux per month through a cell with an area of 1 m². The area under study was limited to coordinates 35°–70°N, 130°–180°E, the spatial resolution of the data was 1/4°, the time resolution was 1 month. The main attention at this stage of the work was focused on the spatial and temporal variability features of the heat balance – determining factor in the formation of thermal conditions in the surface layer of the ocean.

The average long-term values of this parameter reflecting seasonal changes in the latent heat flux are calculated for every month in each spatial cell. To determine the quantitative characteristics of seasonal variations, the amplitudes and phases of annual and semi-annual cycles using the least squares method (LSM) were found. Linear trend parameters were determined using LSM (for each month and each season) in each cell. The method of empirical orthogonal function (EOF) decomposition was also used to study the sequence of LHF time layers; this type of statistical analysis permits simultaneous study of the main features of both seasonal and interannual variations. The interannual variability of the studied parameter is expressed mainly (in addition to unidirectional trends) in the low-frequency modulation of the annual cycle which makes the main contribution to the time functions of the two main modes of the EOF expansion.

Results and discussion

Averaged LHF distributions by season. Fig. 1 shows the average long-term spatial distributions of LHF for different seasons. February was chosen to characterize winter conditions, May – spring, August – summer and November – autumn.

In winter (the distributions of the studied parameter in January and March are identical to those presented in the figure with a slight decrease in its values in absolute value), LHF values are negative throughout the region and have the largest absolute values on the southern boundary between the 140th and 150th meridians, where the warm Kuroshio Current departs from the coast of Honshu and acquires its eastern direction (about –25 MJ/m²). In general, intense latent heat flux is characteristic of the zone between parallels 35° and 40°N both in the Northwest Pacific Ocean and in the Sea of Japan, in the zone of influence of the warm Tsushima Current, although in the latter case to a lesser extent.

LHF values fluctuate within rather narrow limits from –6 to –10 MJ/m² over most of the region under study. The lowest flux values (from 0 to –2 MJ/m²) are in the frozen waters of the northwestern and western parts of the Sea of Okhotsk and in the northern part of the Tatar Strait (the Sea of Japan). This is typical not only for February, when the ice cover reaches its maximum development and prevents heat exchange between the atmosphere and the ocean, but also for December, when high flow intensity could be expected.

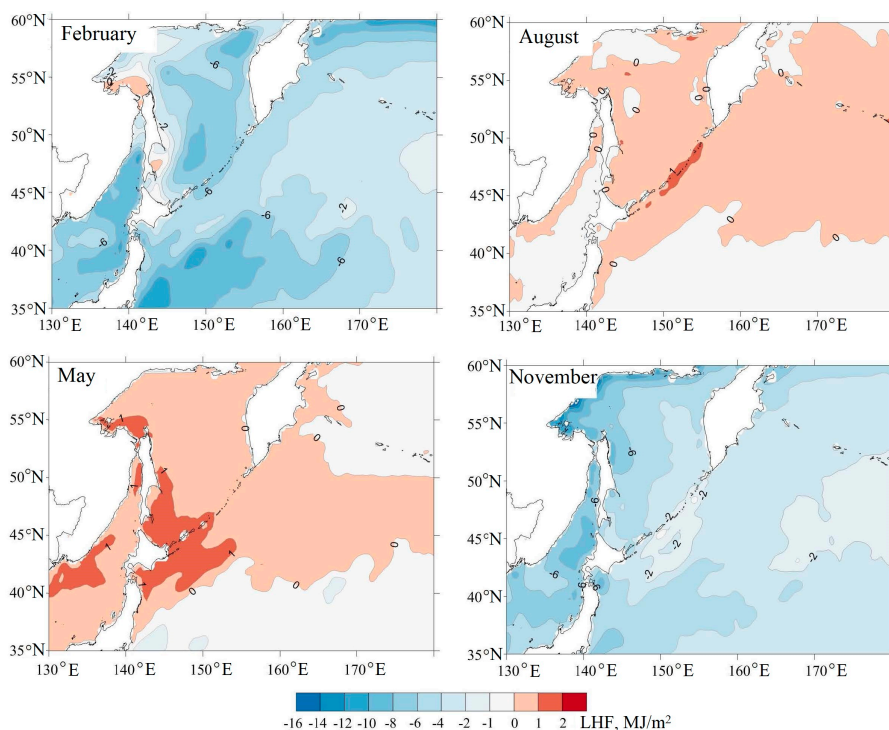


Fig. 1. Average long-term spatial distributions of LHF in the region under study

Latent heat flux values decrease primarily in the southern part of the Northwest Pacific Ocean (they change slightly in the main part of the region) in spring. LHF becomes positive in the southwestern part of the Sea of Okhotsk and in the Northwest Pacific Ocean area adjacent to Hokkaido and the South Kuril Islands in May, although it has a small value from 0.05 to 0.2 MJ/m². This can be determined by moisture condensation in areas with traditionally high clouds.

The area with positive LHF values expands in June; it covers large areas in the area of the Kuril Island Ridge, as well as in the northern and western parts of the Sea of Okhotsk. Areas with positive values (up to 0.5 MJ/m²) reach their maximum sizes in the Sea of Okhotsk and in a wide band (42°–50°N) stretching east from the Kuril Ridge to the Aleutian Islands in July. The latent heat flux intensity decreases to its minimum values for the year (about –6 MJ/m²) at the southern boundary. Areas with positive values narrow noticeably in August; they are noted mainly in the area of quasi-stationary upwellings in the central part of the Kuril Ridge, Kashevarov Bank, the Yam Islands, etc. Positive values are noted only in a small area in the Middle Kuril region in September.

In autumn, the LHF spatial distribution is similar to winter; the only values that are absent are those close to zero noted above in frozen areas. The maximum absolute values were noted on the southern boundary of the studied region and they increased from October to December and exceeded 30 MJ/m².

It is important to emphasize that the highest LHF values were found in autumn and winter in areas with the highest sea surface temperatures (SST), in the zone of influence of the warm Kuroshio and Tsushima Currents, associated with an increase in the temperature contrast between the atmosphere and the ocean surface in the cold season (the similar effect was also noted in the western part of the Barents Sea, in the zone of influence of the warm Gulf Stream [6]). This is largely determined by the effect of the winter monsoon characterized by high wind speeds carrying drier and colder air from the mainland than the summer monsoon brings from the central regions of the Pacific Ocean. The results obtained are consistent with the conclusions of [5, 7] in which the area east of Honshu is noted as one of the most energetically active areas of the atmosphere and ocean. Positive values of the parameter in areas of quasi-stationary upwelling also have a simple physical explanation, since moisture condensation can appear in them due to the lower temperature of the ocean surface.

Harmonic analysis of seasonal variations. Figure 2 shows the spatial distributions of the amplitude and phase of the annual and semi-annual cycles. Annual cycle amplitude usually characterizes the scale of seasonal variations as it takes high values in areas where these variations are most intense and is minimal where the annual cycle is weakly expressed. The figure shows seasonal fluctuations in latent heat flux with pronounced latitudinal variability: they are maximum near the eastern coast of Honshu and minimum in the northern part of the area under study, in the Bering Sea and on the northern shelf of the Sea of Okhotsk. The nature of the spatial variability of the amplitude in the Sea of Japan is somewhat different as the maximum values are noted off the Honshu western coast, in the zone of warm Tsushima Current influence, and the minimum are noted off the Primorye coast. High values of the amplitude of the annual cycle in the zone of influence of the warm Kuroshio and Tsushima Currents show a significant decrease in evaporation in these areas during the summer monsoon characterized by lower wind speeds and higher air humidity compared to the winter monsoon. These differences are not so noticeable in the average long-term LHF distributions for different seasons.

The phase of the annual cycle in the main part of the study area (the Northwest Pacific Ocean, the Bering Sea and the eastern part of the Sea of Okhotsk) fluctuates within $150\text{--}160^\circ$ (1 month accounts for 30° , so the obtained value corresponds to the maximum in July), its values decrease to $130\text{--}140^\circ$ in the Sea of Japan and in the western Sea of Okhotsk and up to $110\text{--}120^\circ$ in the northern part of the Tatar Strait and north of the Sakhalin Island.

Noticeable amplitudes of the semi-annual component were noted in areas with a complex annual cycle which is not well described by the annual cycle. Such areas include the northwestern part of the Sea of Okhotsk, coastal zones off the coast of the Sakhalin, Hokkaido and Honshu Islands (from the eastern side).

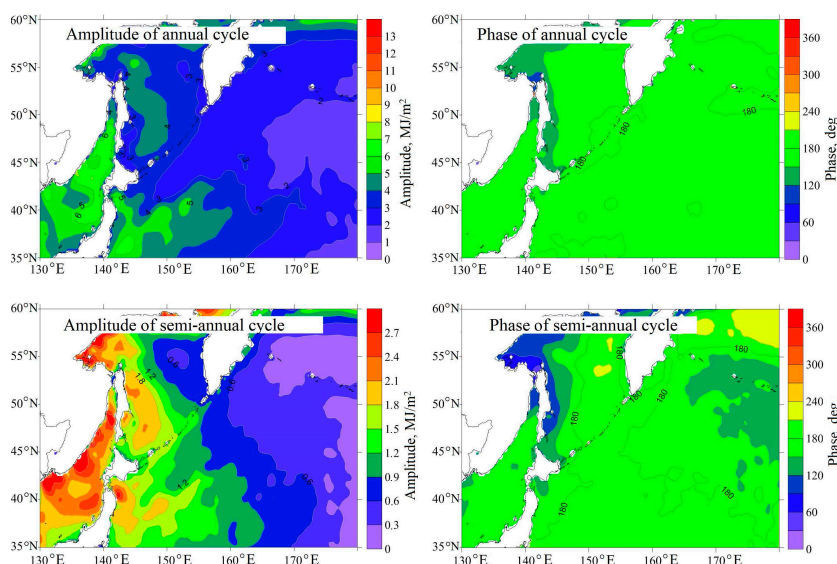


Fig. 2. Spatial distribution of amplitudes and phases of the annual and semi-annual LHF cycles

Linear trend coefficients. Much attention is usually paid to identifying unidirectional trends when studying hydrometeorological parameters under global climate change. In this regard, such an analysis was also carried out for the latent heat flux in the Northwest Pacific Ocean and the Far Eastern seas (Fig. 3). A weakly expressed tendency towards an increase in latent heat flux was noted in the Bering Sea, the northern and northeastern parts of the Northwest Pacific Ocean and in the eastern part of the Okhotsk Sea in winter and spring. The same weak tendency towards its decrease was observed in the Pacific Ocean south of the 45°N parallel, in the northern part of the Sea of Okhotsk and the Sea of Japan. Minor negative trends in most of the area under study were observed in summer. The most intense interannual changes were detected in autumn. Significant negative trends were found in the area of the Sangar Strait and in general off the coast of Japan, positive ones – in the Amur Estuary, near the Shantar Islands and in the Pacific Ocean along the southern boundary of the region under study. In general, relatively weak unidirectional trends in changes in LHF in the Far Eastern seas and the Northwest Pacific Ocean can be observed. It indicates an insignificant impact of global warming on interannual changes in the latent heat flux in this region. This is consistent with the low values of the linear trend coefficients in variations in ocean surface temperature in the studied region (with multidirectional trends in the Sea of Okhotsk and the Bering Sea) and surface atmospheric pressure which indicates relatively weak changes in the atmospheric air circulation ².

² Lozhkin, D.M., 2022. *Spatiotemporal Variability of Surface Temperature of the Sea of Okhotsk and Adjacent Waters According to Satellite Observations and ERA5 Reanalysis*. Thesis Cand. Phys.-Math. Sci. Yuzhno-Sakhalinsk: SakhNIRO, 159 p. (in Russian).

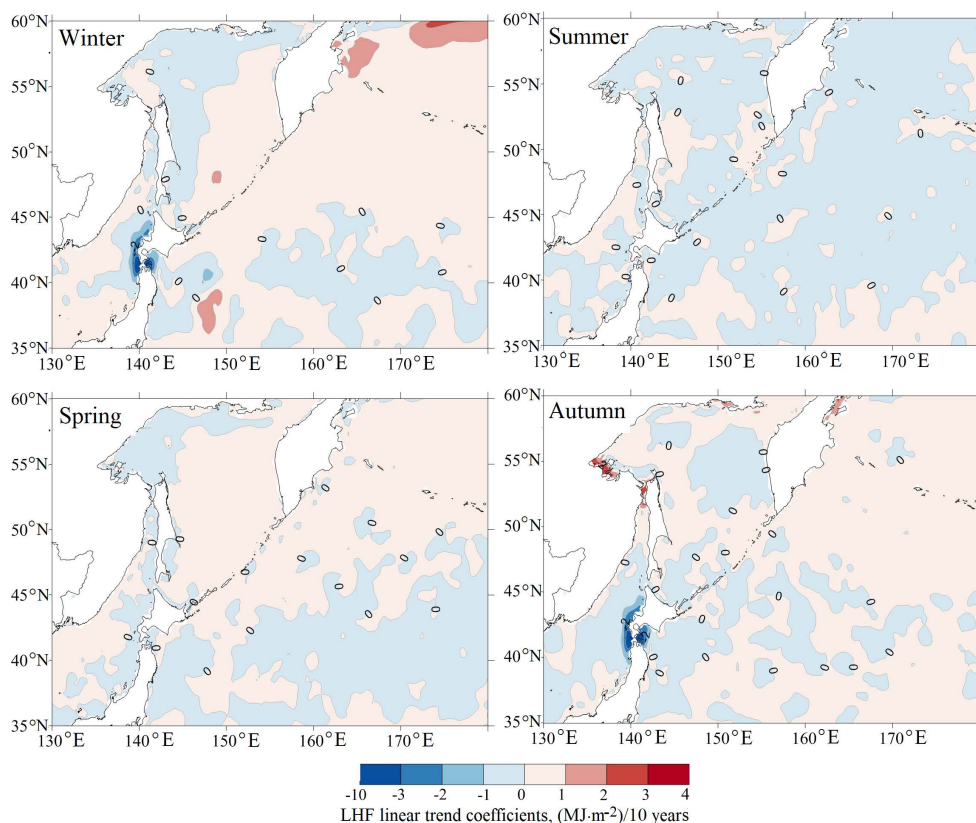


Fig. 3. Spatial distributions of the *LHF* linear trend coefficients in different seasons of a year

Decomposition of LHF in terms of EOF. The EOF decomposition method is often used for a detailed study of the spatial and temporal variability of hydrometeorological fields [8]. Fig. 4 shows the spatial functions of the first two modes of decomposition of the sequence of the LHF time layers using this method. The first mode is the main one accounting for 94.5% of the total variance of the parameter. Its spatial distribution (all values are negative, assumed to be dimensionless) is quite simple; values of ~ -5 are noted in vast areas of the northeastern part of the Northwest Pacific Ocean, in the Bering Sea, in the eastern and central parts of the Sea of Okhotsk. In the north-west of the latter, the smallest absolute values from -2 to -3 were identified and the highest ones were noted in the Sea of Japan off the western coast of Japan (from -10 to -12) and in the south of the considered part of the Northwest Pacific Ocean (up to -20 at Honshu eastern coast).

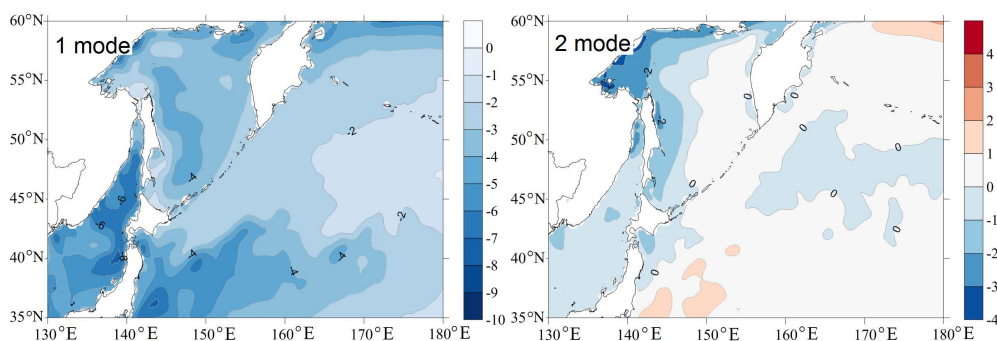


Fig. 4. Spatial distribution of the first two modes of decomposition of a sequence of the *LHF* time layers using EOF (dimensionless)

The time function of the main mode (Fig. 5) has a pronounced annual variation with maximum values in December and January (a little more and a little less than 1.5 MJ/m^2) and minimum values in July and June (about 0.2 MJ/m^2). It is well described by the annual cycle with an amplitude of 0.7 MJ/m^2 and a phase of 334° which corresponds to the above noted maximum in December. It is characterized by low-frequency modulation, most pronounced for winter maxima, with a period of about 6 years. The highest function values in December 2020 (1.84 MJ/m^2) and 2005 (1.79 MJ/m^2) stand out noticeably.

In general, the spatial distribution and temporal function of this mode reveal the most general patterns of the *LHF* distribution: the presence of areas with the most intense evaporation in the cold season in the zones of influence of the warm Kuroshio and Tsushima Currents and low *LHF* values in the northern part of the region under study including in frozen areas.

The distribution of the spatial function of the second mode (it accounts for 1.4% of the *LHF* dispersion) is significantly more complex. It characterizes the parameter variations that are not in phase, which are described by the first mode discussed above. Therefore, it has a nodal line dividing zones with the opposite sign. The area with positive values occupies part of the Northwest Pacific Ocean south of the 45°N parallel with maxima near the Honshu eastern coast (~ 2). Positive values of the function were also revealed in the eastern part of the considered area of the Bering Sea and in a narrow strip near the Middle Kuril Islands. In the rest of the Northwest Pacific Ocean (north of the 45°N parallel) and in the waters of the Far Eastern seas, the spatial function is negative, the maximum absolute values are noted in the western part of the Sea of Okhotsk and in the Sea of Japan (from -1 to -2), extreme values are found in a small area off the Hokkaido southern coast (~ -3).

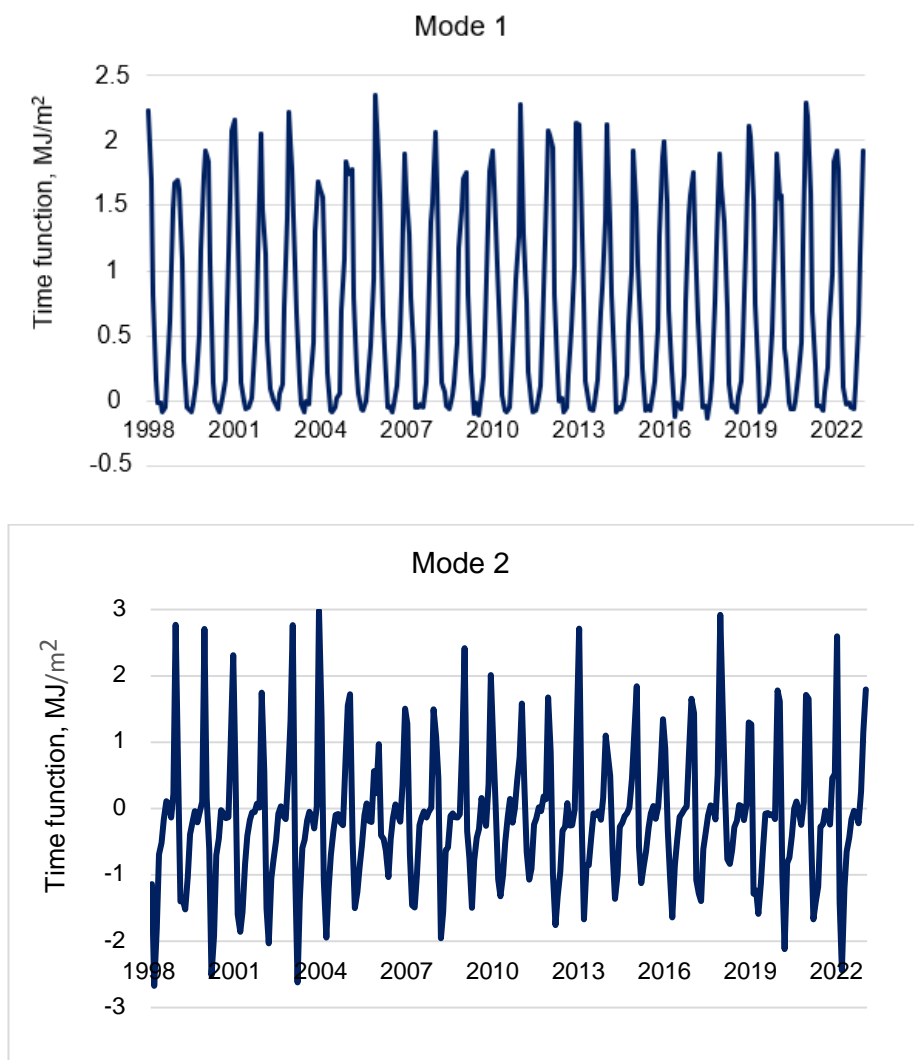


Fig. 5. Variations in time functions of the first (*top*) and second (*bottom*) modes of decomposition of a sequence of the *LHF* time layers using EOF

The time function of this mode is described by a combination of annual and semi-annual cycles with amplitudes of about 1 and 0.4 MJ/m². The average annual variation of this function is characterized by maximum values in November (1.3 MJ/m²) and October (1.1 MJ/m²) and minimum values in April and May (−1.1 MJ/m²). This means that in autumn the second mode provides a positive correction to the main component in the southern part of the region under study and a negative correction in the northern and especially in its northwestern sections. In spring, the contribution of this opposite nature mode is observed. The interannual variability of the time function of the second mode is more significant compared to the first one and is not regular.

Conclusion

The analysis of an array of average monthly LHF values for 1998–2022 showed the following characteristics of the spatial and temporal variability of this parameter.

The LHF values are universally negative and reach their highest absolute values in the zone of influence of the warm Kuroshio and Tsushima Currents in the cold season (autumn and winter). This is determined by the influence of the winter monsoon characterized by stable and strong winds from the northwest and close to it carrying cold dry air from the mainland. The latent heat flux is insignificant in the northern part of the study area, including in frozen areas.

During the warm period in zones of warm currents, the LHF values decrease significantly in absolute value, which is probably determined by the summer monsoon winds, which are characterized by relatively low speeds and high humidity of the air flow. At the same time, the latent heat flux is positive in a number of areas, although small in magnitude. This indicates the important role of condensation in areas of high cloudiness and in zones of quasi-stationary upwelling.

Calculation of the annual cycle amplitudes showed the greatest range of seasonal variations in the zone of warm currents and its sharp decrease in the northern part of the Northwest Pacific Ocean and the Sea of Okhotsk, as well as in the Bering Sea. This component with an amplitude of 0.7 MJ/m^2 and with high values in December and January (about 1.5 MJ/m^2) and minimum values in July and June (0.2 MJ/m^2) plays a major role in variations in the time function of the EOF main mode. Interannual variations are expressed in quasi-cyclic changes in the envelope along maximum values with a period of about 6 years. Unidirectional trends in interannual LHF variations are weakly expressed.

The results obtained can be used to study the variability of thermal conditions in the surface layer of the Northwest Pacific Ocean and the Far Eastern seas to improve forecasts of the timing and conditions of feeding and spawning migrations of Pacific salmon, as well as other species of pelagic fish.

REFERENCES

1. Ponomarev, V.I., Petrova, V.A. and Dmitrieva, E.V., 2012. Climatic Variability of the Heat Balance Components at the Sea Surface in the North Pacific. *Izvestiya TINRO*, 169, pp. 67-76 (in Russian).
2. Ayina, L.-H., Bentamy, A., Mestas-Nuñez, A.M. and Madec, G., 2006. The Impact of Satellite Winds and Latent Heat Fluxes in a Numerical Simulation of the Tropical Pacific Ocean. *Journal of Climate*, 19(22), pp. 5889-5902. <https://doi.org/10.1175/JCLI3939.1>
3. Wang, Yu and Wu, R., 2021. Factors of Boreal Summer Latent Heat Flux Variations over the Tropical Western North Pacific. *Climate Dynamics*, 57(9–10), pp. 2753-2765. <https://doi.org/10.1007/s00382-021-05835-4>
4. Pichugin, M.I. and Ponomarev, V.I., 2013. Variability of Sensible and Latent Heat Fluxes over the Northwest Part of the Sea of Japan in Cold Season. *Vestnik of Far Eastern Branch of Russian Academy of Sciences*, (6), pp. 22-29 (in Russian).
5. Lappo, S.S., Gulev, S.K. and Rozdestvensky, A.E., 1990. *Large-Scale Heat Interaction in the Ocean-Atmosphere System and Energetically Active Zones of the World Ocean*. Leningrad: Gidrometeoizdat, 336 p. (in Russian).
6. Surkova, G.V. and Romanenko, V.A., 2021. Seasonal and Long-Term Changes of Turbulent Heat Fluxes between Sea and Atmosphere in Western Sector of the Russian Arctic. *Vestnik Moskovskogo Universiteta. Seria 5, Geografia*, (4), pp. 74-82 (in Russian).

7. Vlasova, G.A. and Polyakova, A.M., 2013. Energy-Active Zone of the Ocean and Atmosphere in Nw Pacific. *Izvestia: Herzen University Journal of Humanities & Sciences*, 163, pp. 128-140 (in Russian).
8. Bagrov, N.A., 1959. [Analytical Representation of Meteorological Field Series by Natural Orthogonal Components]. *Trudy TsIP* [Transactions of the Central Institute of Forecasts], 74, pp. 3-24 (in Russian).

About the authors:

Georgiy V. Shevchenko, Head of the Oceanography Laboratory, Sakhalin Branch of the All-Russian Research Institute of Fisheries and Oceanography (VNIRO) (196 Komsomolskaya Str., Yuzhno-Sakhalinsk, 693023, Russian Federation), Leading Researcher, Institute of Marine Geology and Geophysics, Far Eastern Branch of the Russian Academy of Sciences (1B Nauki Str., Yuzhno-Sakhalinsk, 693023, Russian Federation), DSc (Phys.-Math.), **ORCID ID: 0000-0003-0785-4618**, shevchenko_zhora@mail.ru

Dmitry M. Lozhkin, Leading Researcher, Sakhalin Branch of the All-Russian Research Institute of Fisheries and Oceanography (VNIRO) (196 Komsomolskaya Str., Yuzhno-Sakhalinsk, 693023, Russian Federation), CSc (Phys.-Math.), **ORCID ID: 0000-0002-7073-681X**

Contribution of the co-authors:

Georgiy V. Shevchenko – analyzing and summarizing the research results, paper preparation

Dmitry M. Lozhkin – processing and complex data analysis, construction of graphs and distributions, discussion of work results


The authors have read and approved the final manuscript.

The authors declare that they have no conflict of interest.

Dynamics of Nutrients Concentration in the Chernaya River Waters (Crimean Peninsula) in 2015–2020

M. A. Myslina , A. V. Varenik, D. V. Tarasevich

Marine Hydrophysical Institute of RAS, Sevastopol, Russian Federation

 myslina@mhi-ras.ru

Abstract

Purpose. The study is purposed at assessing the intra- and inter-annual dynamics of nutrients concentration (compounds of inorganic nitrogen, phosphorus and silicon) in the Chernaya River waters. **Methods and Results.** The quarterly monitoring data on the water hydrochemical characteristics in the lower reaches of the Chernaya River and in the Chernorechenskoe reservoir obtained by Marine Hydrophysical Institute of RAS in 2015–2020 were used. The data obtained made it possible to study the distribution of inorganic nitrogen, phosphorus and silicon compound concentrations in the Chernaya River waters during the period under study, as well as its seasonal and interannual changes. As compared to 2010–2014, the ammonia nitrogen levels in 2015–2020 increased on average by 2.7 times. The mean long-term inorganic nitrogen outflow with the Chernaya River waters was 32.46 t/year in 2010–2014 and 27.8 t/year in 2015–2020, phosphorus and silicon – 0.23 and 57.93 t/year in 2010–2014 and 0.18 and 62.21 t/year in 2015–2020, respectively.

Conclusions. An increase in concentrations of all the nutrients under consideration was observed at the stations located near the villages in the Baydar Valley and hence, most susceptible to the anthropogenic impact, as well as in the area of water outlet of the *Sevagrosoyuz* agricultural firm, that can testify to the inflow of mineral fertilizers to the river waters. Recently the content of nutrients inorganic forms in the Chernaya River waters has increased as compared to the period before 2014, indicating the discussed over the past decade necessity in constructing a sewerage and wastewater treatment system both for the enterprises and the residential development of the Baydar Valley.

Keywords: Chernaya River, Crimean Peninsula, nutrients, inorganic nitrogen, phosphorus, silicon, anthropogenic pressure

Acknowledgements: The study was carried out within the framework of state assignment of FSBSI FRC MHI on theme FNNN 2024-0001 “Fundamental studies of the processes determining the flows of matter and energy in marine environment and at its boundaries, the state and evolution of physical and biogeochemical structure of marine systems in modern conditions”.

For citation: Myslina, M.A., Varenik, A.V. and Tarasevich, D.V., 2024. Dynamics of Nutrients Concentration in the Chernaya River Waters (Crimean Peninsula) in 2015–2020. *Physical Oceanography*, 31(3), pp. 398-408.

© 2024, M. A. Myslina, A. V. Varenik, D. V. Tarasevich

© 2024, Physical Oceanography

Introduction

The Chernaya River is one of the main rivers of the Sevastopol region, the second deepest on the Crimean Peninsula that, unlike other rivers, almost never dries up. Its length is 41 km, the catchment area is 436 km and the average monthly discharge is 1.82–1.94 m³/s [1]. The river originates from the Skelsky spring, near Rodnikovoe (Rodnikovskoe) village. The Chernaya River belongs to the river type with a flood regime. As many as 11 tributaries flow into it ¹. The Chernaya River is

¹ Government of Sevastopol. [Annual Report on the State and Protection of the Environment of the Federal City of Sevastopol for 2015]. [online] Available at: https://sev.gov.ru/files/iblock/a38/gosdoklad_Sev_2015.pdf [Accessed: 16 May 2024] (in Russian).



not only the main surface source of water supply of Sevastopol, but also the only permanent watercourse that discharges its waters into Sevastopol Bay [2, 3].

Intra-annual distribution of the Chernaya River runoff is determined by the nature of the river alimentation and climatic conditions. In Crimean rivers, floods occur mainly in the winter-spring period, from November – December to April, which is associated with the passage of Mediterranean cyclones. The minimum runoff is observed in August – September due to a decrease in the amount or a complete absence of precipitation and depletion of underground runoff [4].

It is known that an increase in the river runoff pollution level can lead to an increase in the concentration and accumulation of nutrients and pollutants in the river estuaries, as well as in the adjacent coastal zone of the sea [5]. In general, the distribution of average nutrient content along river beds reflects the impact of natural and anthropogenic factors on the formation of chemical composition of river waters [6]. The average level of inorganic nitrogen and phosphorus compounds in the rivers flowing near populated areas can be significantly higher than the content of these compounds in large and small rivers, whose runoff is formed under natural conditions. Quite high concentrations of nitrogen and phosphorus inorganic compounds are also observed in the rivers with heavily swamped catchment areas [6].

The work [2] identifies several main factors affecting the pollution level of the Chernaya River: pollution of the river catchment area and its tributaries, high water turbidity during floods, as well as water pollution of the Chernorechenskoe reservoir. The authors of this work suggest that the pollution sources are anthropogenic in nature due to the presence of ponds in the Chernaya River catchment area, which are used not only as water runoff regulators, but also as wastewater storage ponds ².

The greatest anthropogenic impact on the Chernaya River is exerted by the Sevastopol agglomeration with a population density of ~ 5,000 people per 1 km² (as of 2013). At the same time, since 2014, the population of the region has almost doubled, which has caused an increase in the share of untreated wastewater discharge in the total volume of wastewater by 8% in the last five years [7]. River pollution occurs as a result of the flow of drainage water from agricultural fields and household plots, discharges of domestic wastewater through the networks of *Sevgorvodokanal* utility company and unorganized discharges, as well as storm water runoff [8, 9]. In work [10], E.I. Ovsyany and co-authors noted that the Chernaya River water pollution in the middle reaches occurred as a result of the discharge of untreated wastewater from Orlinoe village into the Baydarka River and also due to the lack of sewerage in the nearest settlements. In the area of Sakharnaya Golovka village (the lower reaches of the river), conditionally pure wastewater was periodically discharged, which led to contamination of underground aquifers and entry of pollutants into the river with surface-slope runoff [10].

Based on the foregoing, the study of the nutrients content in the Chernaya River waters, its intra- and interannual variation is relevant from the point of view of assessing the ecological and recreational potential of both the river itself and

² Lisovsky, A.A., ed., 2011. [*Surface Water Bodies of Crimea. Management and Use of Water Resources: Reference Book*]. Simferopol: KRP Publishing House “Krymchpedgis”, 242 p. (in Russian).

Sevastopol Bay. This work is purposed at studying the intra- and interannual dynamics of nutrients concentration in the Chernaya River waters.

Methods and materials

Sampling area. During the monitoring of pollution state of the Chernaya River and Chernorechenskoe reservoir waters from 2010 to 2014, 551 samples were taken; from 2015 to 2020 – 787 samples of river water were taken to determine the content of inorganic nitrogen, inorganic phosphorus and silicon compounds in them. Expeditionary work was carried out quarterly and was part of the state assignment of Marine Hydrophysical Institute (MHI) of RAS (Fig. 1).

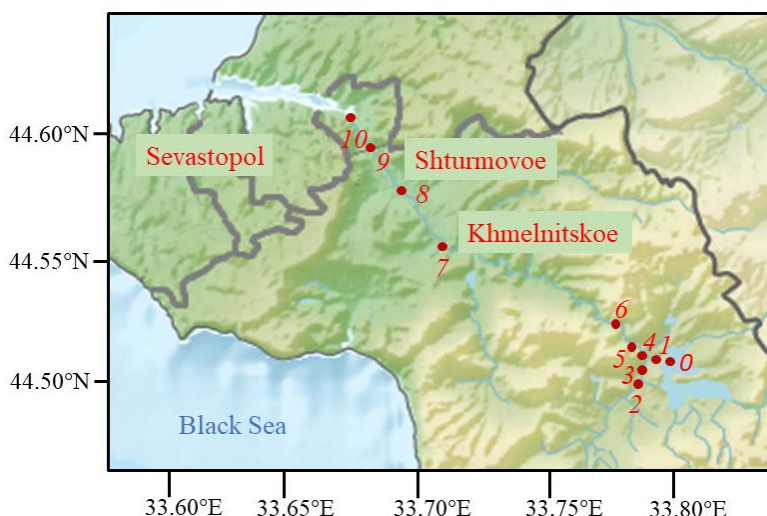


Fig. 1. Location of long-term monitoring stations of the Chernaya River: station 0 – reservoir mirror above the water intake; station 1 – water intake under the reservoir; station 2 – the Baydarka River, former pond; station 3 – culvert under the road in Ozernoe village; station 4 – the Urkusta River (tributary from the pond in Peredovoye village); station 5 – automobile bridge between Ozernoye and Peredovoye villages; station 6 – gauging station at Red Rock; station 7 – gauging station by Khmel'nitskoe village; station 8 – automobile bridge by Shturmovoe village; station 9 – railway bridge near Inkerman; station 10 – automobile bridge near Inkerman

To assess changes in the degree of anthropogenic impact on the dynamics of the nutrients content in the Chernaya River waters we also considered 2010–2014 period, i.e., before active development of the Baydar Valley land.

Methods of chemical analysis. Concentration of the sum of nitrates and nitrites was determined by the spectrophotometric method (RD 52.10.243-92) on an automatic flow multichannel analyzer of nutrients *Scalar San⁺⁺* (Netherlands). The method is based on the reduction of nitrates to nitrites through a copper-plated cadmium reducer. At the minimum detectable concentration of the sum of nitrates and nitrites of 0.36 $\mu\text{mol/l}$, the error is $\pm 0.20 \mu\text{mol/l}$. The content of ammonium ions was determined by the modified spectrophotometric method of Saggi – Solorzano [11] based on the phenol-hypochlorite reaction with the formation of indophenol in

the concentration range of 0.1–15.0 $\mu\text{mol/l}$ with an error σ equal to $\pm 12\%$. The phosphorus concentration was determined by a spectrophotometric method based on the formation of a blue phosphomolybdenum complex with a concentration measurement range of 0.05–100.0 $\mu\text{mol/l}$; the maximum error of the method is $\pm 15\%$ (RD 52.10.243-92). The silicon concentration was determined by the spectrophotometric method (RD 52.10.243-92) based on the formation of a blue silicomolybdenum complex with a range of determined concentrations of 0.05–80.0 $\mu\text{mol/l}$. The error of the method ranges from 3 to 20%.

Results

The main nitrogen forms during the study period were ammonium (NH_4^+) and nitrate (NO_3^-) nitrogen. Their contribution to the total content of inorganic nitrogen compounds in the Chernaya River waters was 9.97 and 87.51%, respectively. Nitrites, as an intermediate element in the ammonium oxidation to nitrates, were found in much lower concentrations, so the work considers the concentration of the sum of nitrates and nitrites (oxidized nitrogen, $\text{NO}_2^- + \text{NO}_3^-$). Some statistical characteristics of the determined elements concentrations are presented in Table 1 and 2.

The ammonia nitrogen content in the Chernaya River waters in the 2015–2020 period varied from 0.00 to 161.58 $\mu\text{mol/l}$. The maximum concentration was recorded in April 2018 by a railway bridge in Inkerman (station 9).

The concentrations of the sum of nitrates and nitrites varied in the range of 5.41–499.76 $\mu\text{mol/l}$, the maximum content of oxidized nitrogen was determined in April 2018 also at station 9.

Table 1

Concentration of nutrients, $\mu\text{mol/l}$, in the Chernaya River waters in 2015–2020

Characteristic	NH_4^+	$\text{NO}_2^- + \text{NO}_3^-$	SiO_3^{2-}	PO_4^{3-}
C_{\min}	0.00	5.41	1.61	0.00
C_{\max}	161.58	499.76	256.85	13.12
Median	3.14	31.32	38.75	0.10
Standard deviation	11.92	47.36	42.75	1.49

The variation range of the concentration of phosphorus (PO_4^{3-}) in the river waters was 0.00–13.12 $\mu\text{mol/l}$. Their maximum content was recorded in August 2020 at station 9. Moreover, in September 2015, the concentration of phosphorus at this station was also high and amounted to 11.34 $\mu\text{mol/l}$.

Maximum silicon (SiO_3^{2-}) content in 2015–2020 was noted in September 2016 in a tributary of the Urkusta River (station 4) and in November 2017 in the area of the gauging station at Red Rock (station 6), the concentrations reached 256.85 and 201.90 $\mu\text{mol/l}$, respectively. The overall range of concentration changes during this study period was 1.61–256.85 $\mu\text{mol/l}$.

In 2010–2014, the median content of ammonia nitrogen and silicon was lower than in 2015–2020 (Table 2). The variation range in the ammonia nitrogen concentration was 0.00–30.46 $\mu\text{mol/l}$, silicon – 0.99–308.15 $\mu\text{mol/l}$.

Table 2

Concentration of nutrients, $\mu\text{mol/l}$, in the Chernaya River waters in 2010–2014

Characteristic	NH_4^+	$\text{NO}_2^- + \text{NO}_3^-$	SiO_3^{2-}	PO_4^{3-}
C_{\min}	0.00	11.17	0.99	0.00
C_{\max}	30.46	302.19	308.15	6.22
Median	1.01	39.16	35.85	0.13
Standard deviation	6.20	50.34	48.63	0.95

The median concentrations of the sum of nitrates and nitrites are the same as the ones of phosphorus, in 2010–2014 they slightly exceeded the corresponding concentrations in 2015–2020. The oxidized nitrogen content varied from 11.17 to 302.19 $\mu\text{mol/l}$, phosphorus – from 0.00 to 6.22 $\mu\text{mol/l}$.

Seasonal variability of nutrients concentrations

When considering seasonal distribution of ammonia nitrogen in 2015–2020 (Fig. 2, *a*), it can be noted that the concentrations at stations in the area of the Chernorechenskoe reservoir and along the entire course of the Chernaya River were distributed almost evenly. The exception was increased values in summer at stations 3, 4, located near Ozernoye and Peredovoye villages, as well as at station 9 throughout the year.

The minimum concentrations of the sum of nitrates and nitrites (Fig. 2, *b*) occurred in the summer period, the maximum ones were typical for the spring-winter period. An increased content of oxidized nitrogen was determined in winter in the the Baydarka River area (station 2) and a culvert under the road in Ozernoe village (station 3), as well as during all seasons by the railway bridge in Inkerman (station 9).

Throughout the entire study period, the maximum phosphorus content was observed at station 9 (Fig. 2, *c*). Its increased concentrations were determined during all seasons in the area of stations 2, 3. A decrease in phosphorus content throughout the river occurred in the summer and autumn periods.

Increased silicon concentrations (Fig. 2, *d*) were observed at stations 2, 3, 4, as well as at station 9. The maximum values were observed in the autumn period in the Urkusta River tributary (station 4), into which the wastewater from Peredovoe village inflows.

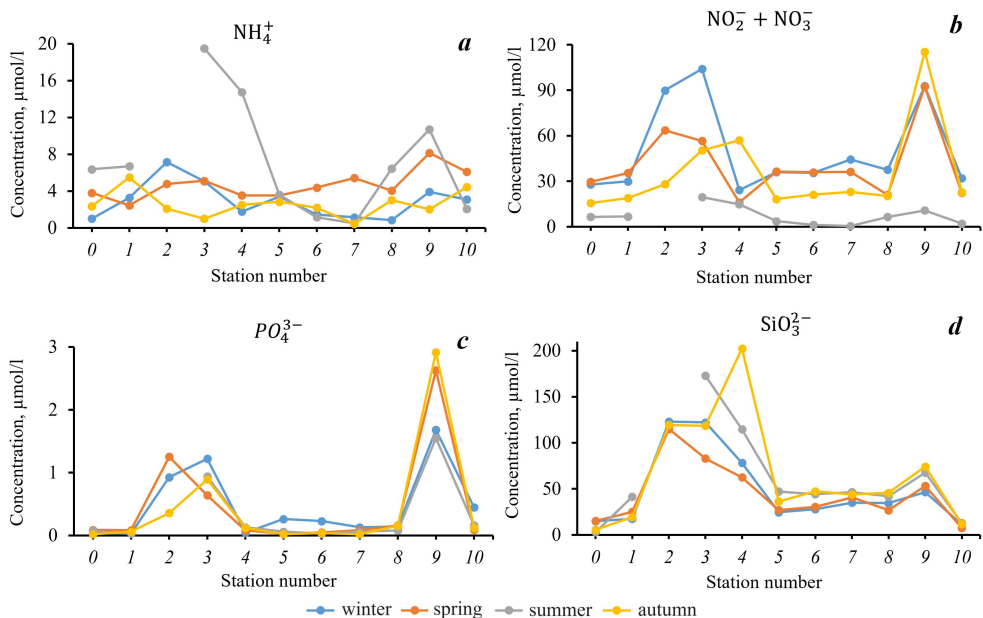


Fig. 2. Seasonal distribution of nutrients in the Chernaya River waters in 2015–2020

Interannual variation of nutrient content.

Compared to the period from 2010 to 2014, in 2015–2020 the ammonia nitrogen supply increased on average 2.7 times throughout the entire course of the river (Fig. 3, a). This increase is especially obvious at stations 1, 2 and 3.

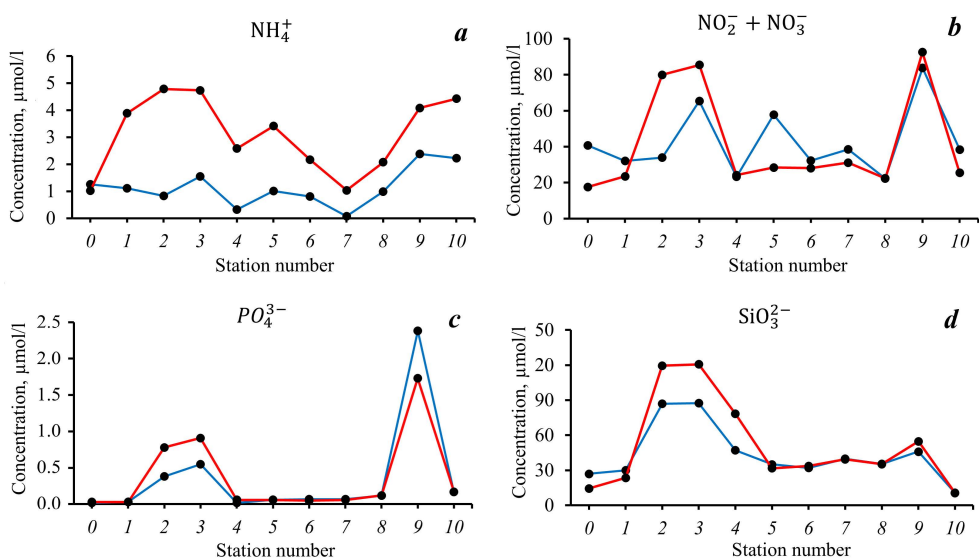


Fig. 3. Mean long-term nutrients content in the Chernaya River waters (blue line denotes 2010–2014, red line – 2015–2020)

An analysis of changes in the oxidized nitrogen concentration (Fig. 3, *b*) also revealed its increase in 2015–2020 in the area of stations 2 and 3 and a twofold decrease at station 5, located between Shirokoe and Ozernoye villages.

Variation of phosphorus concentration along the river course in 2015–2020 and 2010–2014 has a similar character (Fig. 3, *c*), in the same way as for inorganic nitrogen compounds, an increase in concentrations at stations 2 and 3 takes place.

Variation of silicon concentration in both periods under consideration is similar (Fig. 3, *d*). At the same time, there is an increase in its content compared to the earlier period at stations 2, 3 and 4.

Quantitative estimates of nutrients supply with river waters

According to [12], the mean long-term runoff of the Chernaya River is ~ 57.7 million m³/year. In this case, two periods are distinguished – high-water (December – April) with the runoff amount of 51.2% from the annual one and low-water (May – November). Based on these values, as well as data on the median concentration of nutrients in the river waters, we calculated the nutrients outflow into Sevastopol Bay for two periods under consideration: 2015–2020 and 2010–2014 (Table 3).

Table 3

Nutrients outflow with the Chernaya River waters in 2010–2014 and 2015–2020				
Outflow	NH ₄ ⁺	NO ₂ ⁻ +NO ₃ ⁻	SiO ₃ ²⁻	PO ₄ ³⁻
Mean long-term, t/year	0.82 / 2.50	31.64 / 25.30	57.93 / 62.21	0.23 / 0.18
High water period, t/season	0.36 / 1.33	17.85 / 16.01	35.86 / 29.55	0.11 / 0.12
Low water period, t/season	0.78 / 1.14	11.41 / 9.02	13.60 / 32.18	0.12 / 0.08

Discussion of the results

Regular variations were observed in the nutrient content along the Chernaya River course. They were caused, as was shown earlier in [13], by the activity of the consumption processes of these elements by plants and organic matter mineralization, as well as their entry with surface runoff from the catchment area and with wastewater.

Seasonal variations in 2015–2020

Minimum concentrations of the sum of nitrates and nitrites (Fig. 2, *b*) in summer can be explained by their active consumption by autotrophic bacteria. Maximum concentrations of these nutrients during spring-winter floods are typical for the period of maximum surface washout, as well as for the low-water period due to the oxidation of autochthonous organic substances and a relative increase in the share of wastewater with a decrease in natural runoff [2].

Increased concentrations of phosphorus at stations 2 and 3 can be explained by their entry into the Chernaya River waters as a result of the washout of water containing fertilizers from the fields. The decrease in phosphorus content in summer and autumn periods is probably due to their transition to organic form as a result of their consumption by aquatic organisms in the process of life.

Silicon content level in river waters, compared to the content of nitrogen and phosphorus compounds, is determined to a lesser extent by the action of anthropogenic factors [6]. The highest silicon concentrations were noted during the flood period, which is consistent with [3].

Wastewater discharges from sewage treatment plants (STP 5) located near Ozerne village can have an effect on the increase of the nutrients content in the area of stations 2 and 3 [14]. These treatment facilities have a biological type of water purification, the essence of which is in the breakdown of nitrogen-containing organic compounds by microorganisms, and as a result ammonia is released in large quantities³. Under natural conditions, ammonia oxidation (nitrification) occurs with the formation of nitrous acid salts (nitrates). According to [14], the volume of wastewater discharged from STP 5 is about 18 thousand tons/year. An average concentration of ammonia nitrogen in wastewater is 21.42 $\mu\text{mol/l}$, the sum of nitrates and nitrites – 2157 $\mu\text{mol/l}$, phosphorus – 93.55 $\mu\text{mol/l}$.

The constantly increased concentrations of all the considered nutrients in the river waters at station 9, recorded every year in all seasons, are noteworthy. In the area of the specified sampling station there is a permanent water outlet, presumably from the *Sevagrosoyuz* agricultural firm. The main activity of this company, according to the information on the website⁴, is growing vegetables. In April and August 2023, we took water samples from this outlet and analyzed them for nutrients content. It was found that the concentration of ammonium ions exceeded the maximum allowable concentration (MAC) for water bodies of fishery importance⁵ by 5.5 times, nitrites by 9.1 times, nitrates by 4.5 times, phosphorus by 8.7 times, silicon – by 22 times.

It can be assumed that such high nutrients concentrations are the result of the washout of mineral fertilizers (nitrogen, phosphorus, etc.) from the fields of an agricultural company and their entry with groundwater or wastewater. Apparently, the runoff of water containing such significant amounts of inorganic forms of nutrients from this outlet can contribute to an increase in their concentrations in the Chernaya River waters at station 9.

In addition, in [14] it is noted that in the area of this station there is a point of wastewater discharge from sewage treatment plants located in Sakharnaya Golovka village with a volume of discharge into the river of 420 thousand tons/year. An average concentration of ammonia nitrogen in these waters is 21.42 $\mu\text{mol/l}$, the sum of nitrates and nitrites is 2435 $\mu\text{mol/l}$ and phosphorus – 196.75 $\mu\text{mol/l}$. In addition, slightly upstream of the river there are water treatment facilities with a discharge volume of 1680 thousand tons/year, where the average concentration of ammonia nitrogen is 3.57 $\mu\text{mol/l}$, the sum of nitrates and nitrites is 1143 $\mu\text{mol/l}$ and

³ Golubovskaya, E.K., 1978. [*Biological Principles of Water Purification*]. Moscow: Vysshaya Shkola, 271 p. (in Russian).

⁴ Sevagrosoyuz. *Details*. [online]. Available at: <https://spark-interfax.ru/sevastopol-balaklavski/ooo-sevagrosoyuz-inn-9202002342-ogm-1149204043526-aea1ce5322814e16b93d772bdf926635> [Accessed: 10 May 2024] (in Russian).

⁵ Russian Ministry of Health, 1998. *Maximum Allowable Concentrations (Macs) of Chemicals in the Water of Water Objects Used for Drinking and Domestic-Recreation Purposes: GIN 2.1.5.689–98*. Moscow: Ministry of Health, 77 p. (in Russian).

phosphorus – 16.13 $\mu\text{mol/l}$. Perhaps this source may also be the cause for high content of nutrients in the river waters at this station.

Note that sampling stations 9 and 10 are located in the mixing zone of river and sea waters, i.e., they belong to the marginal filter. Therefore, increased nutrient concentrations in the river waters at these stations have a significant impact on Sevastopol Bay ecosystem.

Interannual variation of nutrient content

The increase in ammonia nitrogen concentration is especially obvious in 2015–2020 compared to the earlier period, it manifests itself at stations 1, 2 and 3, located near Shirokoe and Ozernoye villages. Livestock farming and agricultural activities are quite developed in these villages, but there are no sewage systems or wastewater treatment.

The identified increase in concentrations of the sum of nitrates and nitrites, as well as phosphorus in the area of stations 2 and 3, that took place in 2015–2020, may be associated with the inflow of nitrogen-phosphorus fertilizers into groundwater from farmland. At the same time, the fact that nutrients concentration at station 5 has doubled (between Shirokoe and Ozernoye villages) can be explained by mixing of relatively pure waters from station 1 (water intake under the reservoir) and polluted water from stations 3 and 4 (Ozernoye village and the inflow from the pond in Peredovoe village).

Increase in silicon concentrations in 2015–2020 at stations 2 and 3 may be the result of anthropogenic impact, namely agricultural work and the growth of residential development in nearby villages. In addition, near station 3 we noted active construction of a group of cottages on the hill, not indicated on the online maps. This activity leads to a release of silicates into groundwater and then into the river. Station 4 is less anthropogenically loaded, so the increase in silicon concentration here can probably be explained by leaching of rocks.

Conclusion

The work considers nutrients content (average and seasonal) in the Chernaya River waters, as well as its variation in the river waters in two separate periods: from 2010 to 2014 (before the active development of the Baydar Valley lands) and from 2015 to 2020.

During the periods under consideration, regardless of the season, increased concentrations of all nutrients were observed at stations in the Baydar Valley area and at the railway bridge in Inkerman. The main sources of inorganic nitrogen and phosphorus compounds entering the river in the station 9 area may be a water outlet (presumably from the *Sevagrosoyuz* agricultural firm) and wastewater from STPs located in Sakharnaya Golovka village. The maximum concentrations of silicon were observed in the Urkusta River tributary and in the gauging station area at Red Rock, which may be the result of leaching of rocks and earthworks.

During the analysis of interannual variations in nutrients concentration, it was found that in 2015–2020 their content, compared to the period before 2014, increased at stations in the Baydar Valley area, while the ammonia nitrogen content increased along the entire course of the Chernaya River.

The flow of phosphorus with river waters into Sevastopol Bay in both periods under consideration was almost unchanged. The average long-term outflow of ammonia nitrogen with river waters in 2015–2020 was three times higher than this index for 2010–2014 period. The silicon flow with the Chernaya River waters in May – November in 2015–2020 exceeded the one in 2010–2014 almost 2.5 times, which can be explained by the intensification of construction work during the warm period of the year.

The data obtained during the work indicate the need for the construction of sewerage and wastewater treatment systems for enterprises and residential buildings in the Baydar Valley, which has been discussed over the past decade.

REFERENCES

1. Makarov, M.V. and Viter, T.V., 2021. Spatial-Time Changes in the Macrozoobentos of the Chernaya River Mouth and the Top of Sevastopol'skaya Bay (South-West Crimea). *Scientific Notes of V.I. Vernadsky Crimean Federal University. Biology. Chemistry*, 7(4), pp. 92-107 (in Russian).
2. Ovsyany, E.I. and Orekhova, N.A., 2018. Hydrochemical Regime of the River Chernaya (Crimea): Environmental Aspects. *Physical Oceanography*, 25(1), pp. 77-88. <https://doi.org/10.22449/1573-160X-2018-1-77-88>
3. Orekhova, N.A., Medvedev, E.V. and Ovsyany, E.I., 2018. Influence of the River Chernaya Water on Hydrochemical Regime of the Sevastopol Bay (the Black Sea). *Ecological Safety of Coastal and Shelf Zones of Sea*, (3), pp. 84-91. <https://doi.org/10.22449/2413-5577-2018-3-84-91> (in Russian).
4. Sovga, E.E. and Khmara, T.V., 2020. Influence of the Chernaya River Runoff during High and Low Water on the Ecological State of the Apex of the Sevastopol Bay Water Area. *Physical Oceanography*, 27(1), pp. 28-36. <https://doi.org/10.22449/1573-160X-2020-1-28-36>
5. Skibinsky, L.E., 2005. Geochemical Barriers and Their Role in the Formation of Ecological-Chemical State of Water of the White Sea. In: A. F. Alimov, V. Ya. Berger, E. P. Ieshko and N. N. Nemova, eds., 2005. *The Study, Sustainable Use and Conservation of Natural Resources of the White Sea. Proceedings of the IXth International Conference. October 11-14, 2004, Petrozavodsk, Karelia, Russia*. Petrozavodsk: Karelian Research Center of RAS, pp. 280-284 (in Russian).
6. Savichev, O.G., 2003. [*Rivers of the Tomsk Region: Condition, Use and Protection*]. Tomsk: TPU, 202 p. (in Russian).
7. Minkovskaya, R.Ya., 2020. *Comprehensive Studies of Different Types of River Mouths (on the Example of the River Mouths in the North-Western Part of the Black Sea)*. Sevastopol: MHI RAS, 364 p. <https://doi.org/10.22449/978-5-6043409-2-9> (in Russian).
8. Orekhova, N.A., Medvedev, E.V. and Ovsyany, E.I., 2018. Influence of the River Chernaya Water on Hydrochemical Regime of the Sevastopol Bay (the Black Sea). *Ecological Safety of Coastal and Shelf Zones of Sea*, (3), pp. 84-91. <https://doi.org/10.22449/2413-5577-2018-3-84-91> (in Russian).
9. Ovsyany, E.I., Romanov, A.S., Min'kovskaya, R.Ya., Krasnovid, I.I., Ozyumenko, B.A. and Zymbal, I.M., 2001. The Most Important Sources of Pollution for the Marine Environment of the Coastal Zone of Sevastopol. In: MHI, 2001. *Ecological Safety of Coastal and Shelf Zones and Comprehensive Use of Shelf Resources*. Sevastopol: ECOSI-Gidrofizika. Iss. 2, pp. 138-152 (in Russian).
10. Ovsyany, E.I., Artemenko, V.M., Romanov, A.S. and Orekhova, N.A., 2007. The Chernaya River Discharge as a Factor Affecting the Water-Salt Regime Forming and Ecological State of the Sevastopol Bay. In: MHI, 2007. *Ecological Safety of Coastal and Shelf Zones and Comprehensive Use of Shelf Resources*. Sevastopol: MHI. Iss. 15, pp. 57-65 (in Russian).

11. Solórzano, L., 1969. Determination of Ammonia in Natural Waters by the Phenolhypochlorite Method. *Limnology and Oceanography*, 14(5), p. 799-801. <https://doi.org/10.4319/lo.1969.14.5.0799>
12. Minkovskaya, R.Ya., 2008. Geophysical Characteristics of Mouth Area of the Chernaya River. In: MHI, 2008. *Ecological Safety of Coastal and Shelf Zones and Comprehensive Use of Shelf Resources*. Sevastopol: ECOSI-Gidrofizika. Iss. 17, pp. 194-214 (in Russian).
13. Moiseenko, O.G., Khoruzhiy, D.S. and Medvedev, E.V., 2014. Carbonate System in the Chernaya River Waters and in the Zone of the Chernaya River – Sevastopol Bay Biogeochemical Barrier (the Black Sea). *Morskoy Gidrofizicheskiy Zhurnal*, (6), pp. 47-60 (in Russian).
14. Verzhvetskaya, L.V. and Minkovskaya, R.Ya., 2020. Structure and Dynamics of Anthropogenic Load on the Coastal Zone of the Sevastopol Region. *Ecological Safety of Coastal and Shelf Zones of Sea*, (2), pp. 92-106. <https://doi.org/10.22449/2413-5577-2020-2-92-106> (in Russian).

About the authors:

Maria A. Myslina, Junior Research Associate, Marine Hydrophysical Institute of RAS (2 Kapitanskaya Str., Sevastopol, 299011, Russian Federation), **ORCID ID: 0000-0002-0054-0379**, myslina@mhi-ras.ru

Alla V. Varenik, Senior Research Associate, Marine Hydrophysical Institute of RAS (2 Kapitanskaya Str., Sevastopol, 299011, Russian Federation), CSc (Geogr.), **ORCID ID: 0000-0001-5033-4576**, **ResearcherID: H-1880-2014**, **Scopus Author ID: 56960448000**, alla.varenik@mhi-ras.ru

Diana V. Tarasevich, Engineer-Researcher, Marine Hydrophysical Institute of RAS (2 Kapitanskaya Str., Sevastopol, 299011, Russian Federation), **ORCID ID: 0000-0003-4893-9685**, ledi_di2020@bk.ru

Contribution of the co-authors:

Maria A. Myslina – formulation of goals and objectives of the study, qualitative and quantitative analysis of the results and their interpretation, discussion of work results, preparation of graphic materials

Alla V. Varenik – general scientific supervision of the study, formulation of conclusions, qualitative and quantitative analysis of results and their interpretation

Diana V. Tarasevich – review of the literature on the research problem, qualitative and quantitative analysis of the results and their interpretation

The authors have read and approved the final manuscript.

The authors declare that they have no conflict of interest.

Original article

Sea Level Oscillations in the Adjacent Bays – Trade Port and Kholmsk-Severnny (Sakhalin Island)

D. P. Kovalev ¹, Yu. V. Manilyuk ^{2, ✉}, P. D. Kovalev ¹

¹ *Institute of Marine Geology and Geophysics, Far Eastern Branch of RAS, Yuzhno-Sakhalinsk, Russian Federation*

² *Marine Hydrophysical Institute of RAS, Sevastopol, Russian Federation*

✉ uvmsev@yandex.ru

Abstract

Purpose. The paper is purposed at studying long-wave processes in Kholmsk bays and on the adjacent shelf (including the interaction of bays) based on the theoretical concepts and the data of sea level field observations obtained in September 2022 – May 2023.

Methods and Results. Three autonomous wave meters ARW-14 K installed in the bays of Trade Port and Kholmsk-Severnny, as well as on the shelf at an insignificant distance from the bays were used for observations. The measurement discreteness was 1 second. The time series both including the tides and without them were studied based on the spectral analysis using the Kyma program. Within the range of wave periods 1–30 h, the wave processes of a non-tidal origin and with the periods 1.6–6.7 h were found. They can be attributed to the shelf seiches, the Poincaré waves or the Tatar Strait seiches. Spectral analysis in the period range 1–10 min has shown the presence of seiches with the periods 1.83–8.17 min in Trade Port Bay and those with the periods 1.32–8.65 min in Kholmsk-Severnny Bay.

Conclusions. It is established that in course of the whole series of field observations, the coupled oscillations at the periods ~ 8 min took place in the above-mentioned bays. These oscillations correspond to the Helmholtz mode of Kholmsk-Severnny Bay. They are induced in this bay and then transmitted to Trade Port Bay due to interaction. At different times they had both in-phase and anti-phase spatial structures. During the periods of high eigen modes the interaction between the bays was not detected. Besides, the spectral analysis of the sea level oscillations under study made it possible to reveal the beats with a period 4.82 h (289.2 min), resulting from the interaction of modes with the close periods equal to 8.17 and 8.65 min. The stated facts, as well as correspondence of the distance between the bays' inlets to the proposed earlier interaction condition criterion allow us to assert that the coupled oscillations are present in two adjacent bays – Kholmsk-Severnny and Trade Port.

Keywords: sea level oscillations, seiches, Poincaré waves, coupled oscillation system

Acknowledgments: Within the framework of the theme of state assignment of FSBSI FRC MHI FNNN-2024-0016, the results of field observation data processing were analyzed and interpreted; and within the framework of the theme of state assignment of FSBSI Institute of Marine Geology and Geophysics, FEB of RAS FWWM-2024-0002, the field observation data were collected, processed and subsequently analyzed.

For citation: Kovalev, D.P., Manilyuk, Yu.V. and Kovalev, P.D., 2024. Sea Level Oscillations in the Adjacent Bays – Trade Port and Kholmsk-Severnny (Sakhalin Island). *Physical Oceanography*, 31(3), pp. 409-426.

© 2024, D. P. Kovalev, Yu. V. Manilyuk, P. D. Kovalev

© 2024, Physical Oceanography

Introduction

Climate changes occurring in recent decades and accompanied by increased atmospheric disturbances and an increase in their duration require regular sea level observations in order to obtain an up-to-date understanding of the processes taking place in the coastal zone, especially in the areas where seaports are located.

Trade and Kholmsk-Severnoy ports are located in the bays of Kholmsk (Sakhalin Island); they are important not only for the city, but also for the entire island (Fig. 1). A connection with the mainland is held through Trade Port by the Vanino-Kholmsk ferry crossing by means of which a large volume of various cargoes is transported. The water areas of the bays adjacent to the ports are protected well from wind waves by hydraulic structures of various types [1]. However, for long-wave oscillations coming from the sea, such protection is ineffective. This type of oscillations, in particular, includes tidal ones, which have harmonics with periods from days to several hours [2]. The source of long-wave disturbances can be two fundamentally different types of processes leading to the formation of long waves – anemobaric (AB) and infragravity (IG) ones [3]. Anemobaric waves are generated due to the effect of atmospheric pressure and wind fluctuations on the sea surface, as well as level oscillations caused by the energy dissipation of large-scale long-wave formations such as meteorological tides or storm surges on heterogeneities of the relief and coastline. Infragravity waves arise from the nonlinear interaction of wind waves or large swells. Characteristic periods of AB waves lie in the range from several tens of seconds to several hours, and IG waves – in the range of 30–300 s. Penetrating onto the shelf and into the internal waters, these waves induce resonant seiche oscillations there.

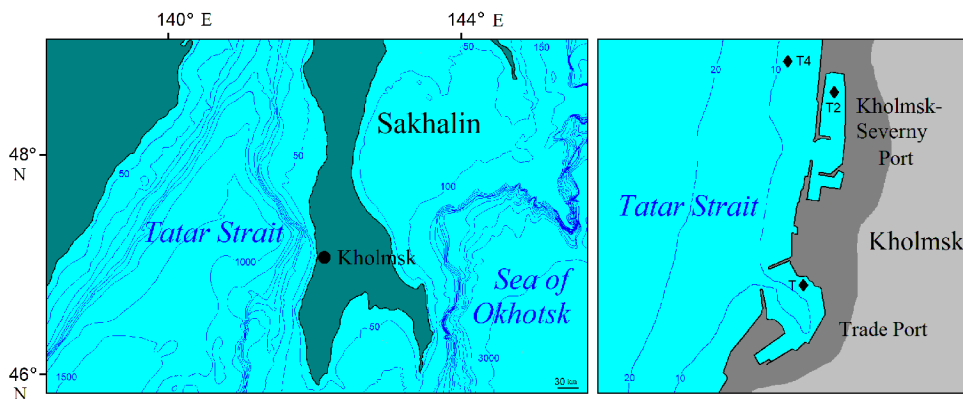


Fig. 1. Maps of the region and the water area near Kholmsk showing locations of device installations marked with black diamonds

A peculiar feature of Kholmsk is presence of two closely spaced bays of comparable size (the distance between inlets is ~ 1 km) with a coupled system of oscillations (Fig. 1). Such an oscillatory system can be interpreted as two coupled oscillators. The paper [4] describes a study using a laboratory setup of water oscillations in two connected bays of equal sizes. It is demonstrated that due to the connection, the oscillations arising in one bay are transmitted to the neighboring one. In addition, the resonant periods of the bays vary due to the connection; the occurrence of both in-phase and anti-phase oscillations, as well as beats, is possible.

Seiches in adjacent real bays have recently aroused great interest among researchers, since this topic, in addition to scientific, has practical significance. Thus,

the works [5–8] describe seiches in adjacent bays located in different regions of the World Ocean. However, these works consider bay systems that include a bay that is larger than the others. Kholmsk bays are almost equal in size; their interaction has not yet been studied.

The purpose of this paper is to study, based on theoretical concepts and data from field observations carried out recently, long-wave processes in the bays of Kholmsk and at the adjacent shelf, including the study of interaction of these bays.

Materials and methods

Object of study. The water areas of Kholmsk bays are demonstrated in Fig. 1. According to the website http://retromap.ru/1419537_z7_46.335550,142.22351&h=0, the parameters of the bays are as follows: Kholmsk-Severny Port – total length is 1008 m, length to the southern partition is 816 m, wide part length is 890 m, northern part length is 513 m, width at the inlet between the external piers is 221 m, width of the bay inlet is 139 m, average depth is 6.2 m; Trade Port – length to the ferry berth is 732 m, length from the bay inlet to the wall is 556 m, width is 422 m, narrow apex width is 109 m, its length is 350 m, bay inlet width is 174 m, average depth along the fairway is 6.5 m. The distance between the centers of the inlets to the bays is 1045 m.

The Tatar Strait near Kholmsk is generally characterized by a relatively weak manifestation of frequency-selective properties of the water area determined by topography: the shelf near Kholmsk is the narrowest and deepest off the western coast of Sakhalin, it expands both in the southern and in the northern directions. The shelf width in the Kholmsk area is ~ 40 km, the bottom slope is 0.0078.

Sea level observations. Sea level observations were carried out from September 2022 to May 2023 using three autonomous ARW-14 K wave meters: T meter (serial number 152), T2 meter (serial number 142) and T4 meter (serial number 149) (Fig. 1). The fourth device was also installed in the sea at an isobath of 4 m opposite the inlet of Kholmsk-Severny Bay, but it turned out to be faulty. Accuracy of bottom hydrostatic pressure measuring, which was subsequently converted into sea level oscillations taking into account the attenuation of short waves with depth, is 0.06% of the full scale of measurement and the pressure resolution is equal to $\pm 0.0003\%$ of the full scale of measurement. Discreteness of sea level and temperature measurements is 1 s.

Methods for processing data from field observations. Spectral analysis, filtering, tide subtraction and visualization of results and time series were performed using Kyma software, designed for complex processing and analysis of large-scale sea level data¹ [9]. The program enables to calculate the spectral density of oscillations for a selected time series using the usual windowed Fourier transform.

¹ Kovalev, D.P., 2018. *Kyma. PC Software*. Yuzhno-Sakhalinsk: IMGIG FEB RAS. State Registration No. RU2018618773 (in Russian).

The time series is divided into $(2n/w) - 1$ windows, where n is time series length, w is window size; the next segment of the time series is selected with a shift of half the length of the window. Filtration is carried out over each segment using the Kaiser–Bessel window (filtering can be disabled). For each window, the Fourier transform is then calculated for a predefined number of frequencies, starting at a given frequency. After calculating spectral parameters for each window, the average value between them is calculated.

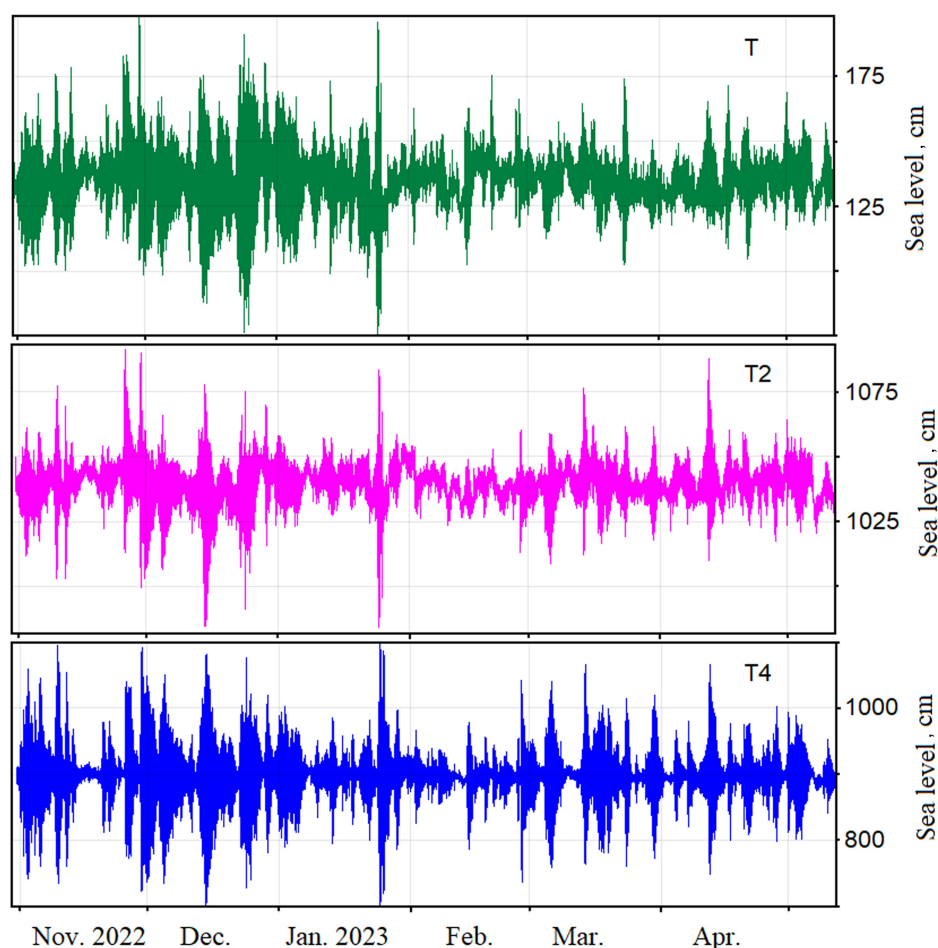


Fig. 2. Recorded time series of sea level oscillations from which the precalculated tide is subtracted. Here and in other figures, the device locations are shown: device T is installed in Trade Port Bay, T2 – in Kholmsk-Severny Bay, and T4 – in the Tatar Strait (on the shelf)

As a result of the observations, long-term time series of sea level variations were obtained. To analyze seiche oscillations, the precalculated astronomical tide was subtracted from the time series. Calculation of tidal harmonics and their subtraction

from the original time series is performed with the help of 35 astronomical harmonics using LSMTM.exe application in the Kyma program. LSMTM.exe algorithm uses the least squares method, which was developed by A.B. Rabinovich and G.V. Shevchenko in the 70s of the 20th century. It has been tested several times and has shown good results in calculating tides. The time series with subtracted precalculated tide are given in Fig. 2.

Results and discussion

Using the time series obtained as a result of sea level observations and the Kyma program, spectral densities of level oscillations were calculated over the entire length of the time series. Since, as further studies showed, wave processes with periods of > 8 min were observed in the bays and they could not be seiches of the bays themselves; it is of interest to consider the range of wave processes for longer periods. In addition, it is necessary to separate tidal harmonics from seiches and other types of waves for the analysis.

Long-period tidal sea level oscillations. Spectral densities of sea level oscillations for time series with tide and series from which the precalculated tide is subtracted are shown in Fig. 3. This makes it possible to determine which peaks correspond to tidal harmonics and which – to other wave processes.

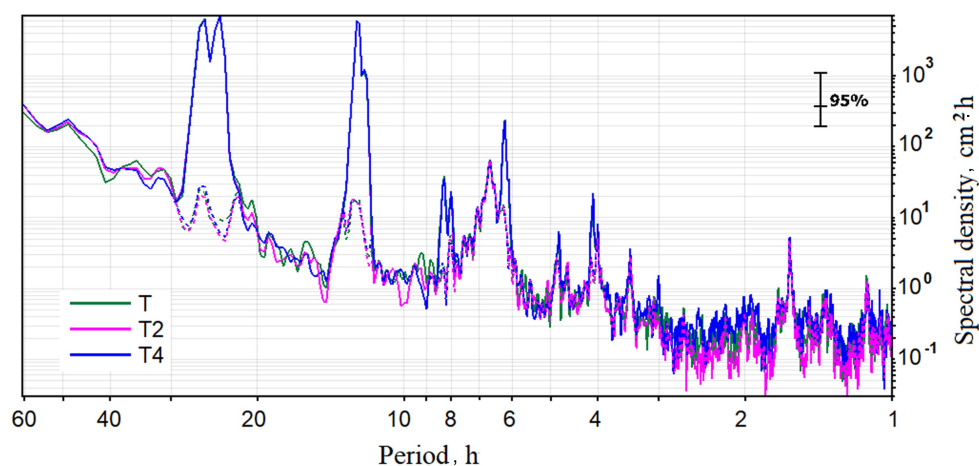


Fig. 3. Spectral densities of sea level oscillations for the time series with a tide (solid lines), and for the series from which the precalculated tide is subtracted (dashed lines)

The periods of maxima in the spectral densities of sea level oscillations are given in Table 1. This table also compares the values of the obtained periods and similar values of the periods of tidal harmonics according to the monograph [2]. Spectral peaks that do not have periods close to tidal harmonics can be attributed to wave processes of a different, non-tidal nature.

Table 1

**Periods of wave peaks in spectral densities of sea level oscillations
and corresponding tidal harmonics**

Components of sea level oscillations	Period, h										
Inclusive of tide	24.7	23.8	12.4	12.0	8.12	8.00	–	6.22	–	4.1	4.0
Not inclusive of tide	–	–	–	–	–	–	6.67	–	4.82	–	3.43 1.62
Tidal harmonic [2]	M_1	K_1	M_2	S_2	MK_3	SP_3	–	SO_4	–	$2MS_6$	M_6

Long-wave processes of non-tidal nature. It can be seen from Table 1 that in the bays of Kholmsk and the adjacent area of the open sea the wave processes of a non-tidal nature with periods of > 1 h take place. The class of such waves includes Poincaré waves and shelf seiches.

Poincaré waves. Continuous spectra of the radiated waves (Poincaré waves) were studied because they could also be correlated with the recorded spectral peaks. With this phenomenon, similar to resonance in an organ pipe [10], a wave coming from the open ocean can be significantly amplified at selected “resonant” frequencies as a result of multiple reflections from the coast and shelf boundary.

Amplitude amplification γ (the ratio of the wave amplitude near the shore to the wave amplitude in the open ocean) is a characteristic that describes the continuous spectrum of Poincaré waves. Its value depends on the frequency of the wave and the alongshore wave number. If we assume that the shelf has a parabolic shape (along its entire length of 86 km), then generally the sea depth at the shelf is described by the equation $h = ax^2$ at $x_0 < x < L$. Then the Poincaré wave amplification factor $\gamma(\omega, 0)$ has the form according to the monograph ²:

$$\gamma(\omega, 0) = 2 \sqrt{\frac{L}{x_0}} \sigma (4\sigma^2 + 1 - \cos(2\mu\sigma) + 2\sigma \sin(2\mu\sigma))^{-1/4} \quad (1)$$

at $\sigma^2 > 0$. Here $\mu = \ln \frac{L}{x_0}$; $\sigma^2 = \frac{(\omega^2 - f^2)}{gH} - \frac{1}{4}$, where f is Coriolis parameter,

$\varphi = 47.06^\circ\text{N}$ for Trade Port Bay. The Coriolis parameter is determined by the well-known formula $f = 2\Omega \sin \varphi$, where φ is location latitude; $\Omega = 7.2921 \cdot 10^{-5} \text{ cycle} \cdot \text{s}^{-1}$ is circular frequency of the Earth’s rotation. Function $\sin \varphi = 0.732$, taking this into account we obtain an inertial frequency of $0.384 \text{ cycles} \cdot \text{h}^{-1}$, the period of inertial oscillations is 16.34 h.

The calculation of Poincaré waves amplification factor using equation (1) for the shelf under consideration in the Kholmsk region with the approximation $h(x) = 0.32x^2$ (x , km is the distance from the coast) revealed that they can include waves with a period of 3.56 h, which has a maximum with a value of 2.25. Note that in the energy spectrum there is a peak at 3.43 h period, which is close to the maximum

² Efimov, V.V., Kulikov, E.A, Rabinovich, A.B. and Fine, I.V., 1985. [Ocean Boundary Waves]. Leningrad: Gidrometeoizdat, 280 p. (in Russian).

amplification; the second maximum with a value of 2.1 at a period of 1.63 hours is also close to the peak in spectral density at a period of 1.62 hours (Table 1).

Other causes for the occurrence of spectral peaks with periods of 3.43, 4.82, 6.67 h are possible, in particular, these could be seiche modes of the Tatar Strait.

Shelf seiches. These are standing sea level oscillations with periods corresponding to resonant frequencies depending on the seabed slope. In the Kholmsk area, shelf depth variations at a distance of up to 40 km can be approximated by a linear dependence $h(x)=\alpha x$, where $\alpha = 0.0078$. The resonant periods of such a shelf are calculated using the equation from [3, p. 183]

$$T_n = 8\sqrt{L}/(n\sqrt{g\alpha}), \quad (2)$$

where L is shelf width; $n = 1, 3, 5, \dots$ is a number of mode; g is gravitational acceleration.

When calculating by equation (2), the period of the first mode is 1.61 h, the third is ~ 32 min, the fifth is ~ 19.3 min, the seventh is ~ 13.8 min, the ninth is ~ 10.7 min. We can assume that the period equal to 1.62 h (Table 1) belongs to the first mode of shelf seiches.

In addition to the first mode period, we obtained periods of the 3rd–9th modes, the values of which, lying in the range of 10.7–32 min, are close to the values of the observed peaks in the spectra. Therefore, it is obvious that waves coming to the shore from the open sea or passing atmospheric disturbances can induce shelf seiches in the resonant water area of the Tatar Strait near Kholmsk.

The carried out calculations and interpretation reveal that the peak periods identified by spectral densities can correspond to different wave processes – shelf seiches and Poincaré waves. It is difficult to determine specifically which of these processes was the cause of the observed peak; it is necessary to install several wave meters in the Tatar Strait waters near Kholmsk. The authors of this work also believe that Poincaré waves can contribute to the generation of seiche oscillations at periods close to them, but this problem is the theme of a separate study.

Seiches in the bays of Kholmsk. Seiches can be generated in bays under the effect of various factors. Many researchers have studied them in different water areas [11–14]. They revealed that the periods of seiche oscillations depend on the parameters of the water areas.

We are to consider waves with periods from 40 s to several tens of minutes, which include seiches in bays. For both bays we calculated the periods of eigen oscillations; this was carried out using the equation for a rectangular basin with an open inlet [15]:

$$\tau_{k,m} = \frac{4}{\sqrt{gh}} \frac{ab}{\sqrt{(1+2k)^2 b^2 + 4m^2 a^2}}, \quad (3)$$

where a , b , h are average length, width and depth of the bay, respectively; non-negative integers defining the mode number: $k = 0, 1, 2, \dots$, $m = 0, 1, 2$.

The periods of seiche oscillations calculated using equation (3) for basins having the characteristic dimensions of the bays under study are given in Table 2.

Table 2

Calculated by equation (3) seiche periods in the model basins approximating the bays of Kholmnsk

Mode number		Seiche periods $\tau_{k,m}$, min	
k	m	Trade Port	Kholmnsk-Severyn
0	0	4.7	8.6
1	0	1.6	2.9
2	0	0.9	1.7
3	0	0.7	1.2
0	1	2.7	0.9
1	1	2.0	0.9

Zero mode ($k = 0, m = 0$, the first largest value of the period for each water area) is the Helmholtz mode, which is similar to the fundamental tone of an acoustic resonator [16]. For the bays under consideration, the periods of this mode are 4.7 and 8.6 min.

In [17], the values of periods of Trade Port Bay longitudinal eigen modes were calculated under the assumption that the depth in its water area varies according to a parabolic law and at its inlet is 10 m. This calculation yielded the following values: 4.9; 2.0; 1.3; 0.9 min.

Figure 4 presents spectral densities for 40 s – 30 h periods of sea level oscillations. Note that the calculation was carried out for time series from which the precalculated tide was subtracted in order to exclude the impact of tidal harmonics of higher orders.

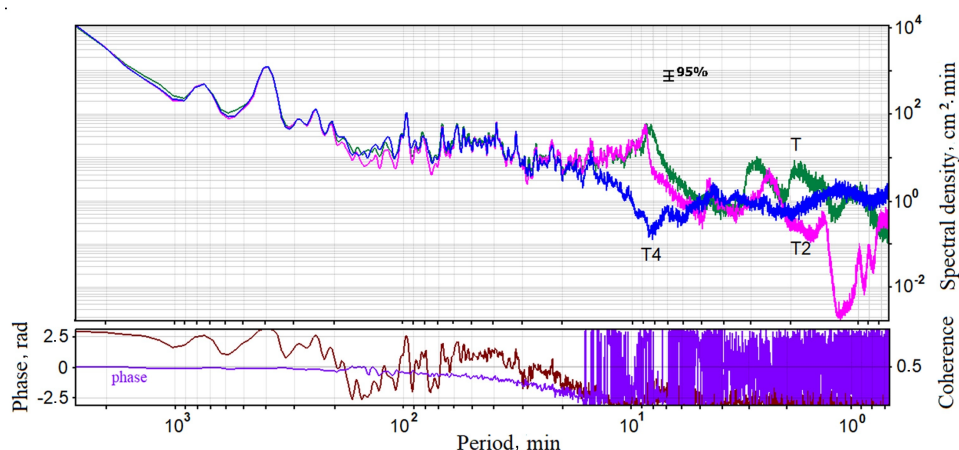


Fig. 4. Spectral densities of sea level oscillations, phase and coherence in the bays under study and in the Tatar Strait

In Fig. 4, the peaks of spectral densities in 1–10 min range of periods, the values of which exceed the confidence interval, are clearly visible. The periods of these peaks are given in Table 3, where the periods of shelf seiches with > 10 min values are also indicated. Previously performed studies of waves in Trade Port Bay revealed that wave processes with periods of ~ 1.83–8.17 min are seiches of this water area [18].

Table 3

**Peak periods in spectral densities resulted from processing
field observation data**

Water area	Period, min							
Kholmsk-Severyn	1.32	2.40	8.65	15.1	22.2	31.8	39.0	97.2
Trade Port	1.83	2.83	8.17	15.1	22.2	31.8	39.0	97.2
Tatar Strait	–	–	11.37	15.1	22.2	31.8	39.0	97.2

Note: Eigen periods of the bays are indicated in bold.

Note that wave processes with ~ 8 min periods are practically absent in the Tatar Strait open waters and in the area where T4 meter is installed (Fig. 4). This is due to a significantly pronounced minimum observed in the spectral density. At the same time, in [19] it is noted that the source of long-wave oscillations with the specified period recorded by the mareograph of Trade Port Bay are long-wave resonators that accumulate and amplify the energy of trapped waves in the area of Moneron Island and at the shelf near Chekhov. Numerical modeling of resonant oscillations in Trade Port Bay, according to this paper, did not demonstrate the presence of intense oscillations at ~ 8 min periods.

Comparison of the periods given in Table 2 and 3 shows that their values are close, except for the Helmholtz mode period of Trade Port Bay. Apparently, this is due to the fact that this bay has a large bayhead and equation (3) does not take into account the presence of such a water area feature. In [20], a study of the bay effect on seiches in a model rectangular basin with a bay was carried out and it was found that the presence of a bay leads to a change in the spatial structure of eigen oscillations and lengthens their periods, especially the one of the higher mode. Apparently, this circumstance contributes to the lengthening of the Helmholtz mode period in Trade Port Bay.

We note another unique property of the water area of Trade Port Bay water area – the presence of intense seiche oscillations over ~ 3 min period, which complicate the operation of the berth serving the ferry crossing [21]. This period corresponds to a single-node longitudinal seiche of the bay (Table 2), as well as the Helmholtz mode of its bayhead (~ 3 min). This further enhances the oscillations in the bayhead and western parts of the bay.

Interaction of bays. A number of papers [4, 5, 22] consider the manifestation of connections between the oscillations of two closely located bays and the possible presence of beats in them due to different periods of eigen oscillations. The authors of [5] believe that the interaction of connected bays will take place under condition $d/l_1 < 5.0$, where d is distance between the inlets of the bays; l_1 is length of one bay. For the bays of Kholmsk $d/l_1 = 1045 \text{ m}/1008 \text{ m} = 1.04$, therefore, interaction effects are possible.

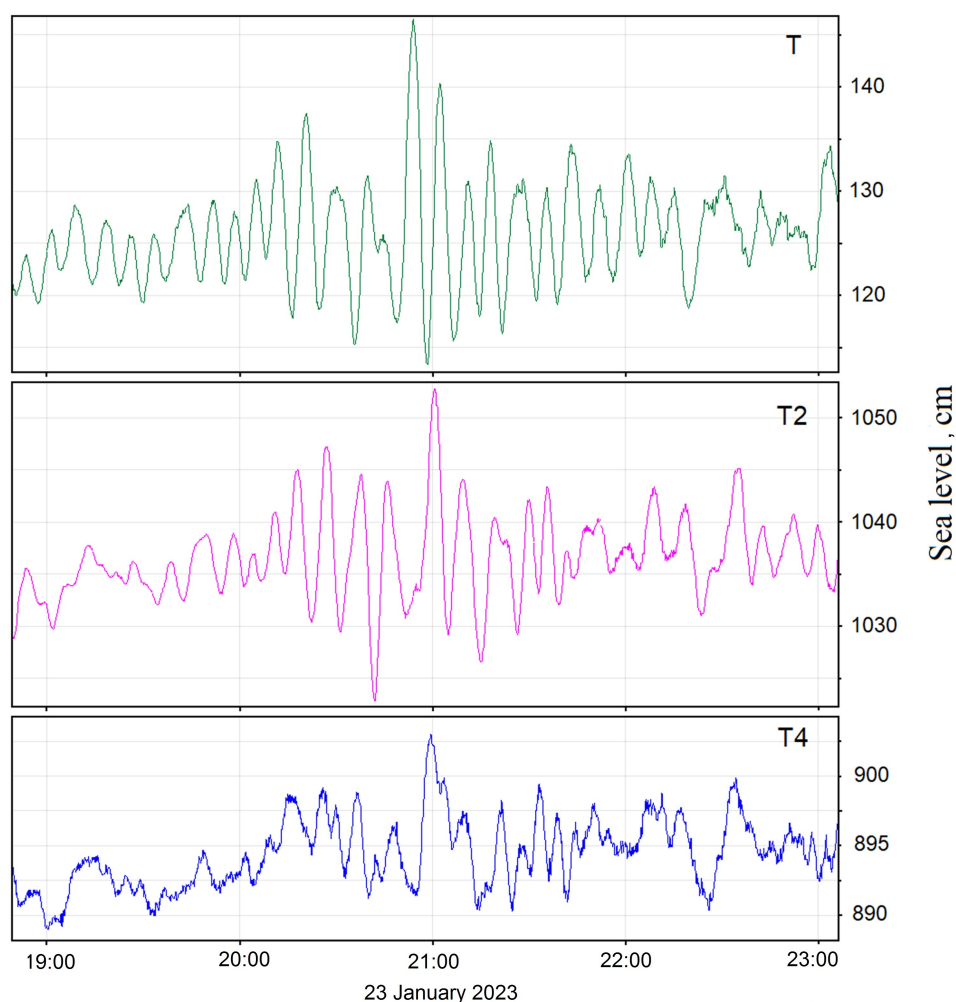


Fig. 5. Time variation of sea level oscillations using the time series with the subtracted precalculated tide in two bays of Kholmsk and in the open sea on January 23, 2023 starting from 19:00

Time variation of sea level oscillations without taking into account the precalculated tide in two bays and in the open sea is represented in Fig. 5 for January 23, 2023. A significant increase in the amplitudes of sea level oscillations with close-by frequencies in the bays from 20:00 to 22:00 is clearly visible. For the open sea, the increase in oscillation amplitudes is 1.5–2 times smaller. At the same time, sea level oscillations at 21:00 in Kholmsk-Severn Bay (T2 meter) and in the open sea (T4 meter) almost coincide in phase, and in Trade Port Bay (T meter) are in an antiphase with them. Note that such synchronous increases in amplitudes are observed quite often and the cases when oscillations with maximum amplitudes in bays coincide in phase (for example, 11 March 2023) also take place.

We are to consider the conditions for generation of such oscillations. They can be different [14], but are usually associated with atmospheric disturbances. Figure 6

shows a fragment of a synoptic map from the weather site rp5.ru for 20 January 2023 at 06:00. It can be seen that at the time of formation of large-amplitude seiches in the bays, a cyclone moved over Sakhalin Island southernmost tip and it was accompanied by prolonged north-northeast winds of $7\text{--}19\text{ m}\cdot\text{s}^{-1}$ speeds and gusts of up to $15\text{ m}\cdot\text{s}^{-1}$. It is obvious that the generation of seiches is caused by the impact of this cyclone. By the time of seiche generation, the background wave did not exceed 5 cm for the waves with periods of up to 10 min. Storm waves arrived at the observation points 12 hours after the occurrence of maximum-amplitude seiches and reached their maximum of 70 cm after 21 hours.

For the segments of time series under consideration (Fig. 5), the spectral densities of sea level oscillations (shown in Fig. 7) are calculated. These more detailed graphs indicate the presence of peaks at 5.62 min period for all meters, as well as at 8.17 and 10.5 min periods for T meter, at 8.65 and 10.92 min periods for T2 meter and 11.37 min period for T4 meter. For periods of ~ 8 minutes, a significant minimum is observed in the spectral density of sea level oscillations, calculated from the T4 meter data.

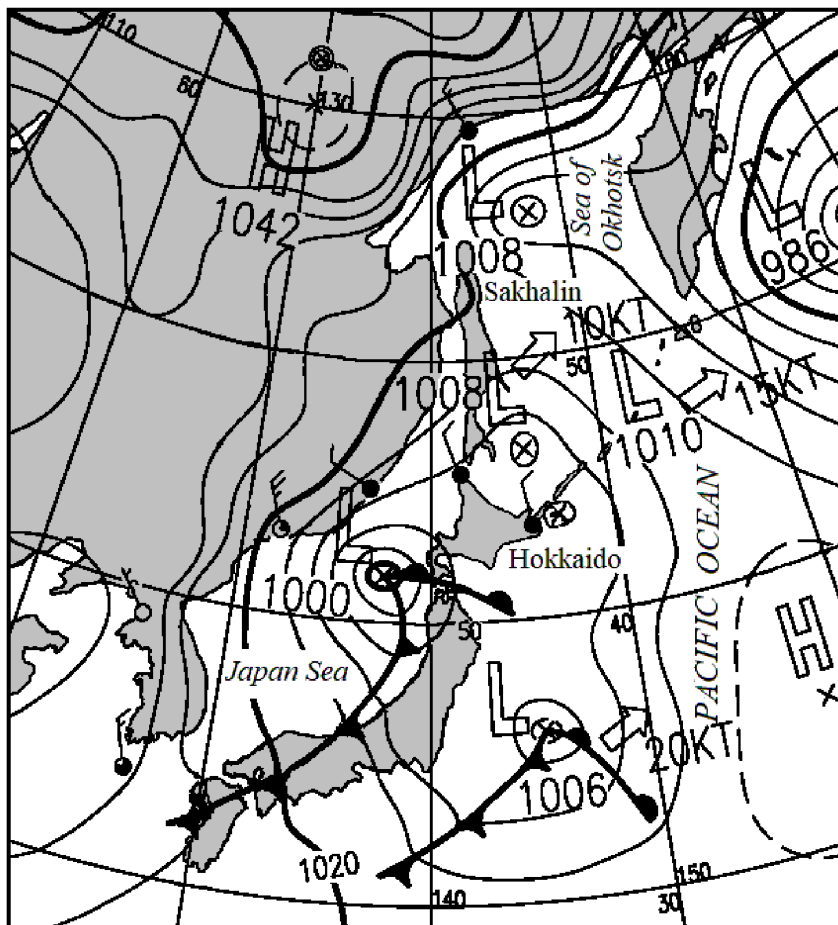


Fig. 6. Fragment of a synoptic map from the open weather site rp5.ru for January 20, 2023 at 6:00

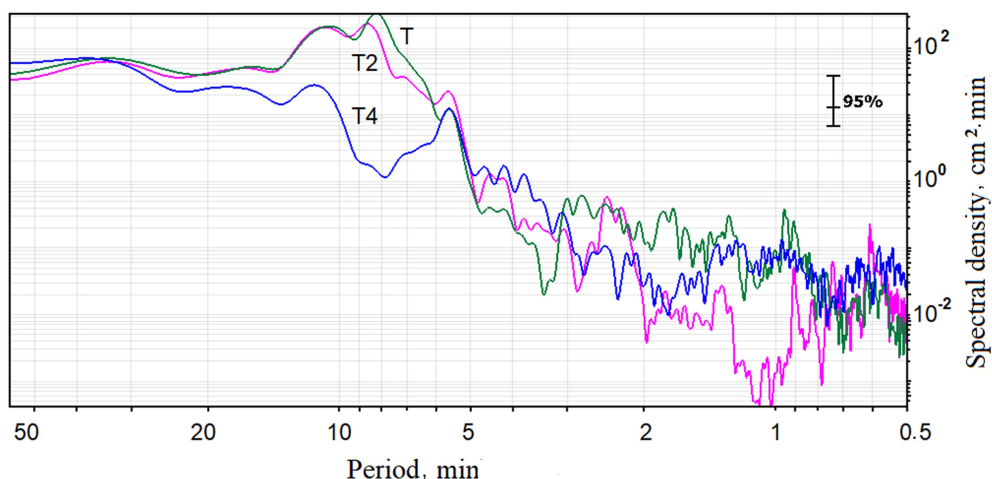


Fig. 7. Spectral densities of sea level oscillations

Since resonant characteristics of the shelf affect the measurements of the instruments located in the bays, they can be removed from the spectra at the inlet sites by dividing the spectra by the spectrum of the instrument installed at the shelf, as proposed in [5]. The square root of this relationship can be considered as an estimate of the transmission function at the inlet, i.e., as the relative amplification of waves penetrating into the bay from the shelf. And since T4 meter was located at some distance from the bay inlets (Fig. 1), we can assume that it was weakly affected by the waves radiated from the bays at resonant frequencies.

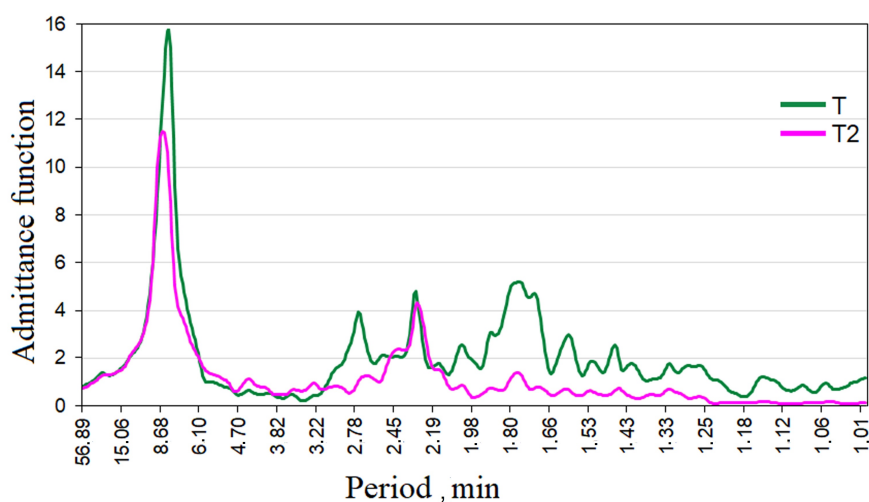


Fig. 8. Admittance (amplification) functions at the inlets of the bays

Admittance functions calculated from the measured sea level oscillations in both bays are represented in Fig. 8. It can be seen that the resonant admittance peaks for both inlets look sharper than in the spectral densities (Fig. 7), and that the corresponding periods are slightly different: for Trade Port Bay the period is 8.0 min, for Kholmsk-Severnny Bay – 8.53 min. According to the authors of [5], such small shifts are not surprising, since the spectrum at the shelf is not constant.

In addition to the main resonant peaks at the inlet to the bays, several secondary peaks are also visible in Fig. 7, 8. If for the Trade Port Bay a peak in the period of the first seiche mode of 2.7 min exists, then a peak in this period for the Kholmsk-Severnny Bay is absent. Also, in both bays at 2.29 min period almost coinciding peaks that do not correspond to eigen oscillations of the bays (Table 3) take place. Apparently, manifestation of this period is due to the occurrence of coupled oscillations in the bays.

Such a system is characterized by a spectrum of normal frequencies ³, which can be reasonably compared with partial frequencies. A partial system is obtained from the original one by removing the connection. For example, one of the pendulums connected by a spring is fixed, or the inlet to one of the bays is closed. Partial frequencies always lie between normal frequencies ³. In Table 3, partial periods are given, since their values were calculated with no regard to the presence of a neighboring bay.

In a system of coupled oscillators, two types of oscillations are possible: in-phase and anti-phase. For example, if the oscillators are pendulums connected by a spring, in-phase oscillations will occur if the spring is not working, and anti-phase oscillations will occur if the spring is working. For bays, this can be represented as follows: in-phase oscillations occur when current lines are directed from the bay towards the open sea, and anti-phase oscillations occur when they pass from one bay to another [4, p. 131]. The period of antiphase oscillations is less than that of in-phase ones [4, p. 130].

Interaction of Kholmsk bays is confirmed by graphs of spectrograms of sea level oscillations, correlations and differences in oscillation phases for these bays (Fig. 9). On the spectrograms of sea level oscillations for each bay (Fig. 9, *a, b*), horizontal stripes are clearly visible at periods of ~ 8 minutes. Moreover, these oscillations were intense throughout the entire observation interval. Due to the connection, the oscillations with the specified period is transmitted from Kholmsk-Severnny Bay to Trade Port Bay and manifests itself there quite intensively.

Similar situation is observed, for example, in the system of Sevastopol bays [7, 8]. The Helmholtz mode of the Sevastopol Bay penetrates into the neighboring Karantinnaya, Kruglaya and other bays, and the Helmholtz mode of Karantinnaya Bay manifests itself with sufficient intensity in Sevastopol Bay.

Constant presence of ~ 8 min period in the spectrum of sea level oscillations in the bays under consideration can be explained by the fact that the Helmholtz mode is usually induced more easily than other modes of eigen oscillations [3]. In addition,

³ Rabinovich, M.I. and Trubetskov, D.I., 1984. *Introduction to the Theory of Oscillations and Waves*. Moscow: Nauka, 432 p. (in Russian).

as mentioned above, the source of long-wave oscillations with the specified period registered by the mareograph in Kholmok are long-wave resonators that accumulate and amplify the energy of trapped waves near Moneron Island and at the shelf near Chekhov [19, p. 44]. The coherence spectrogram (Fig. 9, *d*) at ~ 8 min oscillation periods also demonstrates a band with a coherence of 0.6–0.8 confirming the coupling of oscillations in these bays.

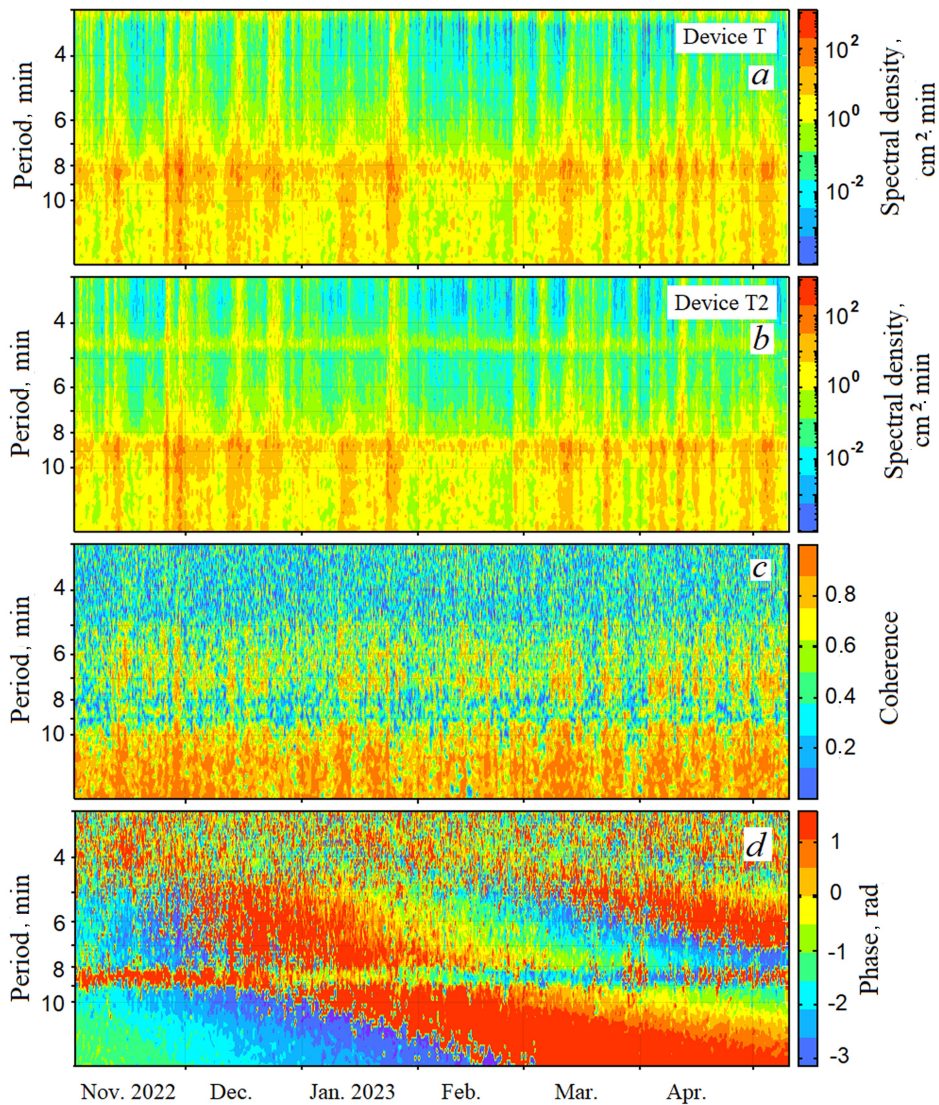


Fig. 9. Spectrograms of sea level oscillations in two bays (*a*, *b*), correlations (*c*) and phase differences (*d*)

Interaction of oscillations in neighboring bays is clearly demonstrated by the spectrogram of their phase difference (Fig. 9, *d*). There is (at 8–9 min periods) a stable horizontal band for the entire observation period, corresponding to the range of periods of eigen oscillations of the bays. Moreover, in January 2023 the oscillations were close to in-phase, and in March – April 2023 – to anti-phase. Besides, a rather slow cyclic phase change is observed in this band. We found this effect and then described it in [1]; it is explained by the synchronization of oscillations in the bay by waves arriving to the inlet ⁴.

On the eigen periods (less than 8 min) of the bays under consideration, no coupling of bays is observed despite the fact that peaks exist in the spectral densities of sea level oscillations at such periods. Apparently, this is due to the fact that the interaction of oscillators at periods of higher eigenmodes is difficult for some reason. This circumstance requires further research.

In [4], special cases of solving the Lagrange equation for an isolated system of two bays during their interaction are considered. Using the equation from this paper, we calculated the beat periods for the case when seiches initially exist only in one of the two bays:

$$T_b = \frac{2\pi}{(n_2 - n_1)/2}, \quad (5)$$

where n_1 and n_2 are frequencies of oscillations in bays. The calculation revealed that for peaks that stand out in the spectral density in two bays with 8.17 and 8.65 min periods, the beat period is 294.5 min (4.91 h). At the same time, in the spectral densities of sea level oscillations calculated from experimental data for three observation points, a peak (Table 1) with a period of 4.82 h (289.2 min) stands out; it differs from the calculated one by 1.8%, which is within the error limits of calculating the spectral density. This wave process is not caused by tidal harmonics or seiches and therefore is really a manifestation of beat caused by the connection between the bays.

Conclusion

Long-term (> 7 months) observations of sea level oscillations were carried out in the adjacent Trade Bay and Kholmsk-Severnny Bay ports, located at 1008 m distance, as well as in the adjacent water area of the Tatar Strait. Discreteness of the performed measurements was one second.

Analysis of sea level oscillations for the range of 1–30 h wave periods, carried out using field data in order to exclude tidal harmonics, indicated the presence of four non-tidal wave processes with 1.6–6.7 h periods. The model calculations carried out revealed that wave processes with such periods can be attributed to shelf seiches, Poincaré waves and the Tatar Strait seiches.

Spectral analysis of 1–10 min period range showed the presence of seiches with 1.83–8.17 min periods in Trade Port Bay and with 1.32–8.65 min periods in Kholmsk-Severnny Bay. In spectral densities of the Tatar Strait sea level oscillations, peaks at 5.62

⁴ Osipov, G.V. and Polovinkin, A.V., 2005. [*Synchronization with External Periodic Impact*]. Nizhniy Novgorod: NNGU, 78 p. (in Russian).

and 11.37 min periods stand out, and at ~ 8 min period, a well-defined minimum is observed.

It is indicated that during the generation of large-amplitude seiche oscillations, a cyclone was moving over the observation area, which was accompanied by prolonged north-northeast winds of $7\text{--}19\text{ m}\cdot\text{s}^{-1}$ speeds and gusts of up to $15\text{ m}\cdot\text{s}^{-1}$.

It is determined that throughout the entire time series of field observations in Kholmsk bays, coupled oscillations over ~ 8 min period took place; they corresponded to the Helmholtz mode period of Kholmsk-Severny Bay. These oscillations were induced in this bay and were transmitted to Trade Port Bay due to interaction. These oscillations at different times had both in-phase and anti-phase spatial structures. During periods of high eigen modes, no interaction between bays was detected.

The spectral analysis of the sea level oscillations under study made it possible to reveal the beats with a period of 4.82 h (289.2 min), resulting from the interaction of modes with close periods equal to 8.17 and 8.65 min.

The stated facts, as well as correspondence of the distance between the inlets of the bays to the proposed earlier interaction condition criterion enable us to assert that the coupled oscillations are present in two adjacent bays – Kholmsk-Severny and Trade Port.

REFERENCES

1. Kovalev, D.P., Kovalev, P.D. and Kirillov, K.V., 2017. The Investigation of Dangerous Marine Phenomena in the Coastal Zone Based on the Field Observations Results. *Geosystems of Transition Zones*, 1(2), pp. 18-34. <http://dx.doi.org/10.30730/2541-8912.2017.1.2.018-034> (in Russian).
2. Parker, B.B., 2007. *Tidal Analysis and Prediction*. NOAA Special Publication NOS CO-OPS 3. Silver Spring, MD: NOAA NOS Center for Operational Oceanographic Products and Services, 378 p. <http://dx.doi.org/10.25607/OBP-191>
3. Rabinovich, A.B., 1993. *Long Gravitational Waves in the Ocean: Capture, Resonance, and Radiation*. Saint Petersburg: Gidrometeoizdat, 325 p. (in Russian).
4. Nakano, M. and Fujimoto, N., 1987. Seiches in Bays Forming a Coupled System. *Journal of the Oceanographical Society of Japan*, 43(2), pp. 124-134. <https://doi.org/10.1007/BF02111888>
5. Liu, P. L.-F., Monserrat, M., Marcos, M. and Rabinovich, A.B., 2003. Coupling between Two Inlets: Observation and Modeling. *Journal of Geophysical Research: Oceans*, 108(C3), 3069. <https://doi.org/10.1029/2002JC001478>
6. Aranguiz, R., Catalán, P.A., Cecioni, C., Bellotti, G., Henriquez, P. and González, J., 2019. Tsunami Resonance and Spatial Pattern of Natural Oscillation Modes with Multiple Resonators. *Journal of Geophysical Research: Oceans*, 124(11), pp. 7797-7816. <https://doi.org/10.1029/2019JC015206>
7. Manilyuk, Yu.V., Lazorenko, D.I. and Fomin, V.V., 2020. Investigation of Seiche Oscillations in the Adjacent Bays by the Example of the Sevastopol and the Quarantine Bays. *Physical Oceanography*, 27(3), pp. 242-256. <https://doi.org/10.22449/1573-160X-2020-3-242-256>
8. Manilyuk, Yu.V., Fomin, V.V., Yurovsky, Yu.Yu. and Bagaev, A.V., 2024. Sea Level Oscillations Spectra of a Shallow Coastal Bay: Cost-Effective Measurements and Numerical Modelling in Kruglaya Bay. *Regional Studies in Marine Science*, 69, 103326. <https://doi.org/10.1016/j.rsma.2023.103326>

9. Plekhanov, Ph.A. and Kovalev, D.P., 2016. The Complex Program of Processing and Analysis of Time-Series Data of Sea Level on the Basis of Author's Algorithms. *Geoinformatika*, (1), pp. 44-53 (in Russian).
10. Munk, W., Snodgrass, F. and Gilbert, F., 1964. Long Waves on the Continental Shelf: An Experiment to Separate Trapped and Leaky Modes. *Journal of Fluid Mechanics*, 20(4), pp. 529-554. <https://doi.org/10.1017/S0022112064001392>
11. Wilson, B.W., 1972. Seiches. In: V. T. Chow, ed., 1972. *Advances in Hydrosience*. New York and London: Academic Press. Vol. 8, pp. 1-94. <https://doi.org/10.1016/B978-0-12-021808-0.50006-1>
12. Korgen, B.J., 1995. Seiches: Transient Standing-Wave Oscillations in Water Bodies Can Create Hazards to Navigation and Unexpected Changes in Water Conditions. *American Scientist*, 83(4), pp. 330-341.
13. De Jong, M., 2004. *Origin and Prediction of Seiches in Rotterdam Harbor Basins*. The Netherlands: Partners Ipskamp Beheer B.V., 119 p.
14. Rabinovich, A.B., 2009. Seiches and Harbor Oscillations. In: Y. C. Kim, ed., 2009. *Handbook of Coastal and Ocean Engineering*. Singapore: World Scientific Publishing Company, pp. 193-236. https://doi.org/10.1142/9789812819307_0009
15. Manilyuk, Yu.V. and Cherkosov, L.V., 2017. Investigation of Seiche Oscillations in a Free Entrance Bay. *Physical Oceanography*, (4), pp. 16-25. <https://doi.org/10.22449/1573-160X-2017-4-16-25>
16. Murty, T.S., 1977. *Seismic Sea Waves: Tsunamis*. Ottawa: Department of Fisheries and the Environment Fisheries and Marine Service, 337 p.
17. Manilyuk, Yu.V. and Sannikov, V.F., 2019. Research of Seiche Oscillations in the Bay of Variable Depth. *Ecological Safety of Coastal and Shelf Zones of Sea*, (2), pp. 4-12. <https://doi.org/10.22449/2413-5577-2019-2-4-12> (in Russian).
18. Levin, B.V. and Tikhonov, I.N., 2009. *Nevelsk Earthquake and Tsunami, Sakhalin Island, the 2 August, 2007*. Moscow: Yanus-K, 204 p. (in Russian).
19. Vturina, A.S., Shustin, V.A., Khramushin, V.N., Shevchenko, G.V. and Ivelskaya, T.N., 2004. Research of the Hydrodynamic Conditions of the Kholmsk Seaport Water Area. *Vestnik of Far East Branch of the Russian Academy of Sciences*, (1), pp. 40-51 (in Russian).
20. Manilyuk, Y.V. and Cherkosov, L.V., 1997. The Influence of the Gulf's Geometry on Seiche Oscillations in an Enclosed Basin. *Physical Oceanography*, 8(4), pp. 217-227. <https://doi.org/10.1007/BF02523662>
21. Shevchenko, G.V., Kovalev, P.D. and Kovalev, D.P., 2012. Resonance of Waves at a Train Ferry. *World of Transport and Transportation*, (1), pp. 58-65 (in Russian).
22. Nakano, M., 1932. The Secondary Undulations in Bays Forming a Coupled System. *Proceedings of the Physico-Mathematical Society of Japan. 3rd Series*, 14, pp. 372-380. https://doi.org/10.11429/ppmsj1919.14.0_372

About the authors:

Dmitry P. Kovalev, Chief Research Associate, Head of Laboratory of Wave Dynamics and Coastal Currents, Institute of Marine Geology and Geophysics, Far Eastern Branch of RAS (1b Nauki Str., Yuzhno-Sakhalinsk, 693022, Russian Federation), DSc (Phys.-Math.), **ORCID ID: 0000-0002-5184-2350**, **ResearchID: A-9300-2016**, **Scopus Author ID: 26032627700**, d.kovalev@imgg.ru

Yuri V. Manilyuk, Research Associate, Wave Theory Department, Marine Hydrophysical Institute of RAS (2 Kapitanskaya Str., Sevastopol, 299011, Russian Federation), CSc (Phys.-Math.), **ORCID ID: 0000-0002-5752-7562**, **ResearchID: P-6662-2017**, **Scopus Author ID: 6602563261**, uvmsev@yandex.ru

Petr D. Kovalev, Leading Research Associate, Laboratory of Wave Dynamics and Coastal Currents, Institute of Marine Geology and Geophysics, Far Eastern Branch of RAS (1b Nauki Str., Yuzhno-Sakhalinsk, 693022, Russian Federation), DSc (Tech.), **ORCID ID: 0000-0002-7509-4107**, **ResearcherID: V-8662-2018**, **Scopus Author ID: 16429135400**, p.kovalev@imgg.ru

Contribution of the co-authors:

Dmitry P. Kovalev – general scientific supervision of research; formulation of goals; writing the paper text; analysis of results and their interpretation; description and discussion of the research results; drawing conclusions; critical text analysis

Yuri V. Manilyuk – participation in the formulation of problem; review of the literature on the research topic; analysis of the results and their interpretation and systematization; writing the paper text; discussing the paper materials and editing the paper text, preparing it for publication; formulation of conclusions

Petr D. Kovalev – participation in the formulation of the problem, collection of available materials on the research topic; analysis of results and their interpretation; systematization, processing and visualization of field observation data; writing the paper text, discussing materials of the paper and text editing; formulating the conclusions, critical analysis of the text

The authors have read and approved the final manuscript.

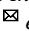
The authors declare that they have no conflict of interest.

Original article

Resuspension of Bottom Sediments in a Shallow Lagoon by Currents and Waves Based on the Numerical Modeling Data (Using the Example of Sivash Bay, the Sea of Azov)

V. V. Fomin, E. V. Ivancha , A. A. Polozok

Marine Hydrophysical Institute of RAS, Sevastopol, Russian Federation

 ev_ivancha@rambler.ru

Abstract

Purpose. The work is purposed at studying the intensity of resuspension of silty bottom sediments in Eastern Sivash Bay (the Sea of Azov) during an extreme storm, as well as at assessing the contribution of currents and wind waves to the resuspension processes.

Methods and Results. The current fields are calculated using a three-dimensional σ -coordinate water circulation model of the *POM* type supplemented with a block of silty sediments resuspension. The *SWAN* spectral model is applied to calculate wind waves. In both models a rectangular computational grid with the horizontal resolution 300 m is involved. The *ERA-Interim* atmospheric reanalysis data corresponding to the extreme storm situation in November 10–13, 2007 are used as a forcing. The performed calculations constituted a base for analyzing the structure of the fields of waves, currents, bottom shear stresses and suspended matter concentration in Eastern Sivash for different phases of the storm. A technique for assessing the resuspension model sensitivity to the variations in the input parameter values is proposed.

Conclusions. The applied resuspension model is most sensitive to the variations in the parameter values that condition intensity of the silt particles vertical flow from the basin bottom. During the period of the storm maximum development, conditions for forming resuspension zones arise on 80 % of the total area of Eastern Sivash Bay. If, while modeling, the contribution of the waves is not taken into account, the total area of resuspension is reduced by four times. This fact testifies to a decisive contribution of the bottom wave stresses in formation of the resuspension zones in bottom sediments in the bay.

Keywords: resuspension, bottom sediments, silt fraction, currents, wind waves, numerical modeling, Sivash

Acknowledgments: The study was carried out within the framework of theme of the FSBSI FRC MHI FNNN-2021-0005. The model calculations were performed at the MHI computing cluster.

For citation: Fomin, V.V., Ivancha, E.V. and Polozok, A.A., 2024. Resuspension of Bottom Sediments in a Shallow Lagoon by Currents and Waves Based on the Numerical Modeling Data (Using the Example of Sivash Bay, the Sea of Azov). *Physical Oceanography*, 31(3), pp. 427-445.

© 2024, V. V. Fomin, E. V. Ivancha, A. A. Polozok

© 2024, Physical Oceanography

Introduction

The need to study water dynamics of Sivash Bay of the Sea of Azov is associated with active anthropogenic transformations of this water area of the Crimean coastal zone. The bay is a recoverable deposit of mineral salts, it is characterized by high biodiversity and included in the list of wetlands of international importance. A special economic zone “Sivash” with a developed chemical industry and agriculture is located on the coast of the bay [1].

The present-day Sivash is a vast shallow bay of the Sea of Azov (a lagoon-type sea bay) with an indented coastline. Sivash is usually divided into two large regions –



Western and Eastern Sivash (Fig. 1, *a*). Western Sivash is currently an almost completely isolated basin, its water level is regulated by a dam, its depth usually does not exceed 0.3–0.4 m. Eastern Sivash is a deeper (up to 3 m) section of the bay, occupying over 60% of the total area of Sivash.

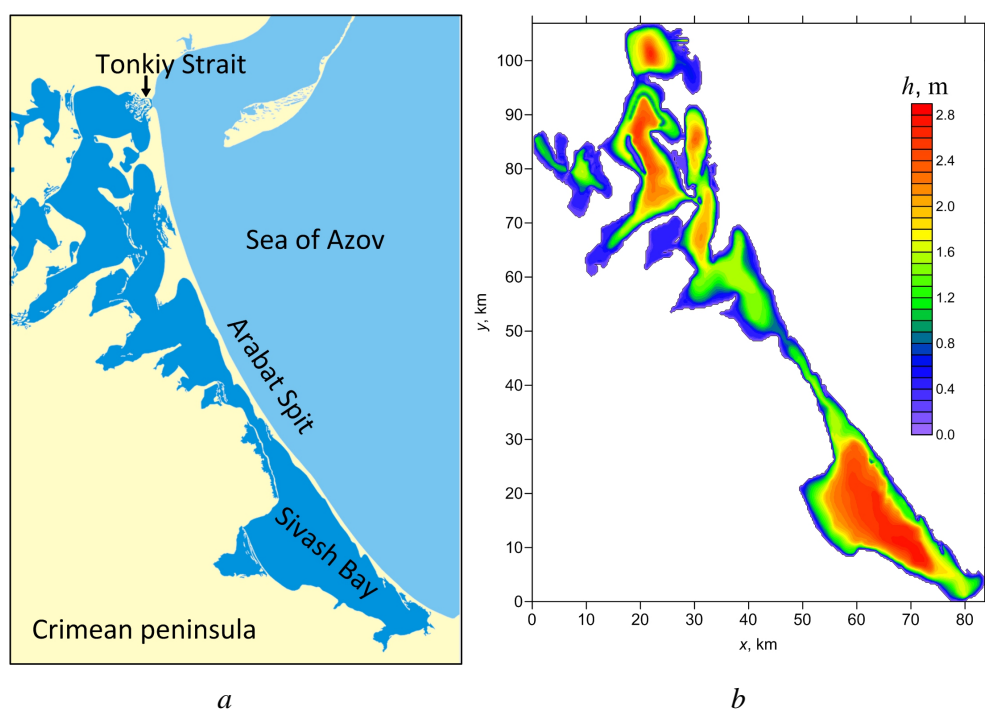


Fig. 1. Location of East Sivash Bay (*a*), model bottom relief of East Sivash Bay (*b*)

Several publications are devoted to the study of hydrodynamic processes in Eastern Sivash. The work [2] presents calculations of surface currents and level oscillations in the bay under winds of various directions. The characteristics of a freshwater plume in the area where the Salgir River flows into Sivash Bay are studied in [3]. In [4], current fields in Eastern Sivash are modeled for different wind conditions. It is demonstrated that the structure of water circulation in the bay is determined by the general direction of the wind. The field of depth-average currents consists of several eddy structures. These structures are expressed especially well in the southern part of the water area. When winds are directed along the water area of the bay, the circulation is most intense. In these cases, in the narrowness connecting the northern and southern parts of Eastern Sivash, a jet current with a speed of more than 1 m/s occurs. In the deepest parts of the water area, a bottom countercurrent is formed near the bottom.

In [5], modeling of the wind wave characteristics in Eastern Sivash was carried out. It is revealed that due to the shallowness of the water area and relatively small effective fetches, the main factor affecting the intensity of waves is wind speed. The waves reach a steady state 3 h after the start of the wind effect. After the wind stops, the waves completely cease after 2 h. Estimates of the maximum values of wave parameters for different wind speed gradations showed that even during

the periods of strong storm, the heights and periods of waves in the waters of Eastern Sivash do not exceed 1 m and 3 s, respectively. In these works, the problems of the effect of currents and waves on the dynamics of bottom sediments in the waters of Eastern Sivash remained beyond the scope of the studies.

The problems of mathematical modeling of suspended matter evolution in shallow waters are considered in [6, 7]. The work [6] simulates the processes of bottom sediment resuspension and sedimentation at the Black Sea northwestern shelf during the passage of an atmospheric cyclone with no regard to wind waves. Bottom sediments are assumed to consist of a single silt fraction. The areas of the most intense rise of suspended matter and vertical profiles of suspended bottom sediment concentration in individual areas are analyzed. A similar study for the eastern part of the Gulf of Finland, but with regard to wind waves, was carried out in [7]. Here, the calculations were carried out for two fractions of bottom sediments: fine-grained sand and silt. The contribution of currents and waves to the sediment resuspension intensity is studied. The importance of taking into account the contribution of wind waves to resuspension processes is shown.

This work is purposed at mathematical modeling of the process of bottom sediment resuspension in Eastern Sivash. Mathematical modeling is an important part of environmental monitoring of the water area; it allows one to calculate various parameters of the bay state, which are not always possible to obtain experimentally. The paper presents the results of numerical experiments on modeling the resuspension of silty sediments during an extreme storm. A description of the mathematical models we applied is given below. The main attention is paid to the analysis of the contribution of currents and waves to the resuspension intensity.

The major problem of mathematical modeling of bottom sediment resuspension is the lack of the required amount of initial data. As a rule, the granulometric composition of bottom sediments is known fragmentarily; there is not enough field observation data to validate models; the selection of critical values of bottom shear stresses determining resuspension processes is a separate task. Currently available field studies in Eastern Sivash [8, 9] do not provide a complete understanding of suspended matter dynamics in the bay, since they are episodic and carried out directly offshore in relatively calm weather. For this cause, the bottom sediment resuspension model sensitivity to changes in input parameters was analyzed.

Materials and methods

Wave model. To calculate wind wave fields in Eastern Sivash Bay, we apply the Simulating Waves Nearshore (SWAN) model [10], based on the numerical solution of the wave energy balance equation in spectral form

$$\frac{\partial}{\partial t} N + \frac{\partial}{\partial x} (c_x N) + \frac{\partial}{\partial y} (c_y N) + \frac{\partial}{\partial \omega} (c_\omega N) + \frac{\partial}{\partial \theta} (c_\theta N) = S / \omega, \quad (1)$$

where $N = E/\omega$ is wave action density; E is wave energy spectrum; x, y, t are spatial coordinates and time; ω, θ are frequency and angular coordinates; $c_x, c_y, c_\omega, c_\theta$ are rates of wave action density transfer along spatial and frequency-angular coordinates.

The source function on the right side of equation (1) has the following form:

$$S = S_{\text{in}} + S_{\text{nl}} + S_{\text{wc}} + S_{\text{bf}} + S_{\text{dib}}, \quad (2)$$

where S_{in} is a source of wind-induced waves; S_{nl} are nonlinear interactions of spectral harmonics; S_{wc} is energy dissipation due to wave crests breaking; S_{bf} is energy dissipation due to bottom friction; S_{dib} is wave breaking at critical depths. Details of parameterization of individual source function terms (2) are given in the manual ¹.

The model bottom relief of Eastern Sivash Bay is represented in Fig. 1, *b*. To calculate wave characteristics, we use a rectangular grid with a horizontal resolution of $\Delta x = \Delta y = 300$ m (284×334 nodes). The discreteness of the model along the angular coordinate is 10° . An uneven grid with 31 nodes is applied along the frequency coordinate, varying within 0.04–1.0 Hz range. We use a non-stationary version of the SWAN model. Integration over time is carried out using an implicit difference scheme with 30 min step.

The outputs of the SWAN model are fields of significant wave height h_s , mean wave direction θ_w , peak wave period T_p and amplitudes of near-bottom orbital motion velocity U_w . These parameters are applied to calculate bottom shear stresses in the model of currents and the bottom sediment resuspension model.

Model of currents. In order to calculate current fields, we used a barotropic version of the three-dimensional hydrostatic water circulation model proposed in [11]. The model is based on three-dimensional σ -coordinate equations of hydrodynamics in the hydrostatic approximation (hereinafter, summation is carried out over repeating indices α and β from 1 to 2):

$$\frac{\partial}{\partial t}(Du_\alpha) + \Lambda u_\alpha + \varepsilon_{\alpha\beta} f Du_\beta + gD \frac{\partial \eta}{\partial x_\alpha} = \frac{\partial}{\partial x_\beta}(D\tau_{\alpha\beta}) + \frac{\partial}{\partial \sigma} \left(\frac{K_M}{D} \frac{\partial u_\alpha}{\partial \sigma} \right), \quad (3)$$

$$\frac{\partial \eta}{\partial t} + \frac{\partial}{\partial x_\alpha}(Du_\alpha) + \frac{\partial w_*}{\partial \sigma} = 0, \quad (4)$$

$$\Lambda \phi = \frac{\partial}{\partial x_\beta}(Du_\beta \phi) + \frac{\partial}{\partial \sigma}(w_* \phi), \quad \tau_{\alpha\alpha} = 2A_M \frac{\partial u_\alpha}{\partial x_\alpha}, \quad \tau_{\alpha\beta} = \tau_{\beta\alpha} = A_M \left(\frac{\partial u_\beta}{\partial x_\alpha} + \frac{\partial u_\alpha}{\partial x_\beta} \right), \quad (5)$$

where $(x_1, x_2) = (x, y)$; σ is dimensionless vertical coordinate varying from -1 to 0 ; $(u_1, u_2) = (u, v)$ are current velocity components along the axes x_1, x_2 ; w_* is current velocity component directed along the normal to the surfaces $\sigma = \text{const}$;

¹ USER MANUAL SWAN Cycle III Version 41.45. Delft University of Technology. [online] Available at: https://swanmodel.sourceforge.io/online_doc/swanuse/swanuse.html [Accessed: 03 June 2024].

$D = h + \eta$; h is basin depth; η is free surface coordinate; f is the Coriolis parameter; $\varepsilon_{\alpha\beta} = 0$ at $\alpha = \beta$ and $\varepsilon_{12} = -1$, $\varepsilon_{21} = 1$; $\tau_{\alpha\beta}$ are components of the turbulent stress tensor; A_M, K_M are coefficients of turbulent viscosity; g is gravitational acceleration.

At the solid lateral boundaries of the computational domain, no-slip conditions are set for velocities and conditions for turbulent fluxes to be equal to zero. To simplify the problem, water exchange through the Tonkiy Strait is not taken into account.

On the free surface of the basin ($\sigma = 0$), the boundary conditions have the following form:

$$w_* = 0, \quad \rho \frac{K_M}{D} \frac{\partial u_\alpha}{\partial \sigma} = \rho_0 c_0 W \cdot W_\alpha, \quad (6)$$

where ρ_0 is air density; $c_0 = (0.49 + 0.065W) \cdot 10^{-3}$ is surface friction coefficient; $W = \sqrt{W_1^2 + W_2^2}$ is modulus of near-water wind speed; W_1, W_2 are zonal and meridional wind speed components.

At the bottom ($\sigma = -1$), the boundary conditions are set by the following expressions:

$$w_* = 0, \quad \rho \frac{K_M}{D} \frac{\partial u_\alpha}{\partial \sigma} = \tau_c \frac{u_\alpha}{U_c}, \quad (7)$$

where $U_c = \sqrt{u_1^2 + u_2^2}$ is modulus of horizontal velocity of currents; τ_c is near-bottom shear stress determined by the formula

$$\tau_c = \rho c_b U_c^2, \quad (8)$$

where $c_b = 0.16 / \ln^2(\delta z / z_b)$ is bottom friction coefficient; δz is vertical distance from the bottom to the point where the friction coefficient is determined; $z_b = d_{50} / 30$ is bottom surface roughness parameter; d_{50} is average diameter of bottom soil particles corresponding to silt deposits.

To determine the coefficient of vertical turbulent exchange K_M , the Mellor–Yamada model is applied [12]. The horizontal turbulent exchange coefficient A_M is calculated using the Smagorinsky formula [13].

The boundary value problem (3)–(8) is solved numerically on the basis of explicit difference schemes for horizontal coordinates and implicit difference schemes for vertical coordinates. To approximate Λ advection operator, monotonic difference schemes are used. A detailed description of numerical algorithm is given in [11]. For horizontal coordinates, the same computational grid as in the SWAN model is applied. Along σ -coordinate, 11 uniform computational levels are specified.

Model of bottom sediment resuspension. The model of bottom sediment resuspension is incorporated into the water circulation model and is based on numerical solution of transport-diffusion equation of the following form:

$$\frac{\partial}{\partial t}(DC) + \Lambda C - \frac{\partial(w_s C)}{\partial \sigma} = \frac{\partial}{\partial x_\beta} \left(A_c D \frac{\partial C}{\partial x_\beta} \right) + \frac{\partial}{\partial \sigma} \left(\frac{K_c}{D} \frac{\partial C}{\partial \sigma} \right), \quad (9)$$

where C is volumetric concentration of suspended particles, m^3/m^3 ; w_s is rate of gravitational settling of particles, depending on their density ρ_c and average diameter d_{50} ; A_c, K_c are coefficients of horizontal and vertical diffusion determined in the water circulation model.

At the solid lateral boundaries of the computational domain, conditions for the turbulent fluxes of substance C are set to be equal to zero.

On the free surface, the condition of the suspended flow absence is specified [6, 14]

$$-w_s C - \frac{K_c}{D} \frac{\partial C}{\partial \sigma} = 0. \quad (10)$$

The resuspended matter flow from the bottom is determined by the difference between F_e erosion and F_d sedimentation flows [6, 14]:

$$-w_s C - \frac{K_c}{D} \frac{\partial C}{\partial \sigma} = F_e - F_d. \quad (11)$$

F_e and F_d flows are functions of bed shear stress τ_b caused by the combined contribution of currents and waves. In the context of the problem under consideration, the value τ_b plays a key role in modeling the process of bottom sediment resuspension.

The erosion flow is non-zero in the case when bottom shear stresses exceed the critical value τ_{ce} :

$$F_e = \begin{cases} M_0 \left(\frac{\tau_b}{\tau_{ce}} - 1 \right), & \tau_b \geq \tau_{ce}, \\ 0, & \tau_b < \tau_{ce}, \end{cases} \quad (12)$$

where M_0 is empirical coefficient characterizing the intensity of sediment resuspension and varying within the range of 10^{-6} – $10^{-2} \text{ kg}/(\text{m}^2 \cdot \text{s})$ [15].

The sedimentation flow is determined by the concentration of sediments at the bottom C_a and is different from zero when bottom shear stresses are less than a certain critical value τ_{cd} [6, 14]:

$$F_d = \begin{cases} w_s C_a \left(1 - \frac{\tau_b}{\tau_{cd}} \right), & \tau_b < \tau_{cd}, \\ 0, & \tau_b \geq \tau_{cd}, \end{cases} \quad (13)$$

where value C_a is assessed by the following formulas [16, p. 673]:

$$C_a = 0.015 \left(\frac{d_{50}}{a} \right) \frac{(\tau_b / \tau_s - 1)^{1.5}}{d_*^{0.3}}, \quad d_* = d_{50} \left[\frac{g \Delta}{\nu^2} \right]^{1/3}, \quad \Delta = \frac{\rho_c}{\rho} - 1, \quad (14)$$

here $a = 0.05D$ is reference level; d_* is dimensionless diameter of particles; $\nu = 10^{-6} \text{ m}^2/\text{s}$ is molecular viscosity coefficient; τ_s is bottom shear stress determined by the Shields criterion.

To evaluate τ_b , the following ratios are used ² [7, p. 37]:

$$\tau_b = \sqrt{(\tau_m + \tau_w |\cos \phi|)^2 + (\tau_w |\sin \phi|)^2}, \quad \tau_m = \tau_c \left[1 + 1.2 \left(\frac{\tau_w}{\tau_c + \tau_w} \right)^{3.2} \right], \quad (15)$$

where ϕ is an angle between the direction of current and waves.

Bottom shear stress caused by wave action is defined as

$$\tau_w = \frac{1}{2} \rho f_w U_w^2, \quad (16)$$

where f_w is wave drag coefficient; U_w is velocity of bottom orbital movements from the SWAN model. A semi-empirical dependence is used to assess f_w [5, p. 100; 17]

$$f_w = \min \{ \exp[5.5(k_b/A)^{0.2} - 6.3], 0.3 \}, \quad (17)$$

where $k_b = 2.5d_{50}$; $A = U_w T_p / 2\pi$.

Research results and discussion

Dynamics of the waters of Eastern Sivash Bay is largely determined by the local features of atmospheric processes on a synoptic scale. According to ERA-Interim global atmospheric reanalysis data ³ over the period of 1979–2020, statistical

² Soulsby, R.L., 1997. *Dynamics of Marine Sands: A Manual for Practical Applications*. London: Tomas Telford Services, 249 p.

³ ECMWF. *Archive Catalogue*. [online] Available at: apps.ecmwf.int [Accessed: 03 June 2024].

characteristics of surface wind speed W for the water area under study are as follows[5]: long-term average value is 7.3 m/s; standard deviation is 3.6 m/s. The greatest occurrence frequency (23%) has the northeastern wind and the least occurrence frequency (5%) has the wind of southeastern direction. The frequency occurrence of winds of other directions does not exceed 10–12%.

From the point of view of studying bottom sediment resuspension in Eastern Sivash Bay, the greatest interest is in cases where the water area of the bay is affected by intense non-stationary atmospheric disturbances such as cyclones. Therefore, as an atmospheric forcing from the ERA-Interim reanalysis data, we selected a synoptic situation (from 00:00 November 10, 2007 to 00:00 November 13, 2007) when an anomalously deep cyclone formed in the western part of the Black Sea. The cyclone moved eastward towards the Sea of Azov and during its movement crossed the waters of Eastern Sivash Bay creating significant atmospheric disturbances over it.

Resuspension was modeled with the following values of input parameters: $\rho_c = 2000 \text{ kg/m}^3$; $d_{50} = 0.01 \text{ mm}$; $\tau_{ce} = 0.13 \text{ N/m}^2$; $\tau_{cd} = 0.1 \text{ N/m}^2$; $M_0 = 10^{-5} \text{ kg/m}^2/\text{s}$.

These constants are taken from [6, p. 9; 7, p. 40]. Sedimentation rate of particles w_s is determined by predetermined values ρ_c and d_{50} . Calculations were carried out for the silt fraction of bottom particles, since the bottom of Eastern Sivash Bay is a silt layer of up to 5 m thickness or more ⁴.

The numerical modeling was carried out in two stages. At the first stage, the wave parameters included in the formulas for calculating bottom stresses (12)–(17) were calculated using the SWAN model. Wave fields were stored with 1 h discreteness. At the second stage, current fields and concentrations of suspended particles were calculated using a water circulation model.

Figure 2, *a* represents the temporal variation of surface wind speed W over the water area of Eastern Sivash Bay for the synoptic situation under consideration (solid curve – average W value over the water area, dashed curve – maximum W value over the water area). The dependence of average wind direction θ_A over the bay area on time is shown in Fig. 2, *b*. Time moment $t = 0$ corresponds to the initial date of synoptic situation in this and other graphs.

The most significant W variations occur in the time interval from 0 to 36 h. Until $t = 18 \text{ h}$, wind speed monotonically increases from 4 m/s to its maximum value. At $t \leq 12 \text{ h}$, the prevailing wind is from the south and southeast. After 12 o'clock, wind changes its direction to southwestern. At $t > 18 \text{ h}$, the storm fades and the wind speed decreases.

⁴ Stashchuk, M.F., Suprychev, V.A. and Khitraya, M.S., 1964. [*Mineralogy, Geochemistry and Conditions for the Formation of Bottom Sediments of the Sivash*]. Kiev: Naukova Dumka, 174 p. (in Russian).

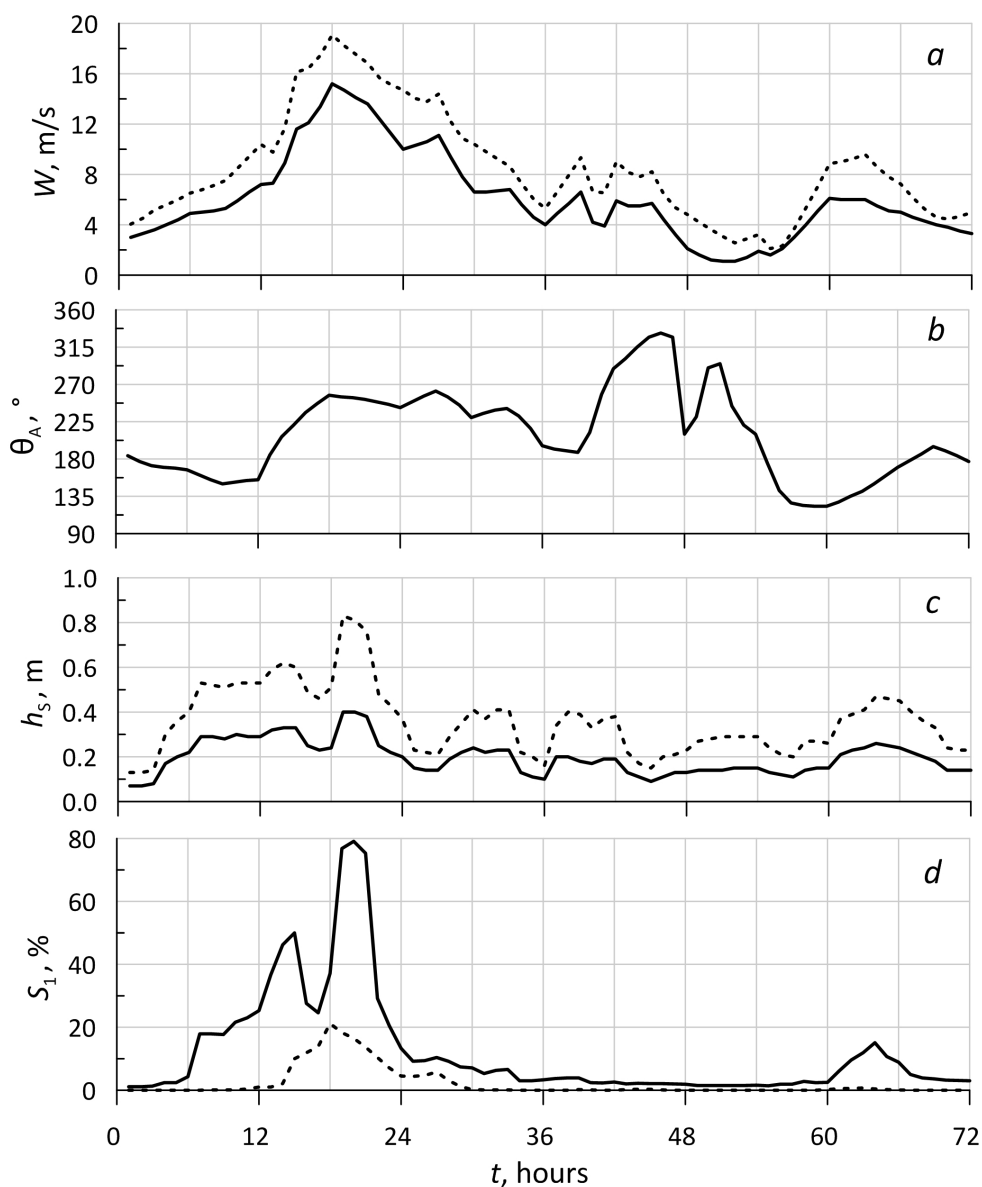


Fig. 2. Wind speed W (a), wind direction θ_A (b), significant wave heights h_s (c) (solid curve shows average values over the water area, dashed line – maximum values over the water area), and integral indicator of bottom sediments resuspension S_1 (solid line – with regard to wave stress, dashed line – with no regard to it) (d)

When an atmospheric cyclone passes through the bay, a non-stationary wave field, caused by temporal variability of wind speed and direction, is generated. The dependences of significant wave heights h_s on time for the considered synoptic situation are given in Fig. 2, c (solid curve – average h_s value over the water area,

dashed curve – maximum h_s value over the water area). It can be seen that wave height is sensitive to changes in both wind speed and direction. When the wind direction changes, the wave height decreases. A phase shift of 1 h is observed between the time of wind speed maximum occurrence and wave height. The maximum wind speed is reached at $t = 18$ h and the maximum wave height is reached at $t = 19$ h.

To quantify the intensity of bottom sediment resuspension in Eastern Sivash Bay, an integral resuspension indicator was applied

$$S_n = 100\% \cdot A_n / A_0, \quad (18)$$

where A_n is bay surface area where the condition for the occurrence of bottom sediment erosion $\tau_b \geq n\tau_{ce}$ is fulfilled, $n \geq 1$ is integer; A_0 is area of the entire bay.

We performed two calculations of integral resuspension index. In the first calculation of indicator (18), wave stress τ_w was taken into account when determining bottom stresses τ_b . S_1 dependence on t (solid curve in Fig. 2, *d*) has two peaks; they correspond to the maximum values: $S_1 = 50\%$ at $t = 15$ h; $S_1 = 80\%$ at $t = 20$ h. Thus, during the period of the maximum storm development, conditions for resuspension of bottom sediments are created on 80% of the bay water area. S_1 curve peaks are shifted relative to the maximum wave heights by 1 h and they are quite sharp, which indicates a rapid course of erosion and deposition processes in bottom sediments. The strongest resuspension occurs during the period of maximum development of wind waves and lasts 3–4 hours. At $n > 1$ (zones of intense resuspension), the following values of the maximum resuspension index were obtained: $S_2 = 35\%$; $S_3 = 10\%$; $S_4 = 5\%$.

The second calculation of the resuspension index (dashed curve in Fig. 2, *d*) was carried out with no regard to the wave stress ($\tau_b = \tau_c$). In this case, only one maximum $S_1 = 21\%$ at $t = 18$ h arises, which corresponds to the occurrence time of the maximum wind speed. From a comparison of both options for calculating S_1 indicator, the following conclusion can be drawn: bottom wave stress makes a decisive contribution to the formation of areas of bottom sediment resuspension, which is explained by the bay shallowness.

Now, let us move on to considering the spatial structure of model fields. As a typical example, Fig. 3 indicates spatial distributions of wind speed W , significant wave height h_s , velocity of bottom wave currents U_w and velocity of wind currents in the bottom layer U_c .

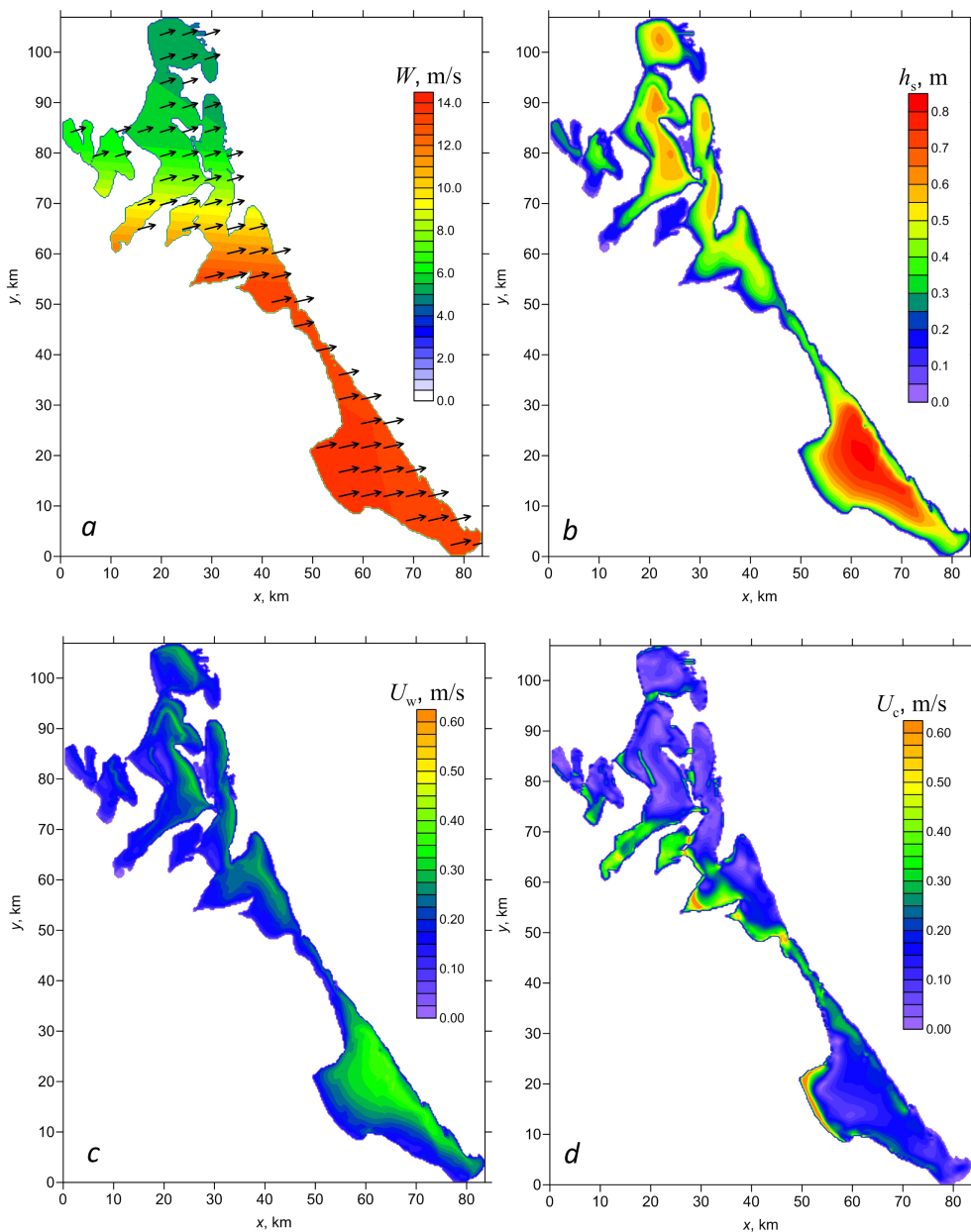


Fig. 3. Wind speed and direction (*a*), significant wave heights (*b*), velocity of the bottom wave (*c*) and bottom wind (*d*) currents in Eastern Sivash Bay at $t = 19$ h

These fields correspond to the time moment $t = 19$ h, when the wind waves in the bay reached their maximum intensity. The wind has a predominant western-southwestern direction and its speed is maximum in the southern part of the bay (Fig. 3, *a*). Here, we can also see the area of maximum waves with wave heights exceeding 0.8 m (Fig. 3, *b*). Wave intensification occurs in the hollows. The areas of maximum waves are shifted to the windward coast. The velocity of bottom wave

currents reaches 0.4 m/s. In this case, the configurations of the velocity field of near-bottom wave currents (Fig. 3, *c*) and the wave height field are well-corresponded to each other. The areas of maximum bottom wind currents with up to 0.8 m/s velocities are localized in shallow water near the leeward shores of the basin and in the narrowness connecting the northern and southern parts of the bay (Fig. 3, *d*).

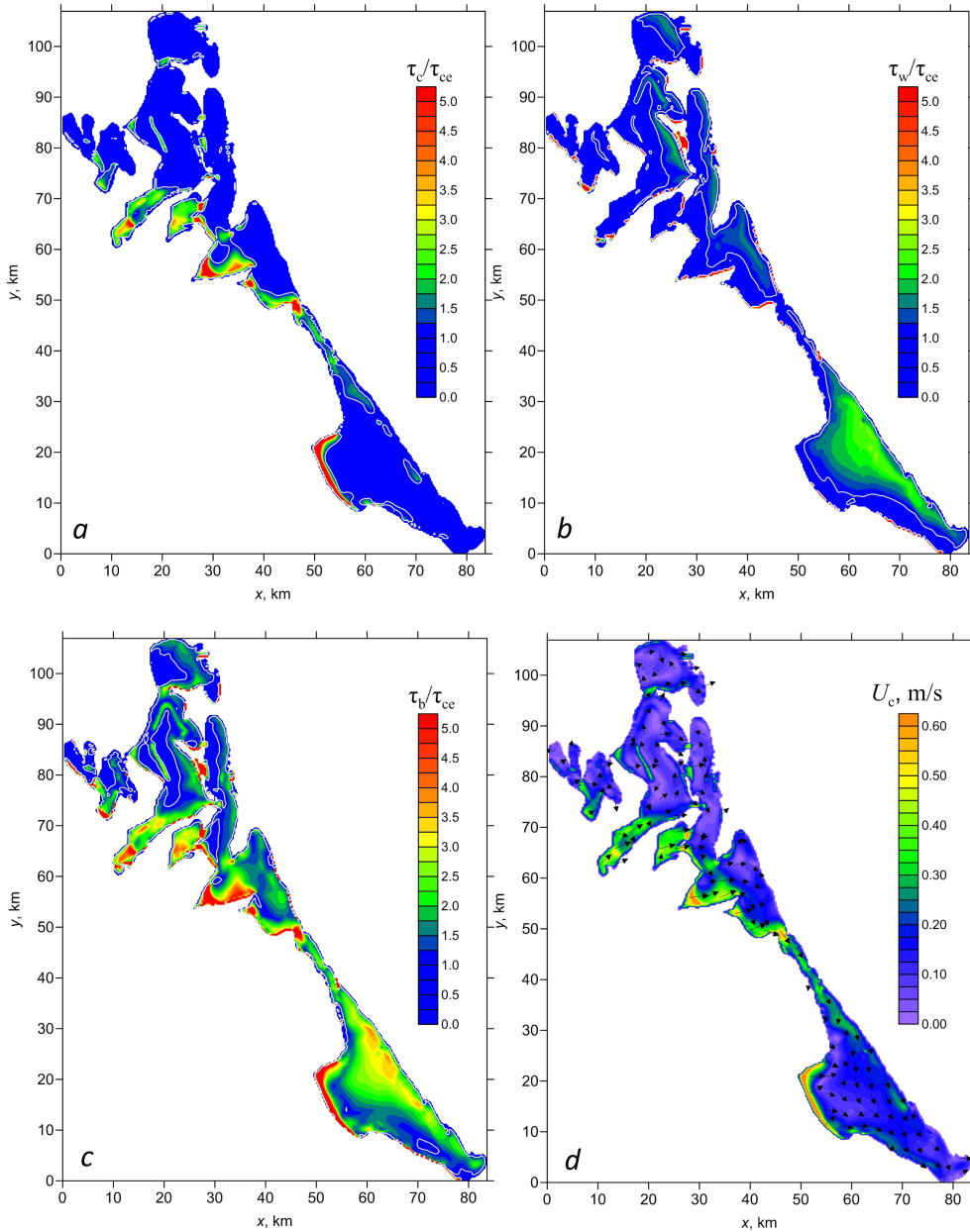


Fig. 4. Spatial distribution of bottom shear stresses in Eastern Sivash Bay and wind current velocities in the bottom layer at $t = 19$ h

Figure 4 demonstrates the fields of bottom shear stresses τ_c , τ_w and τ_b for $t = 19$ h normalized to the critical value τ_{ce} . In general, the configuration of these fields is similar to the one of the bottom current fields (Fig. 4, *d*). The component of shear stresses caused by wind currents increases near the leeward shores and the wave component of shear stresses, on the contrary, increases near the windward shores of the basin.

In some cases, the values τ_c are noticeably higher than τ_w . However, strong bottom stresses caused by currents are concentrated in small areas, while waves generate bottom stresses $\tau_w \geq \tau_{ce}$ over a much larger area of the bay. Thus, when calculating the total bottom stress τ_b , it is necessary to take into account both the bottom wave-generated stress and the stress generated by currents.

Analysis of C vertical structure of the concentration field showed that the concentration profiles of silty suspended matter depend weakly on depth during a storm. The resuspension of silty sediments occurs very quickly. The maximum differences between C values at the surface and at the bottom are no more than 0.1 mg/l. This consistency of profiles is due to bay shallowness and a vertical mixing effect.

In Fig. 5, the fields of depth-average suspended matter concentration for characteristic moments of time are shown:

$$C_m = \int_{-1}^0 C d\sigma.$$

Local turbidity sources, which increase in size and intensify over time, appear near the coast at the initial stage ($t = 8$ h). By $t = 20$ h time point, the bottom sediment resuspension reaches its maximum intensity. Further, sedimentation processes begin – suspended matter concentration in the water column decreases quite quickly and the turbidity areas begin to shrink ($t = 24$ h).

During a storm, in areas where the bottom wind current velocities are maximum, the calculated values C_m at individual points reach 250 mg/l. In numerical experiments, this result is determined primarily by the bay shallowness, the silty nature of bottom and low values of particle sedimentation rate. The question of whether such large concentration values can exist in Eastern Sivash remains open, since no data on suspended matter concentrations under storm conditions is currently available. It can be noted that calculations for the completely silty bottom of Neva Bay provide the same order of magnitude values for the suspended matter concentration [7].

In the bottom sediment resuspension model (9)–(17), as well as in other similar models, the values of input parameters have a large degree of uncertainty. Therefore, it is of interest to evaluate the sensitivity of the resuspension model under consideration to changes in the values of these parameters.

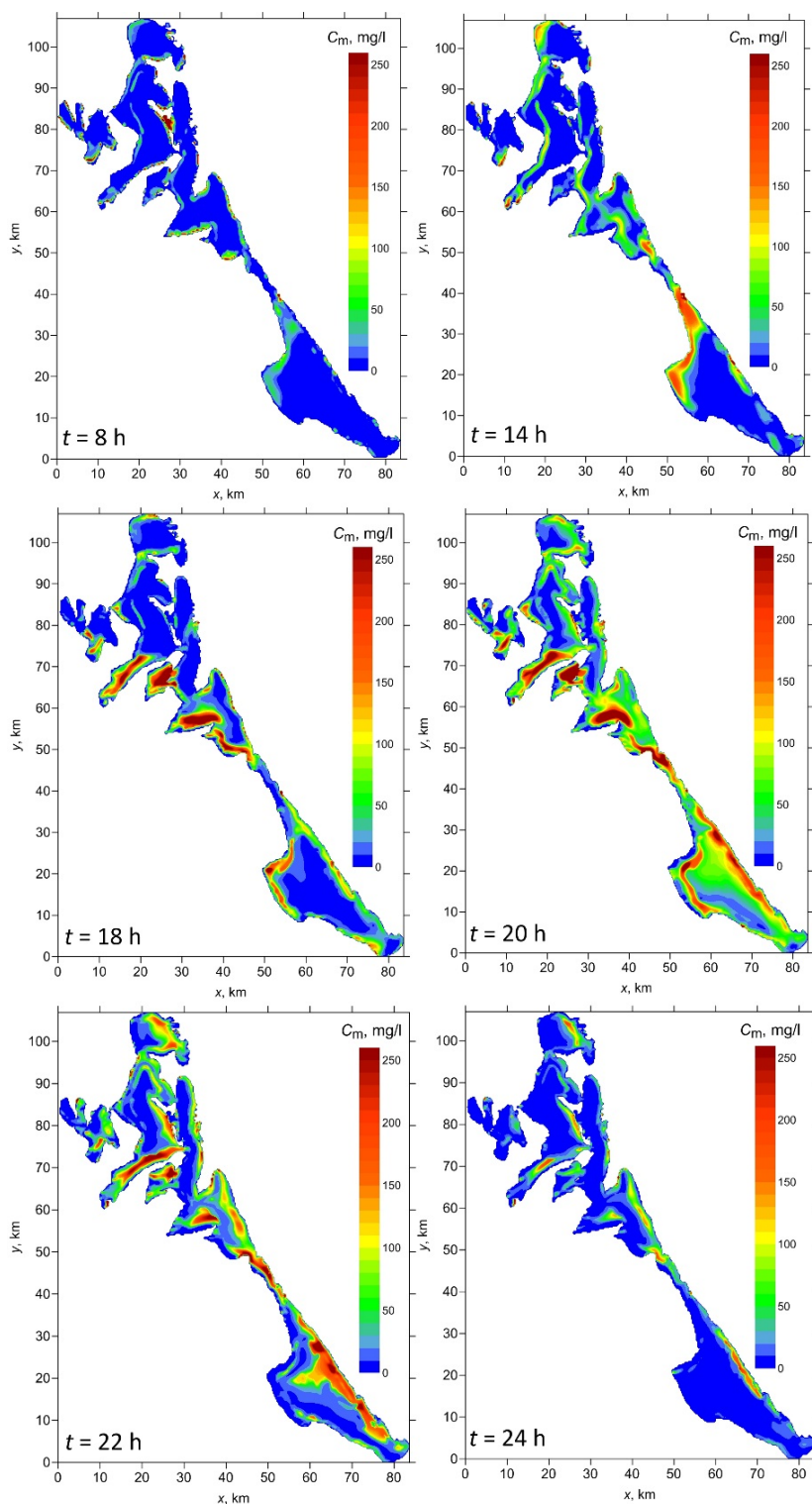


Fig. 5. Field of the depth-average concentration of suspended matter C_m in Eastern Sivash Bay for different time points

For quantitative assessment of resuspension model sensitivity to variations in input parameters, 12 numerical experiments with different combinations of parameters were performed. The list of parameter values is given in Table 1. Model solution deviations from the base case ($k = 1$) were analyzed.

Table 1

Parameters of bottom sediment resuspension model					
k	ρ_c , kg/m ³	d_{50} , mm	τ_{ce} , H/m ²	τ_{cd} , H/m ²	M_0 , kg/m ² /s
1	2000	0.010	0.130	0.10	10^{-5}
2	2000	0.010	0.156	0.10	10^{-5}
3	2000	0.010	0.104	0.10	10^{-5}
4	2000	0.015	0.130	0.10	10^{-5}
5	2000	0.020	0.130	0.10	10^{-5}
6	2000	0.010	0.130	0.10	10^{-4}
7	2000	0.010	0.130	0.10	10^{-6}
8	2000	0.010	0.130	0.10	10^{-3}
9	2000	0.010	0.130	0.12	10^{-5}
10	2000	0.010	0.130	0.08	10^{-5}
11	2100	0.010	0.130	0.10	10^{-5}
12	1900	0.010	0.130	0.10	10^{-5}

Note: k is the experiment number.

For each k we calculated integral indicator

$$B_{kp} = 100\% \cdot Q_{kp} / Q_0, \quad (19)$$

where index p is threshold value of average suspended matter concentration C_m , characterizing resuspension intensity; Q_{kp} is total surface area of the bay where the condition $C_m \geq p$ is satisfied; Q_0 is total surface area of the entire bay.

Indicator (19) provides the total relative size of bottom sediment resuspension sources of different intensity at a specific time point. Five threshold p values (5, 10, 25, 50 and 100 mg/l) were considered. It was revealed that the greatest increase in B_{kp} index occurs during the period of maximum storm development ($t = 19\text{--}22$ h); therefore, B_{kp} maxima sensitivity to changes in input parameters was analyzed.

Values of $\max B_{kp}$, as well as the difference $\gamma_{kp} = \max B_{kp} - \max B_{1p}$ (Table 2), which is a deviation of B_{kp} maximum from B_{1p} maximum of the base experiment, are given below for each numerical experiment.

Table 2

**Values of $\max B_{kp}$ (%) and γ_{kp} (%) for different options
of specifying the resuspension model parameters**

k	p , mg/l									
	5		10		25		50		100	
	$\max B_{kp}$	γ_{kp}	$\max B_{kp}$	γ_{kp}	$\max B_{kp}$	γ_{kp}	$\max B_{kp}$	γ_{kp}	$\max B_{kp}$	γ_{kp}
1	94	0	91	0	82	0	70	0	49	0
2	91	-3	86	-5	73	-9	58	-12	36	-13
3	97	3	95	4	88	6	80	10	65	16
4	90	-4	86	-5	76	-6	62	-8	37	-12
5	87	-7	82	-9	70	-12	53	-17	27	-22
6	96	2	94	3	90	8	87	17	83	34
7	76	-18	57	-34	24	-58	9	-61	2	-47
8	92	-2	90	-1	85	3	82	12	78	29
9	94	0	91	0	81	1	68	2	47	2
10	95	0	92	1	83	0	72	0	51	0
11	94	0	91	1	81	0	70	0	49	0
12	94	0	92	1	82	0	70	0	49	0

In all experiments, p increases with B_{kp} index decrease. The behavior of γ_{kp} parameter demonstrates the opposite trend: with increasing p , the deviations of maxima from the base experiment in absolute value increase, i.e. the impact of variations in the model parameters is more pronounced for areas with large suspended matter concentrations.

In experiments 2 and 3, the influence of critical shear stress τ_{ce} on variations in resuspension areas was assessed. The τ_{ce} value changed by $\pm 20\%$ relative to the base value. With an increase in τ_{ce} by 20%, depending on p values, the resuspension areas decrease by 3–13%. When τ_{ce} decreases by 20%, the resuspension areas are reduced by 3–16%.

In experiments 4 and 5, the average particle diameter d_{50} varied. The increase of d_{50} by 50 and 100% results in a decrease in resuspension areas by 4–12 and 7–22%, respectively.

In experiments 6, 7 and 8, the value of M_0 parameter varied. When M_0 decreases by an order of magnitude, the resuspension areas are reduced by 18–61%. An increase in this parameter by two orders of magnitude increases the resuspension areas by 2–34%.

In experiments 9 and 10, τ_{cd} stress effect on variations in resuspension areas was assessed. A weak dependence of resuspension areas on the values of this parameter was revealed (variations do not exceed 2%).

As shown by experiments 11 and 12, variations in the density of bottom sediment particles ρ_c by $\pm 5\%$ relative to the base value also do not have a noticeable effect on variations in resuspension areas (variations do not exceed 2%).

Thus, the most significant parameters in the bottom sediment resuspension model we applied, are the parameters τ_{ce} and M_0 , which determine the intensity of vertical flow of particles from the bottom.

It seems possible to use an integral indicator of B_{kp} type to clarify the values of the resuspension model input parameters based on remote sensing data for certain areas of the Sea of Azov. To do this, it is necessary to obtain the resuspension areas from satellite images using a regional algorithm for estimating the suspended matter concentration [18] and calculate the B_{kp} index. Next, based on a series of model calculations, we are to select the value of this indicator, which is close to the indicator value obtained from remote sensing data. The problem of estimating the parameters of a model for bottom sediment resuspension in shallow waters is of independent interest and the authors considered it as a continuation of the research presented in this paper.

Conclusion

Based on a combination of numerical models of wind waves and currents, the process of bottom silty sediment resuspension in the eastern part of Sivash Bay during the extreme storm on November 10–13, 2007 was studied. Analysis of numerical modeling results revealed the following.

The strongest bottom sediment resuspension in the bay occurs during the period of wind wave maximum intensification and lasts 3–4 h. During the storm, vertical profiles of silty suspended matter C concentration weakly depend on depth. The maximum differences between C values at the surface and at the bottom are no more than 0.1 mg/l.

Bottom wave stresses τ_w make a decisive contribution to the formation of bottom sediment resuspension areas in the bay. When they are taken into account, the conditions for forming resuspension areas ($\tau_w \geq \tau_{ce}$) are created on 80% of the bay area. If wave stresses are not taken into account during modeling, the total resuspension area is reduced by ~ 4 times.

Currents can also generate bottom stresses $\tau_c \geq \tau_{ce}$, but this occurs in small parts of the water area near the shore, while waves generate bottom stresses $\tau_w \geq \tau_{ce}$ throughout most of the bay. Thus, when calculating the total bottom stress τ_b , it is necessary to take into account both wave stresses and stresses caused directly by currents.

Based on multivariate calculations, it was found that the silt resuspension model we applied is most sensitive to variations in the values of τ_{ce} and M_0 parameters, which determine intensity of the vertical flow of particles from the basin bottom.

The results of the work can be useful in planning and interpreting field experiments in Sivash Bay and other shallow areas of the Sea of Azov.

REFERENCES

1. Sovga, E.E., Eremina, E.S. and D'yakov, N.N., 2018. System of the Ecological Monitoring in the Sivash Bay in the Modern Conditions. *Ecological Safety of Coastal and Shelf Zones of Sea*, (2), pp. 22-38. <https://doi.org/10.22449/2413-5577-2018-2-22-38> (in Russian).

2. Sovga, E.E., Eryemina, E.S. and Khmara, T.V., 2018. Water Balance in the Sivash Bay as a Result of Variability of the Natural-Climatic and Anthropogenic Factors. *Physical Oceanography*, 25(1), pp. 67-76. <https://doi.org/10.22449/1573-160X-2018-1-67-76>
3. Fomin, V.V. and Polozok, A.A., 2022. Features of River Plume Formation in a Shallow Lagoon (the Case of the Sivash Bay, the Sea of Azov). *Ecological Safety of the Coastal and Shelf Zones of the Sea*, (3), pp. 28-42.
4. Polozok, A.A., Fomin, V.V. and Ivancha, E.V., 2023. Numerical Modeling of Wind Currents in the Sivash Gulf (Sea of Azov). In: T. Chaplina, ed., 2023. *Processes in GeoMedia*. Singapore: Springer, vol. VII, pp. 9-20. https://doi.org/10.1007/978-981-99-6575-5_2
5. Fomina, I.N., Fomin, V.V. and Polozok, A.A., 2022. Wind Waves in Sivash Bay According to the Results of Numerical Modeling. In: SSC RAS, 2022. *Ecology. Economy. Informatics. System Analysis and Mathematical Modeling of Ecological and Economic Systems*. Rostov-on-Don: SSC RAS, 1(7), pp. 97-102. <https://doi.org/10.23885/2500-395X-2022-1-7-97-102> (in Russian).
6. Alekseev, D.V., Ivanov, V.A., Ivancha, E.V., Fomin, V.V. and Cherkesov, L.V., 2007. Investigation of the Fields of Concentration of the Suspension on the Northwest Shelf of the Black Sea in the Case of Roiling of the Bottom Sediments by a Moving Cyclone. *Physical Oceanography*, 17(1), pp. 1-16. <https://doi.org/10.1007/s11110-007-0001-0>
7. Martyanov, S.D. and Ryabchenko, V.A., 2013. Simulation of the Resuspension and Transport of Bottom Sediments in the Neva Bay Using a 3D Circulation Model. *Fundamental and Applied Hydrophysics*, 6(4), pp. 32-43 (in Russian).
8. Sovga, E.E., Eremina, E.S. and Latushkin, A.A., 2020. Research Expeditions Performed by Marine Hydrophysical Institute in the Sivash Bay Waters in Spring and Autumn, 2018. *Physical Oceanography*, 27(2), pp. 161-170. <https://doi.org/10.22449/1573-160X-2020-2-161-170>
9. Lomakin, P.D., 2021. Features of the Oceanological Values Fields in the Sivash Bay (The Sea of Azov). *Physical Oceanography*, 28(6), pp. 647-659. <https://doi.org/10.22449/1573-160X-2021-6-647-659>
10. Booij, N., Ris, R.C. and Holthuijsen, L.H., 1999. A Third-Generation Wave Model for Coastal Regions: 1. Model Description and Validation. *Journal of Geophysical Research: Oceans*, 104(C4), pp. 7649-7666. <https://doi.org/10.1029/98JC02622>
11. Ivanov, V.A. and Fomin, V.V., 2010. *Mathematical Modeling of Dynamical Processes in the Sea-Land Area*. Kyiv: Akadempriodyka, 286 p.
12. Blumberg, A.F. and Mellor, G.L., 1987. A Description of a Three-Dimensional Coastal Ocean Circulation Model. *Coastal and Estuarine Science*, 4, pp. 1-16. <https://doi.org/10.1029/CO004>
13. Smagorinsky, J., 1963. General Circulation Experiments with the Primitive Equations: I. The Basic Experiment. *Monthly Weather Review*, 91(3), pp. 99-164. [https://doi.org/10.1175/1520-0493\(1963\)091<0099:GCEWTP>2.3.CO;2](https://doi.org/10.1175/1520-0493(1963)091<0099:GCEWTP>2.3.CO;2)
14. Burchard, H., Bolding, K. and Villarreal, M., 2004. Three-Dimensional Modelling of Estuarine Turbidity Maxima in a Tidal Estuary. *Ocean Dynamics*, 54(2), pp. 250-265. <https://doi.org/10.1007/s10236-003-0073-4>
15. Yang, Z. and Hamrick, J.M., 2003. Variational Inverse Parameter Estimation in a Cohesive Sediment Transport Model: An Adjoint Approach. *Journal of Geophysical Research: Oceans*, 108(C2), 3055. <https://doi.org/10.1029/2002jc001423>
16. Van Rijn, L.C., 2007. Unified View of Sediment Transport by Currents and Waves. II: Suspended Transport. *Journal of Hydraulic Engineering*, 133(6), pp. 668-689. [https://doi.org/10.1061/\(ASCE\)0733-9429\(2007\)133:6\(668\)](https://doi.org/10.1061/(ASCE)0733-9429(2007)133:6(668))
17. Kuhrt, C., Fennel, W. and Seifert, T., 2004. Model Studies of Transport of Sedimentary Material in the Western Baltic. *Journal of Marine Systems*, 52(1-4), pp. 167-190. <https://doi.org/10.1016/j.jmarsys.2004.03.005>
18. Kremenchtskiy, D.A., Kubryakov, A.A., Zav'yalov, P.O., Konovalov, B.V., Stanichniy, S.V. and Aleskerova, A.A., 2014. Determination of the Suspended Matter Concentration in the Black Sea Using the Satellite MODIS Data. In: MHI, 2014. *Ecological Safety of Coastal and Shelf Zones and Comprehensive Use of Shelf Resources*. Sevastopol: ECOSI-Gidrofizika. Iss. 29, pp. 5-9 (in Russian).

About the authors:

Vladimir V. Fomin, Head of Department of Computational Technologies and Mathematical Modeling, Marine Hydrophysical Institute of RAS (2 Kapitanskaya Str., Sevastopol, 299011, Russian Federation), DSc (Phys.-Math.), **ORCID ID: 0000-0002-9070-4460**, **ResearcherID: H-8185-2015**, v.fomin@mhi-ras.ru

Elena V. Ivancha, Junior Research Associate, Marine Hydrophysical Institute of RAS (2 Kapitanskaya Str., Sevastopol, 299011, Russian Federation), **ORCID ID: 0000-0001-8328-4915**, **ResearcherID: AAG-9265-2020**, ev_ivancha@rambler.ru

Anton A. Polozok, Senior Software Engineer, Marine Hydrophysical Institute of RAS (2 Kapitanskaya Str., Sevastopol, 299011, Russian Federation), **ORCID ID: 0000-0002-0825-8669**, **ResearcherID: ADJ-1790-2022**, polozok.umi@gmail.com

Contribution of the co-authors:

Vladimir V. Fomin – formulating research goals, numerical implementation of mathematical problem, carrying out calculations, analyzing results, preparing paper text

Elena V. Ivancha – searching for materials on research objectives in domestic and foreign sources, formulating research goals, participating in the discussion of paper materials, text editing

Anton A. Polozok – formulating research objectives, participation in the discussion of paper materials, scientific analysis and visualization of numerical calculation results

The authors have read and approved the final manuscript.

The authors declare that they have no conflict of interest.